Experimental Study of Heat Flux Partitioning in Pressurized Subcooled Flow Boiling

by

Andrew Jonathan Richenderfer

B.S., Physics, Case Western Reserve University (2012)
S.M., Nuclear Science and Engineering, Massachusetts Institute of Technology (2015)

Submitted to the Department of Nuclear Science and Engineering
in partial fulfillment of the requirements for the degree of

Doctor of Philosophy in Nuclear Science and Engineering

at the

MASSACHUSETTS INSTITUTE OF TECHNOLOGY

February 2018

Author .....
Department of Nuclear Science and Engineering
December 21, 2017

Certified by .....
Matteo Bucci, Ph.D.
Assistant Professor of Nuclear Science and Engineering
Thesis Supervisor

Certified by .....
Jacopo Buongiorno, Ph.D.
TEPCO Professor of Nuclear Science and Engineering
Thesis Reader

Certified by .....
Emilio Baglietto, Ph.D.
Norman C. Rasmussen Associate Professor of Nuclear Science and Engineering
Thesis Reader

Accepted by .....
Ju Li, Ph.D.
Battelle Energy Alliance Professor of Nuclear Science and Engineering
Professor of Materials Science and Engineering
Chairman, Department Committee on Graduate Theses

Experimental Study of Heat Flux Partitioning in Pressurized Subcooled Flow Boiling

by

Andrew Jonathan Richenderfer

Submitted to the Department of Nuclear Science and Engineering
on December 21, 2017, in partial fulfillment of the
requirements for the degree of
Doctor of Philosophy in Nuclear Science and Engineering

Abstract

Understanding of subcooled flow boiling and the critical heat flux (CHF) is of the utmost importance for both safety and profitability of pressurized water nuclear reactors since they are major factors in the determination of the reactor power rating.

Motivated by the emergence of a new wall boiling model by Gilman [3] and previous experimental insights from Phillips [12], a first-of-a-kind experimental investigation of pressurized steady-state subcooled flow boiling was conducted using state-of-the-art diagnostics to gain a unique insight of the relevant mechanisms, including the partitioning of the wall heat flux. Conditions up to 10 bar pressure, 2000 $\frac{kg}{m^2 s}$ mass flux and 20 K subcooling were explored.

High-speed infrared thermometry tools were developed and used to measure the local time-dependent 2-D temperature and heat flux distributions on the boiling surface. These distributions were analyzed to determine fundamental boiling heat transfer parameters such as the nucleation site density, growth and wait times, nucleation frequency, departure diameter as well as the partitioning of the wall heat flux.

While established mechanistic models can capture the trends of growth time and wait time with relatively good accuracy, this work reveals current models do not accurately predict the activation and interaction of nucleation sites on the boiling surface. This is a major roadblock, since boiling curves and CHF values obtained in nominally identical environments can be significantly different depending upon the nucleation site density which in turn is determined by the surface properties.

The role of evaporation in the partitioning of the heat flux increases monotonically as the average heat flux increases, up to a maximum value of 70%, and is the dominant mechanism at high heat fluxes. At low and intermediate heat fluxes single-phase heat transfer is the dominant mechanism. Traditional heat partitioning models fail to capture these physics, but newer models with a comprehensive and physically consistent framework show promise in predicting the wall heat transfer. The data and understanding produced by this work will be essential for the development and validation of these modeling tools.

Thesis Supervisor: Matteo Bucci, Ph.D.
Title: Assistant Professor of Nuclear Science and Engineering

Acknowledgments

To start, I would like to acknowledge Dr. Tom McKrell. Tom had a tremendous effect on me both personally and professionally. His contributions to my work and development as a researcher cannot be overstated. He was a terrific advisor and a wonderful person. We miss him dearly, and his memory will never be forgotten.

I would like to thank my advisor, Professor Bucci. You've helped me every step of the way. Whether it be teaching me how to properly thread a hole, or a leisurely lunchtime chat about the Patriots to assuage a challenging day in the lab. I'm deeply thankful for everything you've taught me.

Thank you to Professor Buongiorno for your support over the years and serving as a reader for this thesis. I still remember the day we met during the new student visit and you offered me the opportunity to work in Green Lab. I truly wouldn't be here without your support.

Thanks to Professor Baglietto for his advisement on this project and serving as a reader for this thesis. Your input has been invaluable throughout my project.

I would also like to thank Dr. Bren Phillips. Your guidance during my first few years at MIT was extremely helpful. Thank you for showing me the ropes.

A special thank you to my office-mates, Carolyn, Guanyu and Melanie. We spent many afternoons brainstorming and learning together. I couldn't have asked for a better set of friends to share this experience with.

Thanks to Artyom and Jee for your help running the CASL loop and post-processing the data. Your help and input throughout the process has been invaluable. I wish you the both the best of luck in your future studies and research. I'd also like to thank the rest of my lab-mates Chi, MD, Mathias and Megan for their help in lab, and Ravi and Etienne for their help with the computational and post-processing work.

I'd like to thank my teachers and advisors from Case Western Reserve University and The Harley School for all the guidance they've given me over the years.

None of this would have been possible without the support from the Consortium

for Advanced Simulation of Light Water Reactors (CASL) and the Nuclear Engineering University Program (NEUP).

To my family, my mother Betty, my father Tom, my sister Laura, my brother-in-law Mike, and the newest member, my nephew Jack; your continual love and support helped me throughout my studies. Thank you for all the phone calls and emails checking in on me. Thank you for all the help when I was in a bind. I couldn't have done it without you.

To Amy, thank you for being everything I needed. Your encouragement and support to pursue my dreams has lead me to where I am today. Your love and kindness got me through an incredibly challenging time in my life. I couldn't imagine a better partner to share my future with.

Contents

1 Introduction **23**

1.1 Motivation 23

1.2 Goals 24

1.3 Objectives 26

1.3.1 Original Scientific Contributions 26

1.3.2 Workflow 27

1.4 Background 30

1.4.1 Bubble Nucleation 30

1.4.2 Subcooled Flow Boiling 33

1.4.3 Heat Flux Partitioning Modeling 34

1.4.4 Infrared Thermometry 37

1.5 Previous Research 39

2 Experimental Apparatus and Methods **45**

2.1 Pressurized Flow Loop 45

2.2 Test Section 52

2.3 Heater Cartridge 59

2.4 ITO Heater 62

2.5 Infrared and High-Speed Video Cameras 63

2.6 Burnout Prevention System 65

2.7 Polarity Switching System 66

2.8 Experimental Methods 70

3 Post-Processing, Results and Analysis **75**

3.1 Test Matrix 75

3.2 Post-Processing of IR Data and Boiling Curve Results 77

3.2.1 IR Calibration with the Radiation-Conduction Model 77

3.2.2 Boiling Curves 86

3.3 Nucleation Site Density 89

3.3.1 Nucleation Site Density Post-Processing 90

3.3.2 Nucleation Site Density Comparison Model 91

3.3.3 Nucleation Site Density Results 92

3.4 Bubble Period, Growth Time and Wait Time 95

3.4.1 Bubble Period, Growth Time and Wait Time Post-Processing 95

3.4.2 Bubble Period, Growth Time and Wait Time Comparison Models 97

3.4.3 Bubble Period, Growth Time and Wait Time Results 98

3.5 Bubble Departure Diameter 99

3.5.1 Bubble Departure Diameter Post-Processing 100

3.5.2 Bubble Departure Comparison Model 101

3.5.3 Bubble Departure Diameter Results 102

3.6 Heat Flux Partitioning 104

3.6.1 Heat Flux Partitioning Post-Processing 104

3.6.2 Heat Flux Partitioning Comparison Model 106

3.6.3 Heat Flux Partitioning Results 107

3.7 Critical Heat Flux Values 115

4 Uncertainty Analysis **119**

4.1 Pressure 119

4.2 Subcooling 119

4.3 Mass Flux 120

4.4 Camera Timing and Synchronization 120

4.5 Surface Temperature 120

4.6 Surface Heat Flux 121

4.7 Nucleation Site Density 122
4.8 Bubble Period, Growth Time and Wait Time 122
4.9 Bubble Departure Diameter 123
4.10 Heat Flux Partitioning 124

5 Summary and Conclusions **125**
5.1 Summary 125
5.2 Conclusions 126
5.3 Technical Contributions 127
5.4 Suggested Future Work 128
5.4.1 Separate Effects Testing and Characterization of Nucleation Sites 128
5.4.2 Fluorine Tin Oxide 129
5.4.3 Elongated Heater Testing 129
5.4.4 Next Generation Infrared Cameras 130

A Boiling Curves and Nucleation Site Density Data **139**

B Heat Transfer Coefficient and Nucleation Site Density **149**

C Bubble Period, Growth Time and Wait Time Data **165**

D Heat Flux Partitioning Data **173**

List of Figures

1-1 (Left) Example of gas embryo in nucleation cavity, (Right) Example of bubble formation 31

1-2 Example of complete boiling curve. Region I: Single-phase, Region II: Nucleate Boiling, Region III: Transition Boiling, Region IV: Film Boiling 34

1-3 Comparison of IR capabilities of published IR thermometry research. Window size is given in parentheses. 43

2-1 Complete view of flow loop with test section column and diagnostic placement. Refer to Table 2.1 for labeling of components. 46

2-2 Schematic of the high-pressure flow loop. 47

2-3 Grundfos CRNE 3-12 X-FGJ-G-F-HQQ circulation pump attached with 4-1/4" Class 150 flanges. 48

2-4 Flexicraft Hydropad HY12 pressurizer. 50

2-5 Inline water filter. 50

2-6 PermSelect degassing system. Connections on the right side are flow inlet and outlet, connections on the left are vacuum ports. 51

2-7 Image of test section. 53

2-8 Results of finite-element stress analysis for the quartz major window. 56

2-9 Results of finite-element stress analysis for the quartz minor window. 56

2-10 Exploded view of the test section assembly. 57

2-11 Cross-section view of the test section assembly. 58

2-12 Results of finite-element stress analysis for Shapal heater cartridge. . 60

2-13 Exploded view of cartridge assembly (Left). View of assembled cartridge with ITO heater (Right). 61

2-14 (Left) Exploded view of ITO heater. (Right) View of ITO heater . . 63

2-15 Schematic of BPS with IR Photodetector imaging ITO heater. The IR photodetector is connected to a switch between the power supply and silver pads. Schematic courtesy of Artyom Kossolapov. 66

2-17 Schematic of the polarity switching system. The relays open and close in pairs as designated by their color coding. 69

2-18 Picture of the orientation of the HSV and IR cameras with respect to the test section and heater. Also shown are the LED backlight and beam splitter used. 70

2-19 Example of stepped power curve for 1 bar, 10 K subcooling, 1000 $\frac{kg}{m^2 s}$ flow rate. 73

2-20 Measured heat flux (via current and voltage measurement) and measured counts from IR camera. The counts reach steady-state approximately the same time the power input reaches a plateau. Also note the frames where the PSS is triggered and there is no power input resulting a briefly diminished value of counts. 74

3-1 Test matrix for pressurized subcooled flow boiling experiment. The color associated with each regime indicates which heater was used to conduct the test. 76

3-2 Multiple absorption and reflection determining the apparent backward emissivity $\epsilon^{-}_{\lambda,app}$. 81

3-3 Multiple absorption and reflection determining the apparent forward emissivity $\epsilon^{+}_{\lambda,app}$ 82

3-4 Top view of the discretized domain (x-y mesh). 84

3-5 Flow chart of the coupled conduction-radiation model. 85

3-6 Sample output of the coupled radiation-conduction model. On the left is the 2-D surface temperature distribution, on the right is the 2-D surface heat flux distribution. 86

3-7 Boiling curves for 20 K subcooling and 1500 $\frac{kg}{m^2 s}$ mass flux with varying pressure at 1, 2 and 5 bar. The 1, 2 and 5 bar tests shown here were conducted on the "Yellow", "Green" and "Blue" heaters, respectively. See Figure 3-1. 87

3-8 Boiling curves for 1 bar pressure and 1500 $\frac{kg}{m^2 s}$ with varying subcooling at 5, 10 and 20 K below T_{sat}. The 5, 10 and 20 K subcooling tests shown here were conducted on the "Red", "Green", and "Yellow" heaters, respectively. See Figure 3-1. 87

3-9 Boiling curves for 2 bar pressure and 10 K subcooling with varying mass flux at 1000, 1500 and 2000 $\frac{kg}{m^2 s}$. All tests shown here were conducted on the "Blue" heater. See Figure 3-1. 88

3-10 "Activity map" for 1 bar, 5 K, 1000 $\frac{kg}{m^2 s}$ 91

3-11 Nucleation site density result for 10 K, 1000 $\frac{k}{m^2 s}$, 1, 2 and 5 bar. Shown on the left is the boiling curve for reference. The 1 bar and 2 bar data was collected using the "Green" heater, the 5 bar data was collected using the "Blue" heater. See Figure 3-1. 93

3-12 Comparison of experimentally measured nucleation site density to the Hibiki-Ishii model for nucleation site density for 10K subcooling at 1000 $\frac{kg}{m^2 s}$. 93

3-13 Boiling curve and nucleation site density for 2 bar, 5K and all mass fluxes. The 1000 and 1500 $\frac{kg}{m^2 s}$ data was collected using the "Green" heater and the 2000 $\frac{kg}{m^2 s}$ data was collected using the "Red" heater. See Figure 3-1. 94

3-14 Depiction of the algorithm used to determine the growth time and wait time. 96

3-15 Comparison of experimental data for bubble period, growth time and wait time to models. 99

3-16 An accepted bubble departure diameter from the bubble departure diameter algorithm. Image courtesy of Ravikishore Kommajosyula . . 101

3-17 An accepted bubble departure diameter from the bubble departure diameter algorithm. Image courtesy of Ravikishore Kommajosyula . . 103

3-18 An accepted bubble departure diameter from the bubble departure diameter algorithm. Image courtesy of Ravikishore Kommajosyula . . 104

3-19 Dry area fraction as a function of applied heat flux. Also shown is a heat flux distribution from a single IR frame. The areas encircled in white are the dry regions. 105

3-20 Schematic of the effect of the K term from the RPI model for the quenching heat flux. 107

3-21 Experimentally measured fractional heat flux partitioning for 1 bar pressure, 10 K subcooling and 1000 $\frac{kg}{m^2s}$ test case. 109

3-22 Experimentally measured total heat flux partitioning for 1 bar pressure, 10 K subcooling and 1000 $\frac{kg}{m^2s}$ test case. 109

3-23 Comparison of the experimental measured heat flux partitioning and the heat flux partitioning results from the RPI model using the experimental measured boiling variables as inputs. The operating condition is 1 bar, 10 K, 1000 $\frac{kg}{m^2s}$ 111

3-24 The fractional boiling area used for the quenching term in the RPI model. The operating condition is 1 bar, 10 K, 1000 $\frac{kg}{m^2s}$ 112

3-25 The experimentally measured fractional boiling area. The operating condition is 1 bar, 10 K, 1000 $\frac{kg}{m^2s}$ 112

3-26 Comparison of the experimental measured heat flux partitioning and the heat flux partitioning results from the RPI model using the experimental measured boiling variables as inputs. 113

3-27 The boiling curve (left) and heat transfer coefficient against nucleation site density (right) is shown for 1 bar and 10 K regimes. 115

3-28 Tabulated values for the point of critical heat flux for each condition in the test matrix. The cell color indicates which heater was used for the test. 116

3-29 Tabulated values for the expected point of critical heat flux for each condition in the test matrix calculated using the Groeneveld Look-up Tables [57]. 118

4-1 Depiction of the error in the growth time due to the camera integration time. 123

5-1 Elongated ITO-sapphire heater for tests with a longer heated length. Image Courtesy of Megan McCandless 130

A-1 Boiling curve and nucleation site density for 5 K, 1000 $\frac{kg}{m^2 s}$ all pressures.139

A-2 Boiling curve and nucleation site density for 5 K, 1500 $\frac{kg}{m^2 s}$ all pressures.140

A-3 Boiling curve and nucleation site density for 5 K, 2000 $\frac{kg}{m^2 s}$ all pressures.140

A-4 Boiling curve and nucleation site density for 10 K, 1000 $\frac{kg}{m^2 s}$ all pressures.140

A-5 Boiling curve and nucleation site density for 10 K, 1500 $\frac{kg}{m^2 s}$ all pressures.141

A-6 Boiling curve and nucleation site density for 10 K, 2000 $\frac{kg}{m^2 s}$ all pressures.141

A-7 Boiling curve and nucleation site density for 20 K, 1000 $\frac{kg}{m^2 s}$ all pressures.141

A-8 Boiling curve and nucleation site density for 20 K, 1500 $\frac{kg}{m^2 s}$ all pressures.142

A-9 Boiling curve and nucleation site density for 20 K, 2000 $\frac{kg}{m^2 s}$ all pressures.142

A-10 Boiling curve and nucleation site density for 1 bar, 5 K all mass fluxes. 142

A-11 Boiling curve and nucleation site density for 1 bar, 10 K all mass fluxes.143

A-12 Boiling curve and nucleation site density for 1 bar, 20 K all mass fluxes.143

A-13 Boiling curve and nucleation site density for 2 bar, 5 K all mass fluxes. 143

A-14 Boiling curve and nucleation site density for 2 bar, 10 K all mass fluxes.144

A-15 Boiling curve and nucleation site density for 2 bar, 20 K all mass fluxes.144

A-16 Boiling curve and nucleation site density for 5 bar, 5 K all mass fluxes. 144

A-17 Boiling curve and nucleation site density for 5 bar, 10 K all mass fluxes.145

A-18 Boiling curve and nucleation site density for 5 bar, 20 K all mass fluxes.145

A-19 Boiling curve and nucleation site density for 1 bar, 1000 $\frac{kg}{m^2 s}$ all subcoolings. 145
A-20 Boiling curve and nucleation site density for 1 bar, 1500 $\frac{kg}{m^2 s}$ all subcoolings. 146
A-21 Boiling curve and nucleation site density for 1 bar, 2000 $\frac{kg}{m^2 s}$ all subcoolings. 146
A-22 Boiling curve and nucleation site density for 2 bar, 1000 $\frac{kg}{m^2 s}$ all subcoolings. 146
A-23 Boiling curve and nucleation site density for 2 bar, 1500 $\frac{kg}{m^2 s}$ all subcoolings. 147
A-24 Boiling curve and nucleation site density for 2 bar, 2000 $\frac{kg}{m^2 s}$ all subcoolings. 147
A-25 Boiling curve and nucleation site density for 5 bar, 1000 $\frac{kg}{m^2 s}$ all subcoolings. 147
A-26 Boiling curve and nucleation site density for 5 bar, 1500 $\frac{kg}{m^2 s}$ all subcoolings. 148
A-27 Boiling curve and nucleation site density for 5 bar, 2000 $\frac{kg}{m^2 s}$ all subcoolings. 148

B-1 Boiling Curves (left), Heat Transfer Coefficient versus Nucleation Site Density (right) for 5 K, 1000 $\frac{kg}{m^2 s}$, 1 and 2 bar. 150
B-2 Boiling Curves (left), Heat Transfer Coefficient versus Nucleation Site Density (right) for 5 K, 1500 $\frac{kg}{m^2 s}$, 1 and 2 bar. 150
B-3 Boiling Curves (left), Heat Transfer Coefficient versus Nucleation Site Density (right) for 5 K, 2000 $\frac{kg}{m^2 s}$, 1 and 2 bar. 151
B-4 Boiling Curves (left), Heat Transfer Coefficient versus Nucleation Site Density (right) for 10 K, 1000 $\frac{kg}{m^2 s}$, 1 and 2 bar. 151
B-5 Boiling Curves (left), Heat Transfer Coefficient versus Nucleation Site Density (right) for 10 K, 1500 $\frac{kg}{m^2 s}$, 1 and 2 bar. 152

B-6 Boiling Curves (left), Heat Transfer Coefficient versus Nucleation Site Density (right) for 10 K, 2000 $\frac{kg}{m^2 s}$, 1 and 2 bar. 152
B-7 Boiling Curves (left), Heat Transfer Coefficient versus Nucleation Site Density (right) for 20 K, 1000 $\frac{kg}{m^2 s}$, 1 and 2 bar. 153
B-8 Boiling Curves (left), Heat Transfer Coefficient versus Nucleation Site Density (right) for 20 K, 1500 $\frac{kg}{m^2 s}$, 1 and 2 bar. 153
B-9 Boiling Curves (left), Heat Transfer Coefficient versus Nucleation Site Density (right) for 20 K, 2000 $\frac{kg}{m^2 s}$, 1 and 2 bar. 154
B-10 Boiling Curves (left), Heat Transfer Coefficient versus Nucleation Site Density (right) for 1 bar, 5 K all mass fluxes. 154
B-11 Boiling Curves (left), Heat Transfer Coefficient versus Nucleation Site Density (right) for 1 bar, 10 K all mass fluxes. 155
B-12 Boiling Curves (left), Heat Transfer Coefficient versus Nucleation Site Density (right) for 1 bar, 20 K all mass fluxes. 155
B-13 Boiling Curves (left), Heat Transfer Coefficient versus Nucleation Site Density (right) for 2 bar, 5 K all mass fluxes. 156
B-14 Boiling Curves (left), Heat Transfer Coefficient versus Nucleation Site Density (right) for 2 bar, 10 K all mass fluxes. 156
B-15 Boiling Curves (left), Heat Transfer Coefficient versus Nucleation Site Density (right) for 2 bar, 20 K all mass fluxes. 157
B-16 Boiling Curves (left), Heat Transfer Coefficient versus Nucleation Site Density (right) for 5 bar, 5 K all mass fluxes. 157
B-17 Boiling Curves (left), Heat Transfer Coefficient versus Nucleation Site Density (right) for 5 bar, 10 K all mass fluxes. 158
B-18 Boiling Curves (left), Heat Transfer Coefficient versus Nucleation Site Density (right) for 5 bar, 20 K all mass fluxes. 158
B-19 Boiling Curves (left), Heat Transfer Coefficient versus Nucleation Site Density (right) for 1 bar, 1000 $\frac{kg}{m^2 s}$ all subcoolings. 159
B-20 Boiling Curves (left), Heat Transfer Coefficient versus Nucleation Site Density (right) for 1 bar, 1500 $\frac{kg}{m^2 s}$ all subcoolings. 159

B-21 Boiling Curves (left), Heat Transfer Coefficient versus Nucleation Site Density (right) for 1 bar, 2000 $\frac{kg}{m^2 s}$ all subcoolings. 160

B-22 Boiling Curves (left), Heat Transfer Coefficient versus Nucleation Site Density (right) for 2 bar, 1000 $\frac{kg}{m^2 s}$ all subcoolings. 160

B-23 Boiling Curves (left), Heat Transfer Coefficient versus Nucleation Site Density (right) for 2 bar, 1500 $\frac{kg}{m^2 s}$ all subcoolings. 161

B-24 Boiling Curves (left), Heat Transfer Coefficient versus Nucleation Site Density (right) for 2 bar, 2000 $\frac{kg}{m^2 s}$ all subcoolings. 161

B-25 Boiling Curves (left), Heat Transfer Coefficient versus Nucleation Site Density (right) for 5 bar, 1000 $\frac{kg}{m^2 s}$ all subcoolings. 162

B-26 Boiling Curves (left), Heat Transfer Coefficient versus Nucleation Site Density (right) for 5 bar, 1500 $\frac{kg}{m^2 s}$ all subcoolings. 162

B-27 Boiling Curves (left), Heat Transfer Coefficient versus Nucleation Site Density (right) for 5 bar, 2000 $\frac{kg}{m^2 s}$ all subcoolings. 163

C-1 Bubble period, growth time and wait time for 5 K, 1000 $\frac{kg}{m^2 s}$, 1 and 2 bar. 165

C-2 Bubble period, growth time and wait time for 5 K, 1500 $\frac{kg}{m^2 s}$, 1 and 2 bar. 166

C-3 Bubble period, growth time and wait time for 5 K, 2000 $\frac{kg}{m^2 s}$, 1 and 2 bar. 166

C-4 Bubble period, growth time and wait time for 10 K, 1000 $\frac{kg}{m^2 s}$, 1 and 2 bar. 166

C-5 Bubble period, growth time and wait time for 10 K, 1500 $\frac{kg}{m^2 s}$, 1 and 2 bar. 167

C-6 Bubble period, growth time and wait time for 10 K, 2000 $\frac{kg}{m^2 s}$, 1 and 2 bar. 167

C-7 Bubble period, growth time and wait time for 20 K, 1000 $\frac{kg}{m^2 s}$, 1 and 2 bar. 167

C-8 Bubble period, growth time and wait time for 20 K, 1500 $\frac{kg}{m^2s}$, 1 and 2 bar. 168
C-9 Bubble period, growth time and wait time for 20 K, 2000 $\frac{kg}{m^2s}$, 1 and 2 bar. 168
C-10 Bubble period, growth time and wait time for 1 bar, 5 K all mass fluxes.168
C-11 Bubble period, growth time and wait time for 1 bar, 10 K all mass fluxes.169
C-12 Bubble period, growth time and wait time for 1 bar, 20 K all mass fluxes.169
C-13 Bubble period, growth time and wait time for 2 bar, 5 K all mass fluxes.169
C-14 Bubble period, growth time and wait time for 2 bar, 10 K all mass fluxes.170
C-15 Bubble period, growth time and wait time for 2 bar, 20 K all mass fluxes.170
C-16 Bubble period, growth time and wait time for 1 bar, 1000 $\frac{kg}{m^2s}$ all subcoolings. 170
C-17 Bubble period, growth time and wait time for 1 bar, 1500 $\frac{kg}{m^2s}$ all subcoolings. 171
C-18 Bubble period, growth time and wait time for 1 bar, 2000 $\frac{kg}{m^2s}$ all subcoolings. 171
C-19 Bubble period, growth time and wait time for 2 bar, 1000 $\frac{kg}{m^2s}$ all subcoolings. 171
C-20 Bubble period, growth time and wait time for 2 bar, 1500 $\frac{kg}{m^2s}$ all subcoolings. 172
C-21 Bubble period, growth time and wait time for 2 bar, 2000 $\frac{kg}{m^2s}$ all subcoolings. 172

D-1 Heat Flux Partitioning for 1bar, 5 K, 1000 $\frac{kg}{m^2s}$ 174
D-2 Heat Flux Partitioning for 2bar, 5 K, 1000 $\frac{kg}{m^2s}$ 174
D-3 Heat Flux Partitioning for 1bar, 5 K, 1500 $\frac{kg}{m^2s}$ 175
D-4 Heat Flux Partitioning for 2bar, 5 K, 1500 $\frac{kg}{m^2s}$ 175
D-5 Heat Flux Partitioning for 1bar, 5 K, 2000 $\frac{kg}{m^2s}$ 176
D-6 Heat Flux Partitioning for 2bar, 5 K, 2000 $\frac{kg}{m^2s}$ 176
D-7 Heat Flux Partitioning for 1bar, 10 K, 1000 $\frac{kg}{m^2s}$ 177

D-8 Heat Flux Partitioning for 2bar, 10 K, 1000 $\frac{kg}{m^2 s}$ 177
D-9 Heat Flux Partitioning for 1bar, 10 K, 1500 $\frac{kg}{m^2 s}$ 178
D-10 Heat Flux Partitioning for 2bar, 10 K, 1500 $\frac{kg}{m^2 s}$ 178
D-11 Heat Flux Partitioning for 1bar, 10 K, 2000 $\frac{kg}{m^2 s}$ 179
D-12 Heat Flux Partitioning for 2bar, 10 K, 2000 $\frac{kg}{m^2 s}$ 179
D-13 Heat Flux Partitioning for 1bar, 20 K, 1000 $\frac{kg}{m^2 s}$ 180
D-14 Heat Flux Partitioning for 2bar, 20 K, 1000 $\frac{kg}{m^2 s}$ 180
D-15 Heat Flux Partitioning for 1bar, 20 K, 1500 $\frac{kg}{m^2 s}$ 181
D-16 Heat Flux Partitioning for 2bar, 20 K, 1500 $\frac{kg}{m^2 s}$ 181
D-17 Heat Flux Partitioning for 1bar, 20 K, 2000 $\frac{kg}{m^2 s}$ 182
D-18 Heat Flux Partitioning for 2bar, 20 K, 2000 $\frac{kg}{m^2 s}$ 182

List of Tables

1.1 Design criteria for 10 bar pressurized flow loop and test section. . . . 29

1.2 A list of boiling heat transfer variables 32

2.1 Reference labels for Figure 2-1. 47

2.2 Operational conditions for the PEThER flow loop. 49

2.3 Results of stress analysis for sapphire heater, quartz windows and Shapal cartridge 55

3.1 Summary of mechanisms for heat flux partitioning for the RPI model and the measured experimental data. 108

3.2 Variables used for RPI model and the method of measurement. 110

Chapter 1

Introduction

1.1 Motivation

The focus of this thesis is pressurized subcooled flow boiling, and in particular, the partitioning of the heat flux to water at the boiling surface up to the critical heat flux (CHF). Subcooled flow boiling is used in several applications, most notably in pressurized water reactors (PWR) to cool the reactor core. In the design of nuclear reactors, the heat transfer between the fuel rods, where the power is generated, and the coolant is of the utmost importance for both safety and profitability. When considering safety, understanding the limits of the heat transfer within the designed system is important in the prevention and mitigation of accidents. In particular, knowing the values of the CHF and the heat transfer coefficient with high certainty is important as the CHF is one of the factors that determines the maximum power at which the plant can safely operate [1]. Recently, efforts in predicting the heat transfer in subcooled nucleate flow boiling as well as the CHF using mechanistic models have yielded promising results [2]. However, before these new mechanistic models can proceed to application, they must be validated against experimental data sets which includes the boiling variables used, at a resolution capable of verifying the models results.

The CHF, as described in Section 1.4.2, is the maximum heat flux that can be achieved in the nucleate boiling regime before a departure from nucleate boiling

(DNB) occurs. The reactor must operate such that the CHF is never reached as doing so would result in fuel failure. The maximum heat flux at which the reactor can operate is a fraction of the value of the CHF and is dependent upon the margins of error in estimating the CHF value, the material properties, the heat transfer coefficient, and other engineering uncertainties [1]. These uncertainties are also dependent on the heat transfer models used for predicting the system performance. A predictive model that has been validated and verified with high certainty will have a lower margin of error when used to predict boiling heat transfer parameters such as the heat transfer coefficient or the value of the CHF. In turn, the lower margin of error will eventually allow the reactor to operate closer to the CHF value while maintaining the same safety standards. This has a significant impact on the profitability of the reactor as increasing the power output will enable the plant to provide more usable energy, increasing revenue, with a minimal increase in capital and operating costs.

Given the benefits of improving the understanding and modeling of boiling heat transfer, the motivation for this study of experimental subcooled flow boiling is clear. The data and understanding provided from this study will aid in the development, validation and verification of new boiling heat transfer models with better and more accurate predictive capabilities than previous models. The new models can then be applied to current and future nuclear reactors to improve their performance and safety standards.

1.2 Goals

Boiling heat transfer is leveraged in many applications due to the high heat transfer achievable compared to single-phase forced convection. Boiling is a complex phenomenon due to the presence of two phases in themodynamic non-equilibrium, liquid and vapor. Quantifying the heat transfer characteristics of boiling has proven to be difficult and many engineering applications have relied on empirical correlations with built-in margins of error to estimate the heat transfer characteristics. Unfortunately, these correlations are application specific and are generated with a large investment

of time and money.

Recently, there has been a paradigm shift in the approach taken to model boiling heat transfer. New models are using a ground-up approach, incorporating fundamental boiling parameters and building a mechanistic model to capture the physics of boiling [3]. These models show promise in more precisely quantifying the heat transfer coefficient in nucleate boiling as well as estimating the point of CHF, the maximum heat flux that can be reached before transitioning to film boiling. Most importantly, these models provide predictive capabilities over a wide range of flow and heat transfer regimes. This is in contrast with the current methods of using regime- and geometry- specific correlations which have limited application outside of their intended regimes.

However, before these new mechanistic and predictive models can be fully leveraged for engineering applications, they must first be validated against high-resolution experimental data. To date, no experimental data exist with the spatial and temporal resolution required for the validation of these models. This represents a significant gap in the field and can hinder the progress and acceptance of new boiling models.

The objective of this work is to provide the experimental data and understanding necessary to validate current mechanistic models and potentially inspire new models with greater predictive capabilities than those currently in use. Filling this gap in the field of boiling heat transfer will allow the models to progress forward in both refinement and, ultimately, acceptance and application to industrial practice.

To validate mechanistic flow boiling heat transfer models, the data set must consist of a complete set of fundamental boiling parameters including nucleation site density, bubble frequency, bubble departure diameter, growth and wait time, local surface temperature and heat flux distributions, and the heat flux partitioning. The benefit of collecting this data is two-fold. First, the individual boiling parameters can be benchmarked against predictive models for each individual parameter. More specifically, the nucleation site density can be compared to the Hibiki and Ishii model [4], the bubble departure frequency can be compared to the Cole model [5], the growth time and bubble departure diameter can be compared to the Mazzocco model [6] or the Zuber

model [7], and the wait time can be compared to the MIT wait time model [8] or the Podowski model [9]. Then the parameters can be combined to estimate the heat flux partitioning using an existing model such as those by Kurul et al. [10], Basu et al. [11] or Gilman and Baglietto [3]. The results can then be contrasted with the published results. Second, the directly measured heat flux partitioning can be bench-marked against the published data as well as the estimated partitioning from the buildup of the models using the experimentally measured boiling parameters. From this analysis it can be determined where the models are in agreement with the experimental data and where they can be improved. Moving forward, the experimental database created from this work can serve as a benchmark for new CFD and mechanistic boiling models as they are developed.

An additional objective, secondary to the collection of the experimental database, is the establishment of a benchmark facility for conducting pressurized flow boiling tests, including tests of CHF. Once complete, this facility can be used to further expand the pressurized flow boiling database or conduct other tests such as experiments studying the effects of engineered surfaces or incorporate additional diagnostic techniques such as Particle Imaging Velocimetry (PIV) or Laser Induced Fluorescence (LIF).

1.3 Objectives

1.3.1 Original Scientific Contributions

The scientific contributions for this work are as follows:

- The design and construction of unique pressurized subcooled flow boiling facility with the capability of synchronized measurement of the temperature and heat flux distributions at the boiling surface, up to CHF. Additionally, advanced post-processing techniques enable the measurement of the most complete set of simultaneously measured fundamental boiling parameters currently available. Consequently, this facility provides the most thorough investigation of subcooled

flow boiling phenomena available to date.

- The generation of an original database for a broad set of flow conditions, including pressure between 1 to 10 bar, subcoolings between 5 and 20 K and mass fluxes between 1000 and 2000 $\frac{kg}{m^2 s}$. At each condition, IR videos were collected at approximately 30 heat fluxes starting at single-phase heat transfer and ending at the CHF, producing over 1000 IR videos. For each heat flux, time-resolved surface temperature and heat flux distributions, nucleation site density, bubble departure diameter, bubble frequency, growth time and wait time are measured using image processing techniques. This work is the first to generate a database with the complete set of boiling parameters necessary to quantify the heat flux partitioning of an entire boiling surface.

- The first experimental direct measurement of the heat flux partitioning for pressurized subcooled flow boiling. Previous works have partitioned the heat flux for a single bubble in pool boiling but have not measured the whole surface heat flux partitioning. This is the first work to experimentally measure the heat flux partitioning across the entire heated surface. Moreover, this work is the first to do so in the flow boiling of water.

- Insight is provided in this thesis on the behavior of the measured boiling parameters and their trends when compared to predictive mechanistic models. In particular, the experimentally measured heat flux partitioning is compared to the predicted heat flux partitioning from Kurul and Podowski's model [10]. A discussion on the discrepancies is provided when there is a deviation between the predicted trends and the measured data.

1.3.2 Workflow

The primary goal of this work is collecting an experimental data set of subcooled flow boiling heat transfer parameters. To do so, a new subcooled flow boiling facility is needed in order to conduct the experiments and collect the data with the precision

and quality necessary for the validation of mechanistic flow boiling models.

The first step is designing a new test section capable of accommodating the flow and heat transfer regimes outlined in the test matrix, see Section 2.2, and the diagnostics needed for collecting the data. The geometry of the test section is similar to the one designed by Phillips [12]. The new test section incorporates changes meant to accommodate much higher pressures, up to 10 bar, and temperatures up to the corresponding saturation temperature. A complete list of design parameters is given in Table 1.1. The test section is also adaptable such that it can accommodate other types of experiments such as engineered surface testing, and other types of diagnostics such as particle imaging velocimetry and laser induced fluorescence.

The next step is to attach the new test section to an existing entrance region and flow loop. Using existing facilities, the new flow cell can be tested using an established flow facility. This simplifies troubleshooting and the development of standard operating procedures for setting up the diagnostic cameras and data collection procedures. A small set of reference experiments at atmospheric conditions (limited by the existing loop) can be carried out to collect a preliminary data set. The data gathered from these experiments can then be used to develop the post-processing analysis tools to quantify the boiling heat transfer parameters and heat flux partitioning.

A new flow boiling loop is necessary to accommodate high pressure testing and the incorporation of the new test section. The design criteria for the flow loop is given in Table 1.1. Special consideration is given to the water quality and treatment in the form of degassing and filtering systems. The flow loop is constructed on a similar support structure as the test section to allow for mobile transport. A shakedown of the new facility allows for a test of the electronics and flow control, and the development of standard operating procedures. The new facility is then leveraged to collect pressurized flow boiling data as outlined by the test matrix.

Upon completion of the experimental test matrix the data is post-processed to determine the boiling heat transfer parameters and heat flux partitioning. The parameters measured include: nucleation site density, nucleation frequency, growth time and wait time, bubble departure diameter and the heat flux partitioning. The mea-

sured parameters are summarized in Table 1.2. To do so, several MATLAB scripts are leveraged starting with a coupled radiation-conduction script to determine the 2-D surface temperature and heat flux distributions. Then nucleation sites are determined by examining the average activity map, which is discussed in Section 3.3. Finally, the complete heat flux partitioning and quantification of individual boiling parameters is carried out using several methods developed in-house.

The last step of this work is to use the analyzed data to compare with current flow boiling models, for both fundamental boiling parameters and the heat flux partitioning, to determine where the data is consistent and where the models may need refinement. The individual boiling parameters are bench-marked against published models and correlations and then input into established heat flux partitioning models. The result are then compared to the directly measured heat flux partitioning.

Parameter	**Design Criteria**
Pressure	Ambient to 10 bar
Temperature	Ambient to 180 C
Mass Flux	Maximum 2000 $\frac{kg}{m^2 s}$ without cavitation of the pump
Water Quality	Filtering and degassing systems
Temperature Diagnostics	Temperature probes monitoring test section, heat exchanger and pump inlet
Pressure Diagnostics	Pressure probes monitoring test section, pump inlet and outlet
Mass Flux Diagnostics	Turbine Flow Meter
Controls	Labview for pump control and monitoring
Flow Channel	3 cm x 1 cm to match existing entrance region
Flow Diagnostics	NPT ports for RTD's and presure transducers
Opitical Diagnostics	Optical access to boiling surface, simple and repeatable alignment
Heat Flux	Up to 10 $\frac{MW}{m^2}$
Electrical Connection	100V, 40A with a mechanical connection
ITO Heater	Compatible with current heater design, flexibility to incorporate new designs

Table 1.1: Design criteria for 10 bar pressurized flow loop and test section.

1.4 Background

1.4.1 Bubble Nucleation

Nucleate boiling is an extremely effective heat transfer process. When liquid is in contact with a heated surface, the heat transferred to the liquid will cause an increase in temperature through convection heat transfer. The liquid layer nearest to the heated surface will increase in temperature above the liquid bulk temperature, this is called the thermal boundary layer. In order for a bubble to nucleate, there must be a cavity in the heated surface with a small amount of entrapped vapor or non-condensable gas. Additionally, the liquid nearest the wall must reach a minimum superheat to initiate nucleation. The criteria for a bubble to grow from a cavity is described by the Hsu criterion [59], and is quantified by the Young-Laplace equation:

$$p_g - p_f = \frac{2\sigma}{r^*} \tag{1.1}$$

Where p_g and p_f are the gas and fluid pressures, respectively, σ is the surface tension between the two phases and r^* is the critical radius of the bubble. According to this criterion, a bubble can grow out of a cavity when the surface temperature reaches $T_{sat}(p_g)$

Once the growth process has started the bubble will grow very rapidly. Initially, the rate of the bubble growth will be limited by the movement of the liquid displaced by the bubble. This is called the inertia-controlled growth phase, as the bubble growth is limited by the inertia of the liquid it is displacing. Eventually, the bubble growth will be limited by the heat transfer at the perimeter and the base of the bubble, the thermally controlled growth phase. Vapor generation will originate from evaporation of the micro-layer at the base of the bubble, and the evaporation of the liquid in the thin superheated layer of liquid surrounding the bubble. The evaporation will be opposed by condensation at the top of the bubble when the bulk fluid is subcooled.

The bubble will grow until the forces pulling the bubble away from the surface (e.g. lift force or buoyancy force) are greater than the forces holding the bubble on

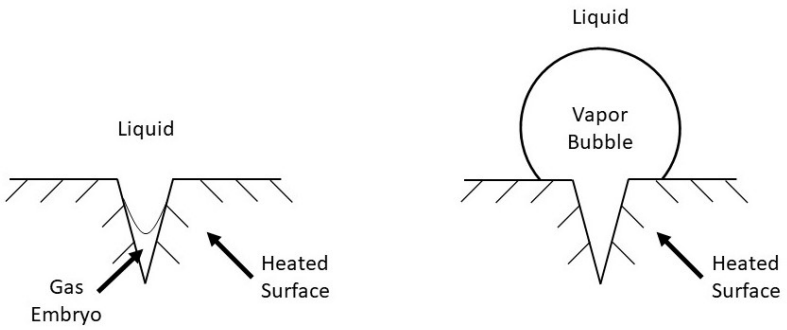

Figure 1-1: (Left) Example of gas embryo in nucleation cavity, (Right) Example of bubble formation

the surface (e.g. surface tension). The bubble will then lift off of the surface and fresh liquid will rush into the evacuated area and cool the surface before another bubble begins to grow. This cycle is called the ebullition cycle. Determining when the bubble will depart the surface depends upon the balance of forces on the bubble. Sugrue et al. [13] summarize these forces in a force balance model for determining bubble departure diameter, and Mozzocco et al. posited a mechanistic model for bubble departure diameter [6].

Nucleate boiling greatly increases the heat transfer between the wall and the coolant due to the large amounts of energy required during the phase change process and the rush of cool water that rapidly quenches the wall after bubble departure. The global enhancement due to boiling will scale with the bubble departure frequency and nucleation site density, that is, the number of nucleation sites on the surface actively forming bubbles. The total amount of heat transfer between the heated surface and bulk liquid in contact with the wall is quantified by a heat transfer coefficient.

$$q'' = h_{tc}(N''_{sd}, f) \cdot (T_{wall} - T_{bulk}) \tag{1.2}$$

Here q'' is the heat flux from the heated wall to the liquid, h_{tc} is the heat transfer coefficient, and T_{wall} and T_{bulk} are the wall temperature and bulk fluid temperature, respectively. However, due to the complex phenomena involved, accurately predicting the boiling heat transfer coefficient has proven difficult. Many engineering applica-

Variable	Notation	Units	Description
Wall Superheat	ΔT_{sup}	Celsius	Temperature of wall above the saturation temperature
Heat Flux	q''	$\frac{W}{m^2}$	Heat removed from solid surface into contacting liquid, per unit area
Bubble Departure Diameter	D_d	m	Diameter of bubble when departing from surface
Bubble Departure Frequency	f	Hz	Frequency at which bubble departs surface, inverse of sum of growth time and wait time
Growth Time	t_g	s	Time of growth period for bubble
Wait Time	t_w	s	Time after bubble departs until new bubble begins to nucleate
Nucleation Site Density	N''	$\frac{1}{m^2}$	Density of potential or active nucleation sites per unit area
Sliding Distance	l_s	m	Distance bubble slides along surface before departing
Dry Area Fraction	A_{dry}	m^2	Fraction of heated surface with vapor in-contact with the wall

Table 1.2: A list of boiling heat transfer variables

tions rely on correlations developed for specific geometries and test conditions. This approach is both expensive and time-consuming as a new correlation must be created for each application; requiring numerous tests, validation, and verification. A better approach is to construct a predictive model based on the physics involved to create a method for determining the heat transfer coefficient between the heated wall and the fluid. There are several fundamental physical parameters which can be used to quantify boiling heat transfer. They are summarized in Table 1.2. These parameters can be used as the building blocks for a mechanistic boiling model. Such a model could be applied to many applications without the need for additional experiments or validation as the physics can be adjusted to fit the regime in question.

1.4.2 Subcooled Flow Boiling

Flow boiling can occur horizontally or vertically, and in the case of vertical flow, it can be either upward-flow or downward-flow. The research presented here only concerns upward vertical flow. In subcooled flow the bulk flow temperature is below the liquid saturation temperature. The subcooling of the flow is defined as the difference between the saturation temperature at the system pressure and the bulk temperature of the liquid. Despite the bulk liquid temperature being below the saturation temperature, boiling can still occur if there is sufficient heat to establish a superheated thermal boundary layer sufficient for boiling. However, when bubbles begin to nucleate and detach from the wall, they will condense as they enter the bulk flow due to subcooled bulk temperature causing condensation of the vapor within the bubble.

Nucleate boiling heat transfer is often presented using a boiling curve, see Figure 1-2. The boiling curve plots the relationship between the wall temperature and the applied heat flux. The heat transfer coefficient is the slope of the curve. Typically experiments are conducted with a controlled heat flux, as such, the description of the behavior along the boiling curve follows increasing and decreasing heat flux.

The boiling curve can be broken up into four regions as noted on the figure, Region I: Single-Phase, Region II: Nucleate Boiling, Region III: Transition Boiling, and Region IV: Film Boiling. The first region shows a linear behavior between the wall temperature and heat flux. This region is the single-phase forced convection region where the heat transfer coefficient is constant. Region I ends at the onset of nucleate boiling (ONB). This is when the heat flux is sufficient to facilitate boiling but the nucleating bubbles do not necessarily depart from the surface. The start of the nucleate boiling regime, Region II, is characterized by an increase in the heat transfer coefficient (i.e. a change in the slope of the curve). This region continues until the CHF is reached. CHF marks when a departure from nucleate boiling (DNB) occurs and a transition to film boiling (Region IV) takes place with a dramatic increase in surface temperature. Most materials are unable to withstand such a large increase in temperature and typically fail if DNB occurs. As such, most applications involving

boiling heat transfer avoid CHF and many operate with a mandated margin of safety. The Leidenfrost point indicates where a transition from film boiling to nucleate boiling occurs. Note, Region III: Transition Boiling is only achievable in a temperature-controlled experiment.

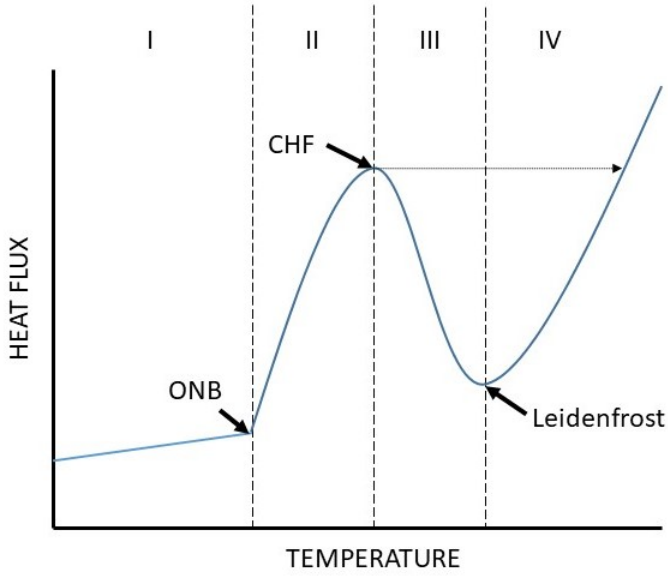

Figure 1-2: Example of complete boiling curve. Region I: Single-phase, Region II: Nucleate Boiling, Region III: Transition Boiling, Region IV: Film Boiling

1.4.3 Heat Flux Partitioning Modeling

One approach to mechanistically modeling boiling heat transfer is the so-called "Heat Flux Partitioning" approach. This approach was initially introduced by Judd and Hwang [14], but one of the most recognized heat flux partitioning schemes is the one proposed by Kurul and Podowski [10]. The concept is to identify the heat transfer mechanisms in nucleate boiling, and to partition the total heat flux into separate terms with each term attributed to a specific heat transfer mechanism. The result of the model is given in Equation 1.3.

$$q''_{total} = q''_{fc} + q''_{quench} + q''_{evap} \tag{1.3}$$

In this equation q''_{total} is the total heat flux from the heated surface to the liquid, q''_{fc} is the heat flux attributed to forced convection, q''_{quench} is the heat flux attributed to quenching, and q''_{evap} is the heat flux attributed to the evaporation. The single-phase forced convection term accounts for the surface area where nucleation is not occurring and liquid is always directly in contact with the wall. Quenching is the occurrence of cool liquid from the bulk flow rushing in to fill the volume previously occupied by the bubble. Additionally, a hot spot on the boiling surface is left behind when the bubble departs, due to the dry area at the base of the bubble where the micro-layer had been completely evaporated. When a bubble departs the surface it causes a disturbance of the thermal boundary layer, causing some mixing with the bulk flow. Before nucleation can occur again, the thermal boundary layer must be re-established such that the requisite superheat is present to initiate nucleation. The evaporation term accounts for the heat flux used for vapor generation due to departure. The term is quantified using the volume of the bubble. The equations for each of these terms is given in Equations 1.4-1.8.

$$q''_q = h_{quench}(\Delta T_{superheat} + \Delta T_{subcooling}) \tag{1.4}$$

$$h_{quench} = 2J_{quench} f \sqrt{\frac{\rho_l c_{pl} k_l t_w}{\pi}} \tag{1.5}$$

$$J_{quench} = K \frac{\pi D_d^2}{4} N'' \tag{1.6}$$

$$q''_e = \rho_v h_{fg} \frac{\pi}{6} D_d^3 N'' f \tag{1.7}$$

$$q''_{fc} = h_{fc}(\Delta T_{superheat} + \Delta T_{subcooling}) \tag{1.8}$$

Here h_{fc} and h_{quench} are the forced convection and quenching heat transfer coefficients, respectively. ρ is the density, c_p is the heat capacity, h_{fg} is the latent heat of vaporization, t_w is the wait time, f is the nucleation frequency, k is the thermal

conductivity, ΔT is the difference between the saturation temperature and the stated temperature, and K is the bubble area of influence, typically $K = 4$ [15].

Gilman et al. [3], have improved upon Podowski's model by including an additional term for flow boiling, sliding conduction. In flow boiling a bubble can depart a nucleation site in one of two methods, either the bubble can immediately lift-off the surface from the nucleation site and depart into the bulk flow, or the bubble can detach from the nucleation site and slide along the heated surface. A bubble departing the surface and entering the bulk flow will cause a quenching of the surface as previous described. However, a bubble sliding along the surface can cause a disturbance of the thermal boundary layer as it slides, leaving cool liquid to quench the surface in its wake. Gilman et al. introduced a new term q''_{sc} to account for this additional heat transfer mechanism.

$$q''_{total} = q''_{fc} + q''_{quench} + q''_{evap} + q''_{sc} \tag{1.9}$$

Initially, these heat flux partitioning models were empirical, and focused on predicting the wall heat flux or the fractional partitioning of the wall heat flux, see the review paper of Warrier and Dhir [16]. However, newer models have attempted to determine the wall heat flux as well as the partitioned heat fluxes through mechanistic modeling using fundamental boiling heat transfer parameters such as the ones outlined in Table 1.2. This first principles approach allows for an accurate prediction of the partitioned heat fluxes, given the appropriate physics. These can be combined using Equation 1.3 or 1.9 to quantify the total surface heat flux. Moreover, the model is general as long as the heat transfer regime still applies, making such models much more attractive compared to correlation-based models which have a very narrow range of applicability.

The experimental data presented in this thesis will be compared to established models, such as Kurul and Podowski's model, and can be used to inspire and validate new mechanistic models with greater predictive capabilities.

1.4.4 Infrared Thermometry

The principle diagnostic technique used in this work is called infrared (IR) thermometry. IR thermometry is the use of IR cameras to image an object and create a 2-D image of the surface of interest. In the field of boiling heat transfer, IR thermometry has been leveraged to image the boiling surface and create a 2-D time-dependent temperature distribution. For this work, a high-speed IR camera is used to image an ITO heater positioned on the wall of the channel to capture the boiling that occurs when the heater is energized.

The most common setup for IR thermometry boiling heat transfer experiments is to use an IR transparent substrate coated with an IR opaque thin-film, although other options are possible. Either the substrate or the thin-film is conductive, so Joule heating can be used to generate the necessary heat flux for boiling. The IR camera is then placed behind or underneath the heater to image the rear-side of the boiling surface through the IR transparent substrate. The thin-film layer is thin enough that it has negligible thermal resistance and capacitance, so the temperature on the rear-side of the film is the same as the temperature on the boiling surface. An example of an IR heater is given in Section 2.4.

The opaque thin-film must be emissive in the IR wavelengths where the IR camera can measure the emission from the heater. The optical properties of the thin-film, as well as the IR transparent substrate, can be determined using a Fourier Transform Infrared Spectrometer (FTIR). This device uses a reference light source and passes it through or reflects it off the material of interest. The resulting signal is then compared to the reference signal and analyzed using a Fourier transform to determine the frequency (or wavelength) dependence. The result is the determination of the transmission or reflection properties of the material depending upon the arrangement of the test. To determine the absorbance, Kirkoff's law of thermal radiation can be used:

$$\tau_\lambda + \rho_\lambda + \alpha_\lambda = 1 \tag{1.10}$$

Here, τ_λ is the transmittance, ρ_λ is the reflectance, and α_λ is the absorbance. Thus, the absorbance can be determined by the reflectance and transmittance at each measured wavelength. Moreover, it can be shown that:

$$\alpha_\lambda = \epsilon_\lambda \tag{1.11}$$

Where ϵ_λ is the emittance.

The choice of camera is dependent upon the object and temperatures of interest. The camera's range of sensitivity should align with the wavelengths where the object will emit the most light. This can be calculated using the Planck distribution or a more simple analysis could be done using Wien's displacement theory. IR cameras fall into one of three regions of interest, short-wave IR for wavelengths between 1-3 μm, mid-wave IR for wavelengths between 3-5 μm, and long-wave IR for wavelengths greater than 8 μm. For this work, and most other work involving boiling water at atmospheric and higher pressures, a mid-wave IR camera is the camera of choice.

Once the optical properties have been determined, a radiometric model of the heater can be made. This model describes the emission and propogation of light from the heater to the IR camera. As Bucci et al. [17] demonstrated, if such a radiometric model is coupled to a conduction model of the heater using the surface temperature distribution as a boundary condition to link the two models, both the surface temperature and surface heat flux distributions can be determined. For a highly thermally conductive substrate a three-dimensional conduction model should be applied to accurately determine the temperature distribution within the substrate. A one-dimensional model can be sufficient for substrates with a lower thermal conductivity or if a thermal insulation layer is included [18].

The last consideration when using the IR thermometry technique is the calibration and processing of the data. A proper calibration of the IR camera is necessary to reduce the uncertainty in the data. The calibration and post-processing techniques used in this work are discussed in Section 3.2.1.

1.5 Previous Research

Subcooled flow boiling has been an extensively studied field. There have been numerous experimental studies to develop correlations for specific flow geometries and flow regimes, such as the work by Jens and Lottes [19] which lead to the Jens-Lottes correlation for subcooled flow or Thom's work [20] on pressure drop in boiling channels. However, newer research has focused on developing mechanistic models rather than correlations specific to their application. With this new approach to modeling, flow boiling experiments have been evolving to incorporate new technologies to measure more boiling parameters in support of the development and validation of these mechanistic models. Notably, boiling heat transfer studies have begun to incorporate diagnostics such as IR thermometry, PIV, LIF, and High-Speed Video imaging (HSV). The work covered in this section is not a comprehensive review, but representative of the field and the direction it has taken.

One of the first implementations of IR thermometry to the study of boiling heat transfer was done by Sgheiza and Myer [21]. They used a 25.4 μm thick stainless-steel heater and imaged the rear-side of the heater using an IR camera operating at 60 frames per second with a maximum scan rate of 3,000 Hz. Pool boiling experiments were carried out at atmospheric pressure using degassed water. Sgheiza and Myer primarily focused on nucleation site identification, but also tracked transient temperatures during nucleation using a point scan method at a higher frame rate of 3000 frames per second. They were able to measure boiling curves, nucleation site density and bubble period.

Theofanous et al. [22, 23] implemented high-speed IR thermometry in a pool boiling experiment. They captured a 1 cm^2 surface with a resolution of 225 microns per pixel at 1000 frames per second. In the two part work, both nucleate boiling and CHF were investigated and boiling parameters such as nucleation site density and bubble period were quantified. They also investigated the origination and growth of the dry spots, both reversible and irreversible, that occur during CHF. In particular, they identified that the dry areas at the base of the bubble were the origin of the

larger CHF dry spot. When multiple bubbles coalesced, their dry areas also coalesced forming a large dry patch causing the initiation of the departure from nucleate boiling (DNB).

Golobic et al. [24] used an IR camera synchronized with a HSV camera to image a thin-foil heater in atmospheric pool boiling at saturation conditions. They achieved a spatial resolution of 40 microns at a frame rate of 1000 frames per second and imaged single bubbles nucleating to determine the temperature distribution at the bubble base. They found that their setup was insufficient in identifying the triple contact line of the bubble and suggested higher-speed equipment was necessary for precise identification. Despite this limitation, they were able to identify the transient behavior of the heat flux as the bubble grew. Initially, the heat flux would be highest at the center of the bubble where most of the evaporation occurred. As the bubble grew and the triple contact line moved outward, the maxima of the heat flux would follow. This would attribute the localized high heat flux to the evaporation of the micro-layer at the base of the bubble.

Gerardi et al. [25, 26] used an IR camera synchronized with a HSV camera for a study of nanofluids in atmospheric pool boiling. They used an Indium Tin Oxide (ITO) thin film as the heater and IR emissive layer, coated on a sapphire substrate. The IR camera imaged the boiling surface at a resolution of 100 microns per pixel at a frame rate of 500 frames per second. By imaging the boiling surface they were able to quantify boiling parameters such as the nucleation site density, growth and wait times, heat transfer coefficient, bubble departure diameter, and nucleation frequency. Gerardi et al. compared boiling in a nanofluid with deionized water, and found the nanofluids cause a drop in heat transfer coefficient while increasing the CHF value by as much as 100%.

Wagner and Stephan [27] conducted pool boiling experiments with refrigerants and used IR thermometry to capture the local surface temperature distributions. They achieved an extremely high-resolution of 14.5 microns at a frame rate of 978 frames per second, pushing very near the diffraction limit for IR cameras. They used FC-84 and FC-3284 and binary mixtures as their working fluid. They were able to quantify

bubble departure diameter, bubble departure frequency and growth and wait times for a single nucleation site.

Jung et al. [28] used IR thermometry to investigate CHF of FC-72 in atmospheric pool boiling. Their camera operated at 383 frames per second with a spatial resolution of 56 microns per pixel. They implemented an IR calibration technique developed by Kim et al. [18] which allows for the calibration of the camera signal using a coupled radiation-conduction algorithm using spectrally averaged optical properties and a 1-D conduction analysis. The post-processed IR images quantified the local 2-D temperature and heat flux distributions. Using these images they were able to track the contact line location as the dry spot developed during CHF. Based on their observations they gave a description of the process through which CHF occurs.

Jung and Kim [29] combined IR thermometry with a total internal reflection laser technique to simultaneously measure the temperature distributions and liquid-vapor phase distributions on the surface of a pool boiling heater. They were able to visualize the liquid micro-layer underneath the bubble where most of the evaporation occurs. They applied a conduction analysis to determine the wall-to-liquid heat flux, the micro-layer evaporation heat flux and the micro-layer conduction. Their results showed the micro-layer conduction was higher by an order of magnitude compared with the other heat fluxes, but noted the large discrepancy and suggested further analysis was required to draw a conclusion. Additionally, they saw the same shifting of heat flux throughout bubble growth as Golobic [24].

Phillips [12] used a combination of IR thermometry, HSV and PIV to develop a data set for subcooled flow boiling. He used an ITO-sapphire heater in a subcooled flow boiling environment to generate a data set of flow boiling parameters for validation of sliding conduction heat transfer model. A 2-D surface temperature distribution was measured using a empirical calibration curve. Departure diameter, departure frequency, growth and wait times and nucleation site density were quantified using a combination of IR and HSV images. He also reported the flow velocity distributions for a single nucleating bubble along with synchronized IR and HSV images.

Su et al. [30, 31] implemented synchronized IR thermometry and HSV in a study of transient nucleate boiling in both pool and flow boiling conditions at atmospheric pressures. An ITO-sapphire heater was used for heat generation and IR emission. They were able to capture an exponentially increasing heat flux at 2500 frames per second to accurately determine the onset of nucleate boiling under transient conditions. They found that the onset of nucleate boiling (ONB) temperature and heat flux increased with decreasing period and increasing subcooling.

Figure 1-3 shows the progression of IR thermometry studies to higher frame rates and better resolution. Notably, most of these studies have been limited to individual nucleation sites as the pixel array size has been limited on high-speed IR cameras. However, higher-resolutions and faster frame rates are possible with state-of-the-art IR cameras. In the future, frame rates as high as 10,000 frames per second will be achievable with 100 micron resolution or less with window sizes above 100 x 100 pixels, see Telops FASTM3K on Figure 1-3. As the technology improves, the applications to boiling heat transfer will improve as well. As demonstrated by this work, studies on whole heater areas are possible, where a complete heat flux partitioning analysis can occur as opposed to being limited to a single nucleation site where global effects can be missed. Additionally, the increased spatial resolution is needed to investigate high-pressure experiments, such as this work, where the bubble diameters will be significantly smaller. Bubble nucleation periods can be on the order of 1 ms in water [12], necessitating a minimum frame rate of 1000 frames per second to ensure the bubble is captured. Higher frames rates are necessary to capture separate stages of the ebullition cycle.

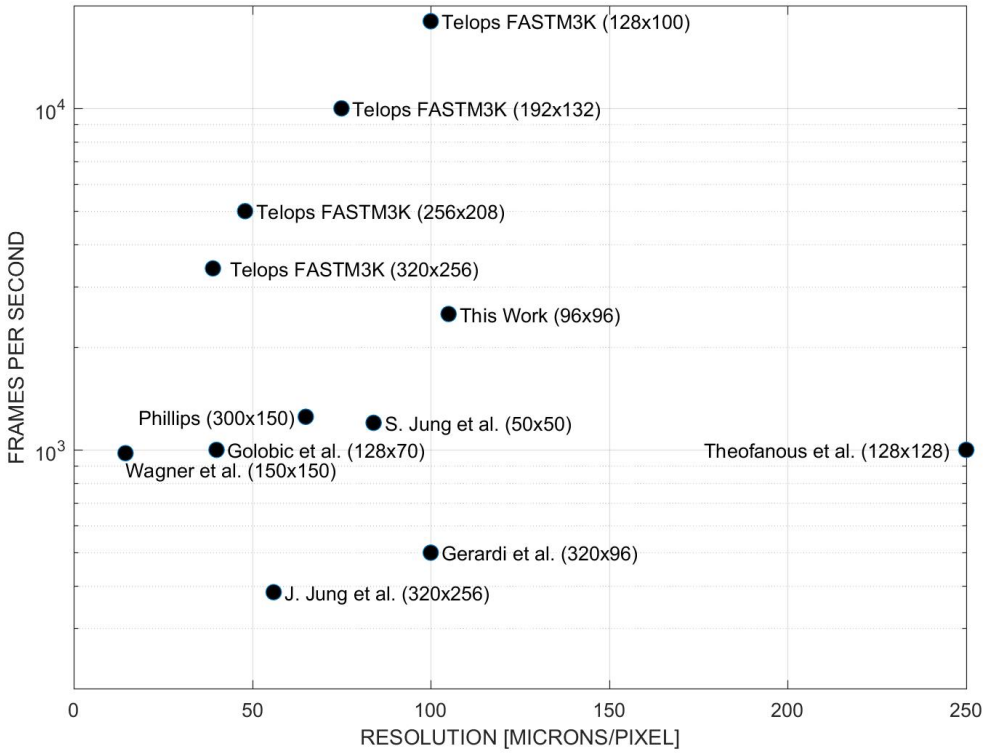

Figure 1-3: Comparison of IR capabilities of published IR thermometry research. Window size is given in parentheses.

Chapter 2

Experimental Apparatus and Methods

This chapter covers the experimental facility and methods used to conduct the subcooled flow boiling study outlined in Chapter 1. The Platform for Experimental Thermal-hydraulics Engineering Research (PEThER) is an experimental flow boiling facility designed, built, and operated by MIT's Department of Nuclear Science and Engineering. This facility is capable of conducting flow boiling tests up to 10 bar pressure at saturation temperature. It uses state-of-the-art diagnostics and control systems to collect high-resolution flow boiling data including capturing the establishment and growth of the DNB event.

2.1 Pressurized Flow Loop

A new flow loop was designed to accommodate the high-temperature and high-pressure conditions involved in this work. A picture of the flow loop is shown in Figure 2-1, a schematic is given in Figure 2-2. The design of the loop was inspired by a previous flow loop design by DeWitt for investigation of downward facing CHF [32]. That loop was later adapted by Phillips for subcooled boiling experiments at lower mass fluxes and pressures [12]. Improvements were incorporated into the new loop design based on lessons learned from the operation of the previous loop. Namely,

a significant focus was put on maintaining good water quality and degassing, and reducing the lead time required for executing experiments. The design requirements for the new loop are given in Table 1.1. The primary design criteria was compatibility with the high pressures and temperatures, 10 bar and 180°C, respectively, although each piece of equipment had additional criteria to follow.

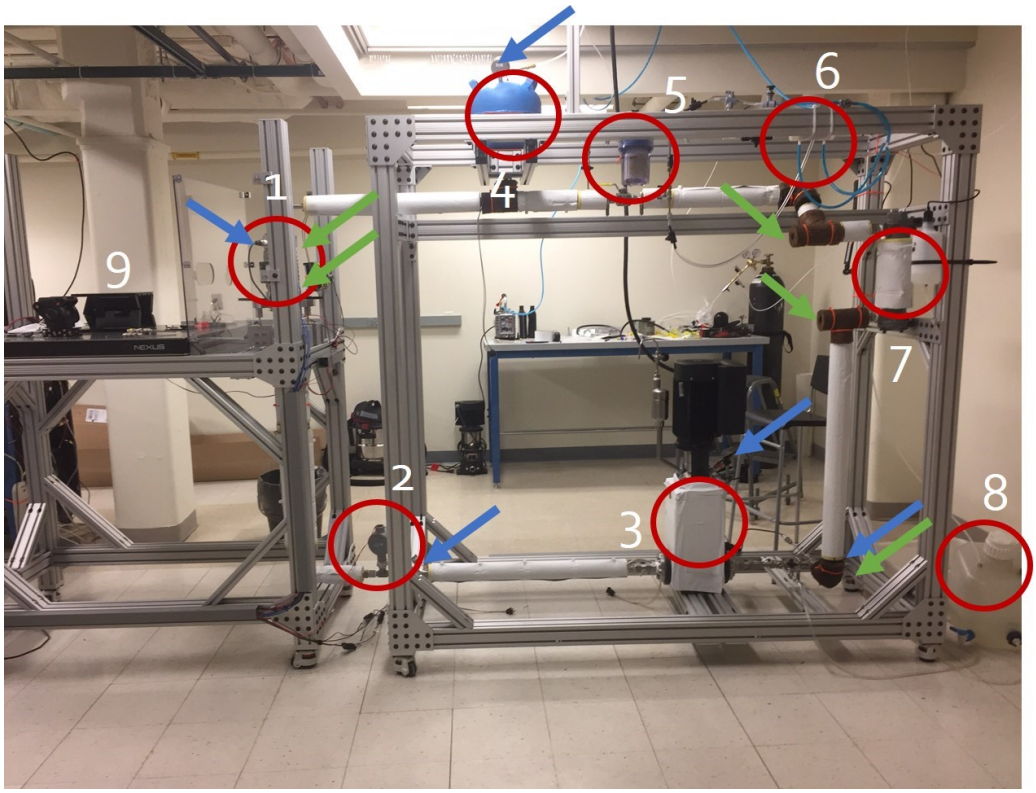

Figure 2-1: Complete view of flow loop with test section column and diagnostic placement. Refer to Table 2.1 for labeling of components.

The circulation pump chosen was the same used by DeWitt [32], a Grundfos CRNE 3-12 X-FGJ-G-F-HQQE, see Figure 2-3. This pump was chosen over other options because of previous operation experience. The pump is outfitted with the Grundfos Cool-Top which enables the pump to operate up to temperatures of 180°C[33]. This is a variable speed pump which allows for control of the flow rate by controlling the output pump head. The speed is controlled by inputting a voltage signal between 0 and 10V. The output of the pump scales roughly linearly with the voltage input, although a mass flow meter was used in series with the pump for accurate measurement of the flow rate. Mass fluxes up to 2000 $\frac{kg}{m^2 s}$ were achieved at all pressures when the

Blue Arrows	Pressure Transducer
Green Arrows	Thermocouple/RTD
1	Test Section
2	Turbine Flow Meter
3	Grundfos Circulation Pump
4	Pressurizer
5	Water Filter
6	Degassing Membrane
7	Heat Exchanger
8	Filling Tank
9	Diagnostic Camera Stage

Table 2.1: Reference labels for Figure 2-1.

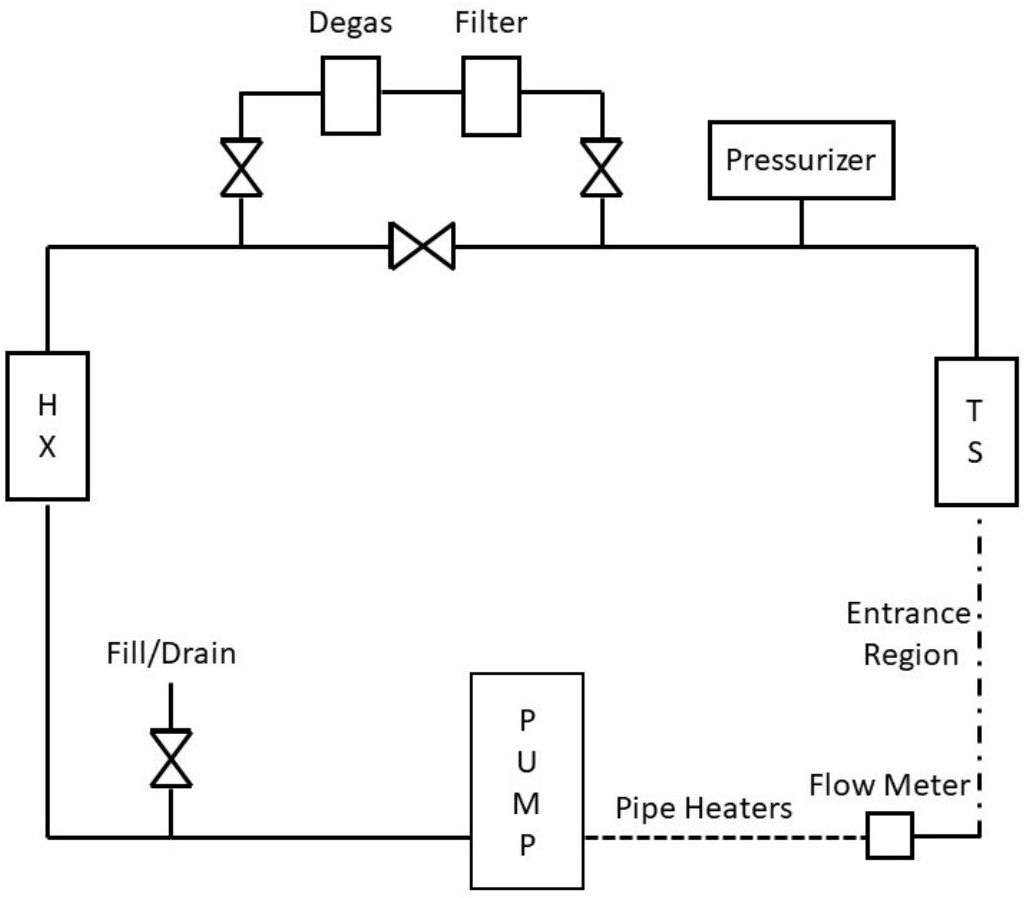

Figure 2-2: Schematic of the high-pressure flow loop.

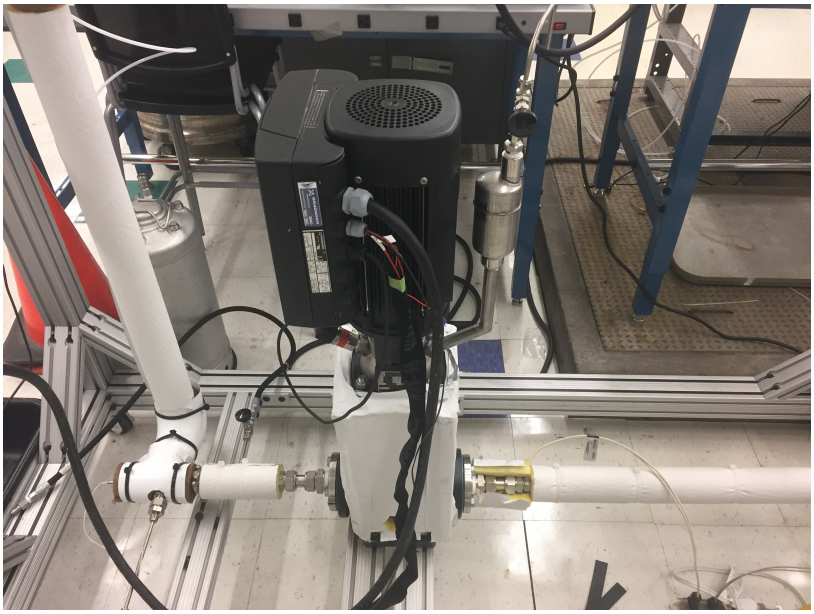

Figure 2-3: Grundfos CRNE 3-12 X-FGJ-G-F-HQQ circulation pump attached with 4-1/4" Class 150 flanges.

pump was operating at near maximum output.

The pressurizer used to set and maintain the pressure of the loop was a Flexicraft Hydropad HY12, see Figure 2-4. This part was selected from previous operational experience of a loop designed by Forrest [34]. The pressurizer is connected to the highest point of the main flow line as per the installation instructions [35]. The HY12 has all stainless-steel components on the wetted-side of the pressurizer [36]. The bellows separate the wetted-side from the gas chamber. The pressure is controlled by pressurizing the gas-side using an external gas source such as a nitrogen bottle. Pressurizing the gas chamber compresses the bellows and increases the pressure on the wetted-side, increasing the pressure within the loop. The bellows will also expand to compensate for thermal expansion of the water as the temperature of the loop rises. This helps maintain constant pressure within the loop throughout testing.

316 Stainless-steel tubing and fittings were used throughout the majority of the loop. A small part of the secondary water treatment loop consisted of plastic tubing because of the plastic degassing system. The tubing for the main flow line was predominantly 3/4" tubing, however 1" and 1-1/4" tubing was used for compatibility with certain components. 1/4" tubing was used on the secondary line. Most of the

Parameter	Range
Pressure	ambient - 10 bar
Temperature	ambient - 180 C
Mass Flux	0 - 2000 $\frac{kg}{m^2 s}$
Reynolds Number	0 - 60,000
Subcooling	0 - 75 K
Heat Flux	0 - 20 $\frac{MW}{m^2}$
Hydraulic Diameter	1.5 cm
Boiling Number	0 - 0.019
Prandtl Number	1.25 - 6.13
Equilibrium Quality	-0.1 - 0

Table 2.2: Operational conditions for the PEThER flow loop.

fittings and valves were manufactured by Swagelok. The fittings are rated up to 760 bar [37], while the valves were class 150 ball valves. In addition to the stainless-steel tubing, two flexible tubes were used, one before and one after the test section column. These tubes connected the flow loop to the test section column and allowed for simple alignment and attachment of the two sections.

To maintain high-quality water multiple filtering and degassing systems were included in the flow loop. A simple membrane water filter was used to filter contaminants and debris from the water, see Figure 2-5. In addition to the filter, a PermSelect degassing system, see Figure 2-6, was installed to remove non-condensable gases from the flow. This system uses a gas-permeable silicone membrane to separate the liquid flow from a vacuum [38]. The gases are pulled across the membrane by the pressure difference between the liquid and a vacuum created using a vacuum pump. The degassing chamber has four ports, an inlet and outlet for the flow and two ports to connect to a vacuum pump. This system allowed for adequate degassing after 2-3 hours of circulation. However, both the PermSelect system and the filter can only be operated near atmospheric temperatures and pressures.

For additional degassing at high temperatures, a high-point degassing line was installed above the test section. This method uses the installed heaters on the loop to boil the water in the test section column and allow the vapor bubbles to accumulate at the venting point. The non-condensable gases are purged along with the vapor ac-

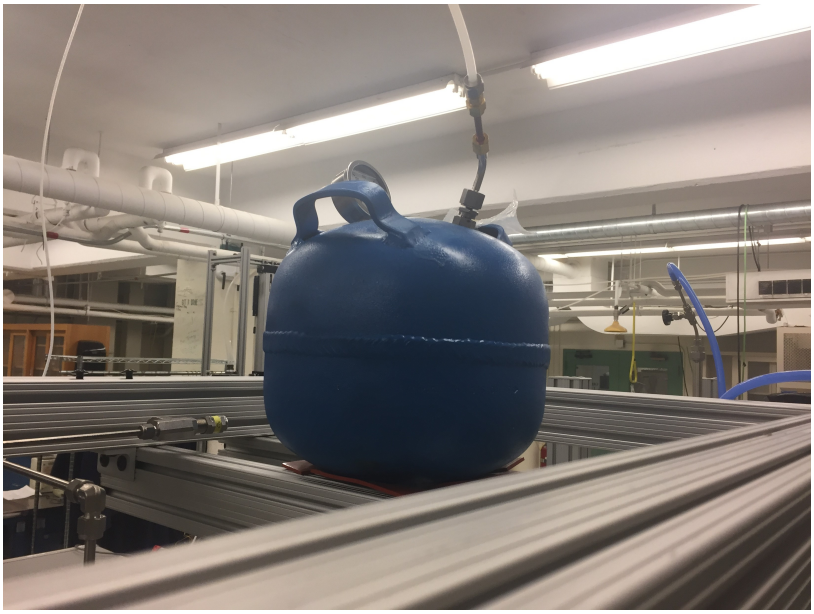

Figure 2-4: Flexicraft Hydropad HY12 pressurizer.

Figure 2-5: Inline water filter.

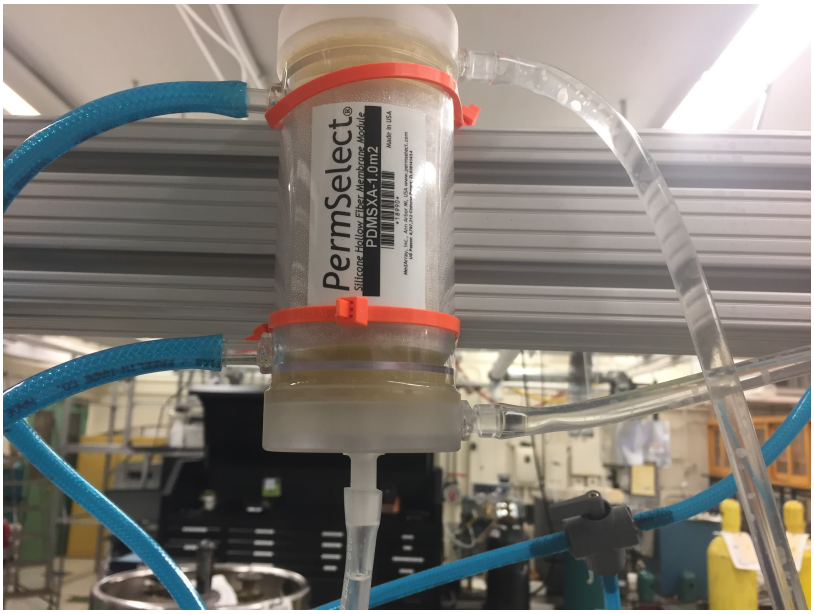

Figure 2-6: PermSelect degassing system. Connections on the right side are flow inlet and outlet, connections on the left are vacuum ports.

cumulation. The water is then mixed by cycling the loop and the process is repeated. This method allows for degassing at high temperatures and pressures.

A JB Industries vacuum pump was used for both initial vacuum pull of the loop and for the degassing system. It was necessary to install a moisture accumulator before the inlet of the vacuum pump to protect the pump from water slugs.

A heat exchanger was installed on the main line in order to cool the flow during high mass flux conditions. When high mass fluxes are required, the pressure drop across the whole loop can be quite large. This can cause cavitation of the pump due to the pressure at the inlet of the pump falling below the pressure required for a net positive suction head. The solution is to cool the water before it enters the pump, lowering the pressure required for a net positive suction head and preventing cavitation. However, when cooling the liquid, it must be reheated before it enters the test section. The preheater installed in the loop must provide enough power to make up the energy lost at the heat exchanger.

The heat exchanger was connected to the building process water supply. This provides water at 5 bars pressure near room temperature. A needle control valve was placed on the building supply line to control the flow rate of the water through the

secondary side of the chill line to limit the cooling of the primary side.

Pipe heaters were used as a preheater to heat the flow and maintain a constant temperature. Pipe heaters were chosen because of the ease of installation and the scalability. The heaters were wrapped around the 316 stainless steel tubing after the pump and provided a maximum of 1 kW of power. The power was controlled using a pair of variable transformers with each transformer controlling two heaters. This setup allowed the loop to reach 90 C from room temperature within an hour.

To monitor the flow rate a Series FTB-1400 turbine flow meter was used from Omega. The flow meter is constructed from 316 stainless-steel and can operate up to 180 C and 5000 psi [39].

2.2 Test Section

Perhaps the most integral part of the PEThER facility is the in-house designed test section. The test section provides several functions, but most notably contains the active heater and provides optical access to the heater for the HSV and IR cameras. The complete design criteria for the flow cell are given in Table 1.1. The geometry of the test section is based on a quartz test section designed by Phillips [12]. The primary difference between this test section and the one developed by Phillps is the capability of operating at higher pressures up to 10 bar and higher temperature up to 180°C.

The design of the test section started with identifying the constraints which the new design must adhere to. The first constraint was the reuse of an entrance region used by Phillips [12]. The entrance region has a 3 cm x 1 cm channel and provides a 60 L/D developing length in which the flow can reach a fully-developed flow conditions. This constraint determined the channel size as well as the connection between the test section and the entrance region. The other design constraint was the use of IR and HSV cameras as the primary diagnostics. This necessitated direct optical access to rear of the heater for the IR camera, and visible access to the front, rear and both sides of the heater for the HSV camera.

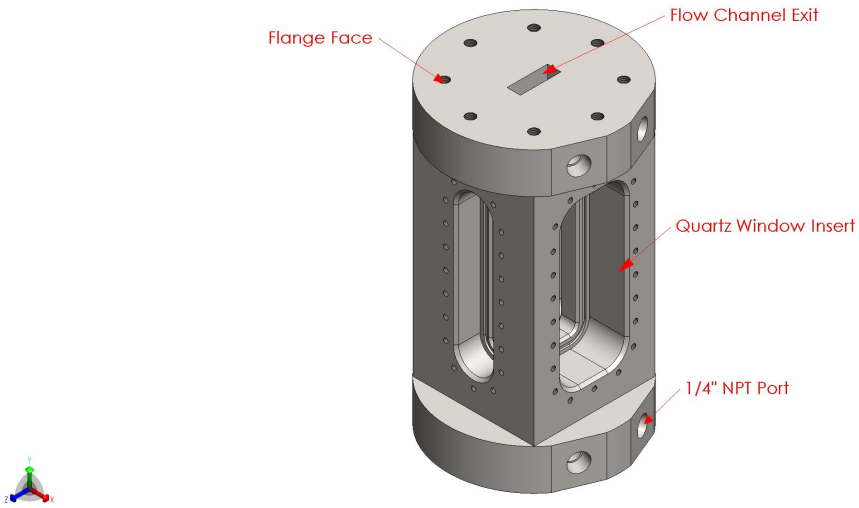

Figure 2-7: Image of test section.

The next step of the design was the choice of materials. 316 stainless steel was chosen for the body of the test section as it has a high tensile and compressive strength to withstand the pressurized environment, can withstand the 180°C saturation temperature, is chemically compatible with water and is easily machinable. Since optical access was needed for the front and side views, quartz windows were included in the design. Quartz was used by Phillips with much success as he was able to use both PIV and HSV for his tests. For the pressure and liquid seals, silicone o-rings were be used when ever possible to create a face seal as they can withstand up to 205°C, are easily compressible, and are purchasable in a variety of sizes and thicknesses [40]. The last component to consider was the heater cartridge, which is covered in Section 2.3.

Once the materials were chosen the design of the test section can begin to take shape. SolidWorks was used to create the CAD files and the technical drawings required for machining as well as run finite-element analysis to ensure the design would be able to withstand the stresses created from the high temperature and pressure.

The test section measures 22 cm tall and 12.7 cm in diameter at it's widest. The upper and lower sections are rounded while the mid-section is squared with each face parallel to a channel wall. The upper and lower faces are threaded for 5/16" screw

holes to fit the entrance region and flange. There are also four 1/4" NPT ports on the upper and lower sections with small holes that penetrate into the flow for pressure and temperature probes.

Each mid-section face is designed to accommodate either a quartz window or the heater cartridge. A tight-tolerance cutout extends up to the flow channel which enables the placement of either a window or cartridge to sit flush with the wall of the channel. A 1/16" o-ring groove allows for a face seal between the window/cartridge. The outer face of the wall is threaded with 1/4"-20 holes so a flange may be placed on the rear of the window/cartridge, separated by a protective PTFE gasket, and press the part against the o-ring to ensure a tight seal. Each of the quartz windows and the heater cartridge are 10 cm tall. The width of each is determined by the size of the channel wall, and the thickness was determined by running a finite-element analysis and providing a minimum 20% margin for safety. A first estimate can be made using the equation in table 11.4, case 8a in Roark's Formulas for Stress and Strain [41] which gives the equation for maximum stress of a plate with fixed edges.

$$\sigma = \frac{\beta_x q b^2}{t^2} \tag{2.1}$$

$$y_{max} = \frac{\alpha W b^4}{E t^3} \tag{2.2}$$

Here, σ is the stress either at the center (in which case $x = 1$) or at the edge (in which case $x = 2$), and y_{max} is the maximum deflection of the plate. β_x is a dimensionless number which accounts for the aspect ratio of the plate, q is the applied pressure, b is the length of the longest edge, t is the thickness of the plate, α is another dimensionless number correlated to the aspect ratio of the plate, E is the Young's modulus of elasticity of the material, and W is the force applied. The first equation can be re-arranged to solve for the minimum thickness, given the pressure and yield strength of the material.

$$t = \sqrt{\frac{\beta_x q b^2}{\sigma}} \tag{2.3}$$

Using these equations an estimate of the thickness was determined as well as the margin of safety for that thickness.

Part	**Thickness (mm)**	**Yield Strength (MPa)**	**Max Stress (MPa)**	**Deflection (μm)**
Sapphire	1	760	123	5.07
Quartz Window 1	8	50	5.28	0.35
Quartz Window 2	8	50	18	4
Shapal Cartridge	9	300	18.12	2.17

Table 2.3: Results of stress analysis for sapphire heater, quartz windows and Shapal cartridge

The results of Table 2.3 show there is a large margin of safety for each of these parts. To confirm this calculation, a finite-element analysis of each part was conducted using The SolidWorks Simulation Package. The results of the quartz window finite-element simulations are shown in Figures 2-8 and 2-9. Additionally, a finite-element simulation was completed for the test section body as well to analyze the areas most likely to fail under high-stress. For the finite-element analysis, the rear edges were fixed while a 10 bar pressure load was placed on the front faces. This is a conservative analysis in that the rear of the windows and cartridge are normally supported by flanges and the net pressure load on the front faces should be 9 bar to account for the 1 bar pressure on the rear faces to account for atmospheric pressure in the laborartory.

Figure 2-10 shows an exploded isometric view of the test section assembly. Figure 2-11 shows a cross-section view of the test section for better understanding of the final assembly.

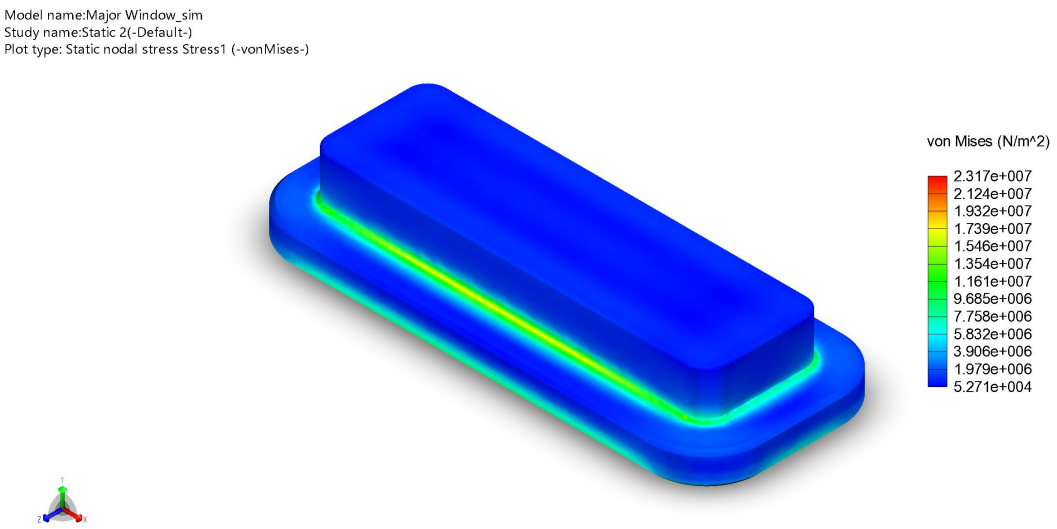

Figure 2-8: Results of finite-element stress analysis for the quartz major window.

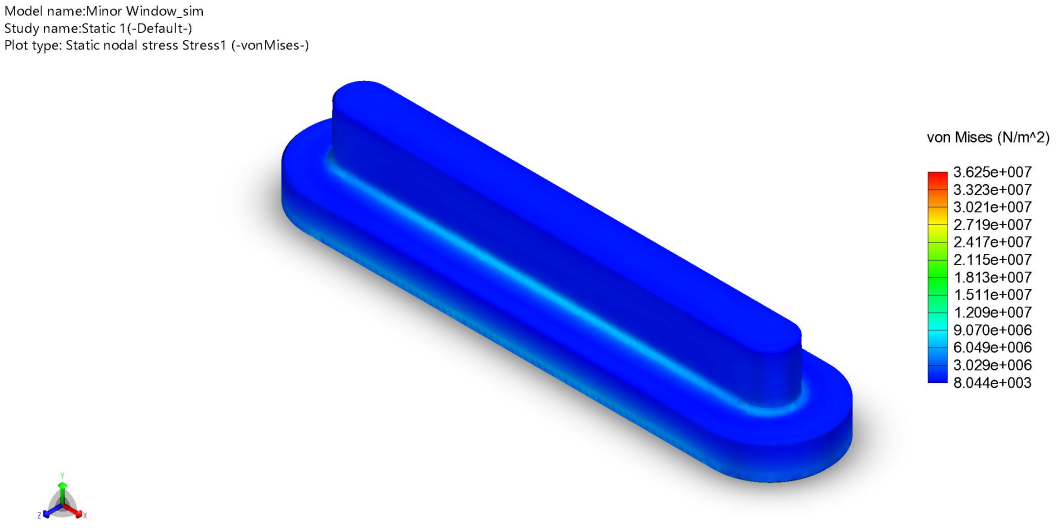

Figure 2-9: Results of finite-element stress analysis for the quartz minor window.

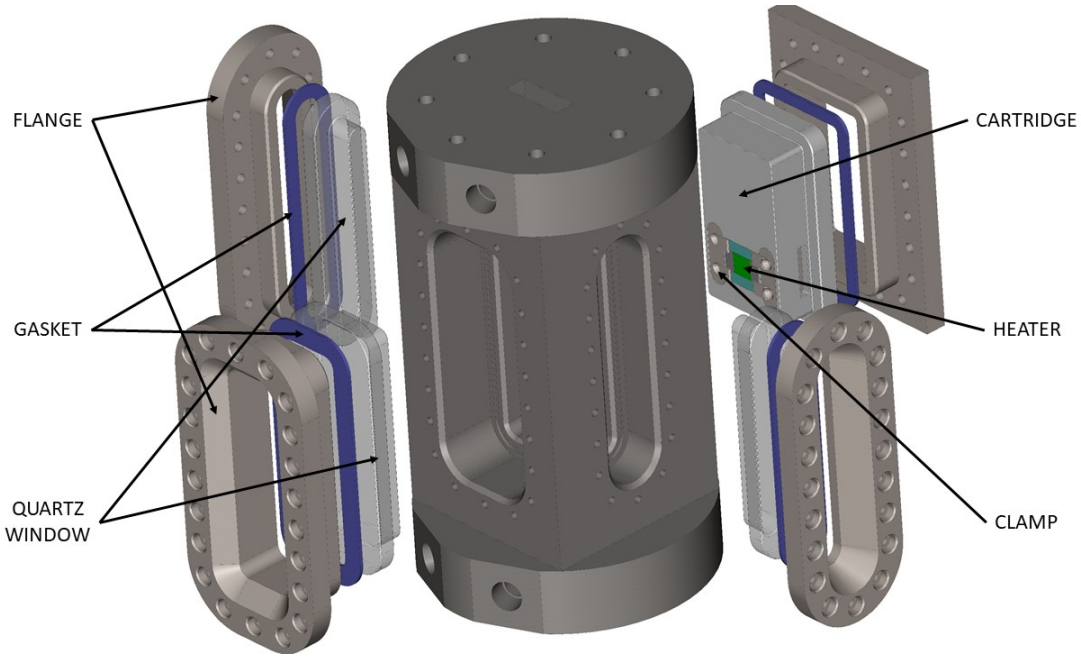

Figure 2-10: Exploded view of the test section assembly.

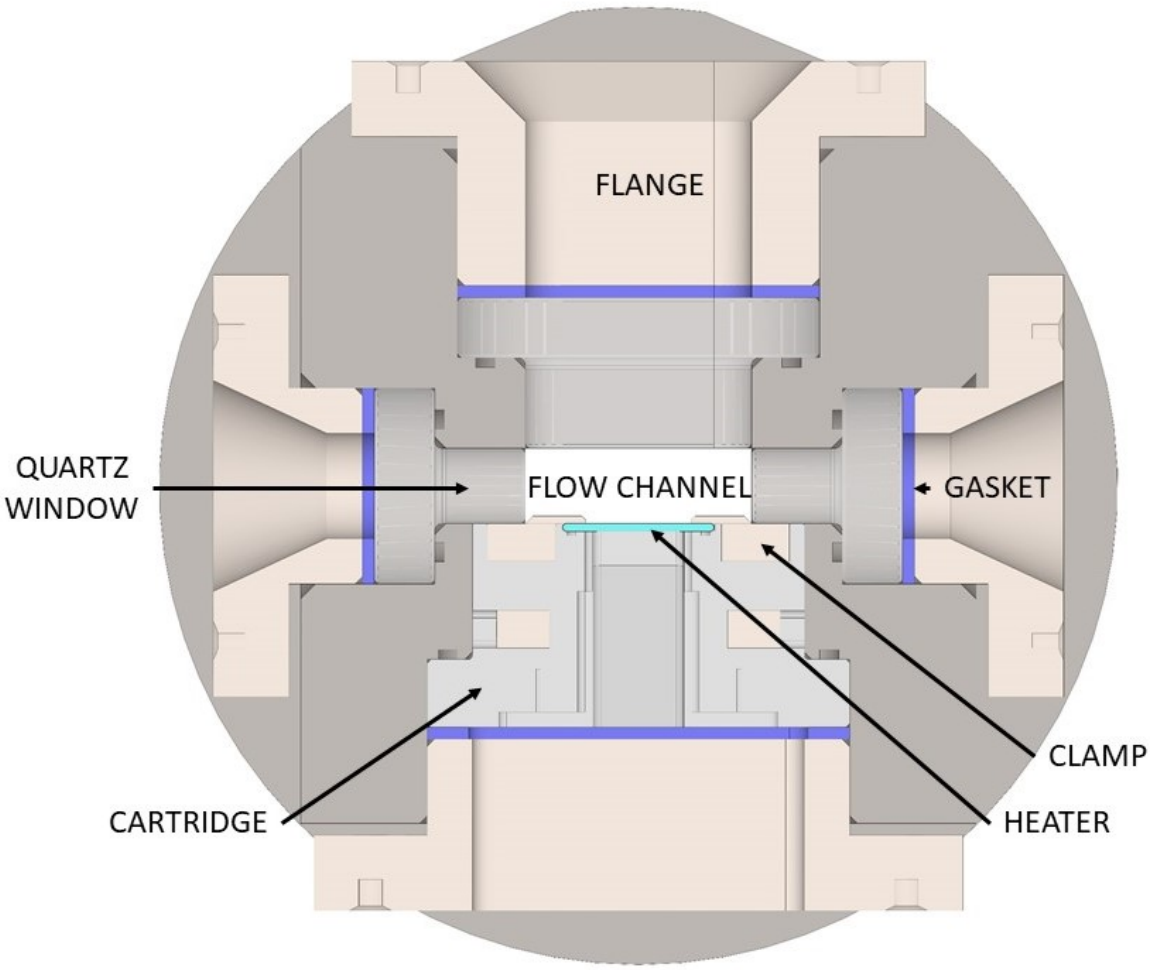

Figure 2-11: Cross-section view of the test section assembly.

2.3 Heater Cartridge

The heater cartridge serves three primary functions, mechanical support and positioning of the ITO heater, electrical access and isolation of the heater and providing an optical path to the heater for the camera diagnostics. Figure 2-13 provides an image of the exploded heater cartridge assembly. The cartridge must position the heater such that it sits flush with the channel wall and is in direct contact with the flow. The ITO serves as a Joule heater and requires an electrical connection to a DC power supply to generate the heat for boiling. Since the test section is made of 316 stainless steel, the heater must by isolated from the test section to prevent short-circuiting. Finally, the IR camera must have a direct line of sight to the heater, with minimal obstructions in the optical path. The HSV camera must also have line-of-sight to the heater surface as well as appropriate back-lighting for shadowography.

The mechanical support and electrical isolation require the cartridge to be made of a compatible material. Ceramic materials provide both mechanical strength and a lower electrical conductivity and are an ideal choice for the heater cartridge. Phillips used a Macor cartridge for an ITO heater [12], although epoxy was used to secure the heater in place. A ceramic material, similar to Macor, called Shapal was chosen for the heater cartridge. Shapal has a much higher yield strength of 300 MPa and a resistivity of $10^{15} \frac{\Omega}{cm}$ [42]. Further, Shapal can be easily machined using traditional machining techniques allowing for a wide variety of designs with minimal limitations. A calculation and stress analysis similar to the calculations outlined in Section 2.2 was done to ensure the Shapal was strong enough to withstand the stresses from the high pressure conditions. Results of the finite element stress analysis are shown in Figure 2-12.

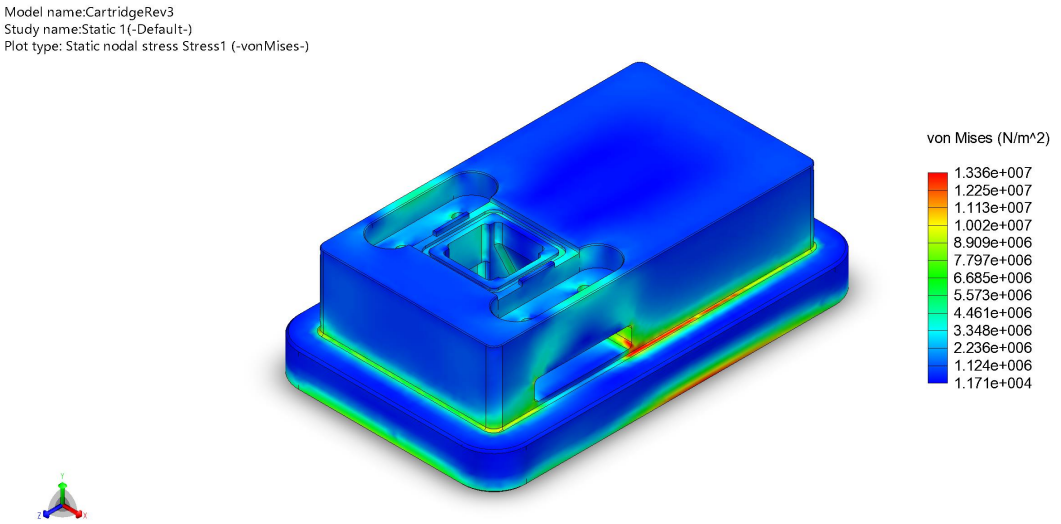

Figure 2-12: Results of finite-element stress analysis for Shapal heater cartridge.

The heater must be mounted on the cartridge such that is flush with the channel wall. A mechanical clamping mechanism was chosen for mounting the heater as it is more reliable and faster than an epoxy adhesive. The heater is placed on the front of the cartridge along with an o-ring to create a liquid seal and pressure barrier. To secure the heater, a clamp is placed on either side of the heater with arms that extend onto the heater pads. The clamps are made of 316 stainless steel to minimize the amount of corrosion that can occur with water. The clamps are then screwed down to depress the heater into the o-ring providing the necessary compression to ensure a good seal.

Behind the mounted heater is a through-hole extending to the rear-side of the cartridge. This hole provides the optical path required for both the IR camera and back-lighting needed for HSV shadowography. The vertical walls of the hole are angled outward so as to provide an additional visible angle for the burnout prevention system outlined in Section 2.6. Conductive aluminum tape is placed on the sides of the hole that connect the silver pads on the heater to the rear-side of the cartridge. This enables electrical connections to be made to the heater outside of the flow channel. This point is important as adjustments to the electrical connection can be made without the need to drain the loop and replace the cartridge.

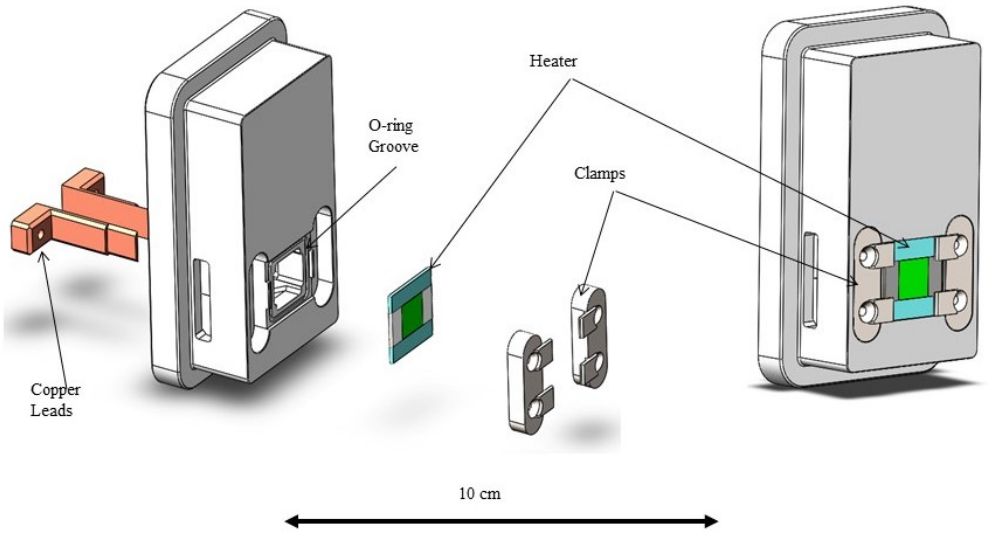

Figure 2-13: Exploded view of cartridge assembly (Left). View of assembled cartridge with ITO heater (Right).

2.4 ITO Heater

The ITO heater consists of three layers, see Figure 2-14. The substrate is made of optical grade sapphire. Sapphire is transparent in the visible wavelengths as well as the IR wavelengths with minimal emission above 5 μm [43]. Sapphire is mechanically robust enough to withstand the high-pressure environment [44] with a compressive strength of 2000 MPa and a tensile strength of 250-400 MPa depending upon the orientation of the crystal structure. Sapphire also has a high electrical resistivity of $10^{17}\Omega - cm$. On top of the sapphire is a 700 nm ITO thin-film. ITO is transparent in the visible wavelengths and opaque in the IR wavelengths [45]. This allows for back-lighting through the rear-side of the heater with a HSV camera imaging the top surface of the heater. In the IR, ITO will emit radiation based on the local temperature which can then be recorded through the IR transparent sapphire substrate using an IR camera. The ITO film is thin enough such that it has negligible thermal resistance and thermal capacity, as such, the temperature difference between the boiling surface and the rear-side of the ITO can be considered negligible [46]. ITO is also electrically conductive with a surface resistivity of approximately 2.5 $\frac{\Omega}{sq}$. An electrical DC current can be applied to generate the heat required for boiling using Joule heating. The third layer of the ITO heater consists of two electrically conductive silver pads. The silver pads are meant to facilitate the electrical connection to the ITO thin-film, reduce the contact resistance between the electrical leads and the ITO film, and define the active area of the ITO.

The sapphire substrate measures 20 mm x 20 mm x 1 mm with two filleted edges on either side. The filleted edges are used in the "wrap-around" heater design where both the ITO film and the silver pads wrap-around from the top surface of the heater to rear surface using the filleted edges to maintain a consistent connection. The wrap-around design is used so the electrical connection can occur on the back-side of the heater rather than attempting to make the electrical connections on the wetted-side of the heater. Both the ITO and the silver pads wrap-around to enhance the contact area between the two layers and minimize the amount of contact resistance.

Additional contact resistance increases the amount of power required to generate heat for boiling and also concentrates the heat generation in unwanted areas on the heater. Minimizing the contact resistance is of utmost importance in the heater design process.

The ITO film is 700 nm thin, 10 mm wide, runs the length of the top surface of the sapphire heater and wraps around to the rear side, extending 4 mm towards the center of the heater. The silver pads are also 10 mm wide and sit directly atop the ITO film. The pads extend 5 mm each towards the center on the top-side of the heater. On the rear-side the silver pads extend 4 mm towards the center, the same as the ITO. The shorter length of the silver pads leaves a 10 mm x 10 mm square area of ITO exposed on the top-side of the heater. This is the boiling surface and the location of the heat generation.

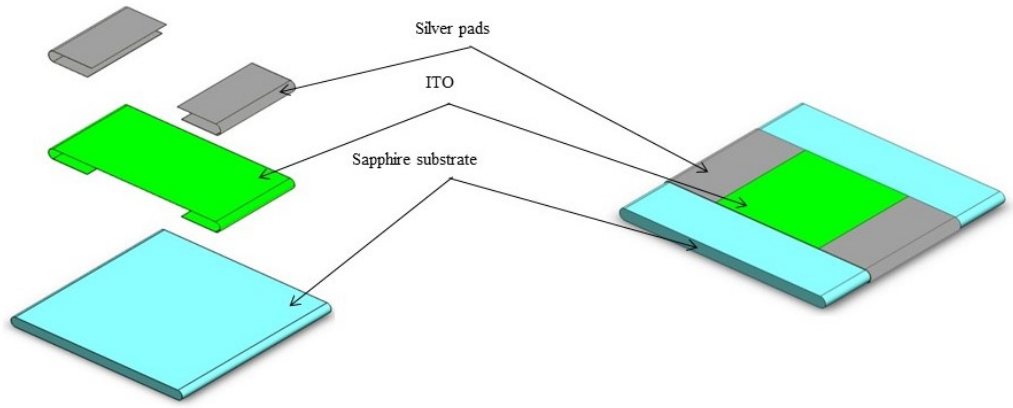

Figure 2-14: (Left) Exploded view of ITO heater. (Right) View of ITO heater

2.5 Infrared and High-Speed Video Cameras

The IR camera used for this study is an IR Cameras 806HS. The 806HS has a maximum window size of 640 x 512 pixels with a full frame acquisition rate of 475 frames per second [47]. The window can be downsized to increase frame rate. This study used an effective window size of 96 x 96 (actual window size of 640 x 96) with an acquisition rate 2500 frames per second. The integration time used was 0.1 ms. A

longer integration time could be used, however the IR camera would saturate quickly when CHF is reached. A shorter integration increases the range of temperatures the IR camera can measure while still allowing for a good signal-to-noise ratio. The 806HS is a mid-wave camera sensitive to IR wavelengths between 1 to 5.7 μm. A filter wheel is located in front of the sensor and a 3 to 5 μm band-pass filter was used during data collection. A 100mm IR lens was used at a working distance of approximately 0.6 meter. The achieved resolution is 115 microns/pixel.

The camera focal plane array (FPA) must operate below 80 K. The 806HS is cooled by liquid nitrogen from a dewar located behind the FPA. A full dewar will keep the camera cool for approximately four hours, however it is suggested the dewar be refilled every hour.

The camera is controlled using the WinIRC software to set the window size, integration time, frame rate, total number of frames to record and triggering mechanism [48]. The software is also capable of providing real-time analysis tools such as line/area profiles and averages which can be used for camera alignment. Finally, the software offers a non-uniformity correction (NUC) to account for a non-uniform response across the FPA.

The HSV camera used was a Phantom V12 designed by Vision Research [49, 50]. The V12 was operated at 20,000 frames per second with a 380 x 380 window size. The maximum integration time of 49 μs was used. A Nikon 200mm lens was used along with extension rings depending upon if both the top and side-views were images or just the top-view. Refer to Figure 2-18 for a schematic of the HSV optical setup. The camera was controlled using the Phantom software. Window size, integration time, number of frames to record, and triggering were set using the software.

In experiments where both IR and HSV cameras were used, the two cameras were synchronized using an external function generator. The function generator outputs a TTL burst signal set to 20,000 Hz for 2.5 seconds. Data is collected on the IR and HSV cameras for 2 seconds, corresponding to 40,000 frames of HSV data and 5000 frames of IR data. The function generator is triggered using an external trigger. When triggered the HSV follows the TTL signal and triggers every frame off the TTL

signal. The IR camera triggers off of the first input and then follows an internal clock for subsequent frames.

2.6 Burnout Prevention System

Capturing the departure from nucleate boiling is part of the scope of work for this thesis. When DNB occurs a vapor film is created on the boiling which drastically lowers the heat transfer coefficient between the ITO and the water. This results in a large increase in surface temperature. Such a large change in temperature in a very short time causes large thermal stresses on the heater and can lead to failure. Failure of the heater, typically in the form of a crack in the sapphire, drastically increases the time required to collect data and increases the number of heaters necessary to complete the test matrix. Preventing catastrophic failure of the heater is beneficial for quite a few reasons. It is beneficial to use the same heater for as many tests as possible, as it limits the discrepancies between tests since each heater can have different surface qualities such as contact angle, nucleation site density, and roughness. Additionally, if the heater were to fracture at high-pressure, localized flashing will occur which can be a safety concern for operators within the room. Finally, the sapphire substrate is no longer viable and cannot be reused. This leads to increased costs.

To prevent catastrophic failure of the heater a "Burnout Prevention System" (BPS) was implemented. This system consists of a small IR photodetector and a lens focused on the ITO heater. Figure 2-15 shows a schematic of the BPS setup. The system is connected to a switch between the power supply and the ITO heater. The switch remains closed during normal operation allowing the power supply to deliver a DC current to the ITO heater. The IR photodetector outputs an analog signal proportional to the change in the radiometric signal it measures. If the photodetector measures a constant signal (i.e. no change in ITO surface temperature) then it will not output any signal. However, when the temperature begins to change, the IR photodetector will output a signal to the switch. The switch will activate, opening the connection between the power supply and heater, when a threshold voltage is output

from the IR photodetector. The threshold can be tuned using a potentiometer. In this case the BPS is tuned to cut the power when it detects the transient temperature increase due to DNB.

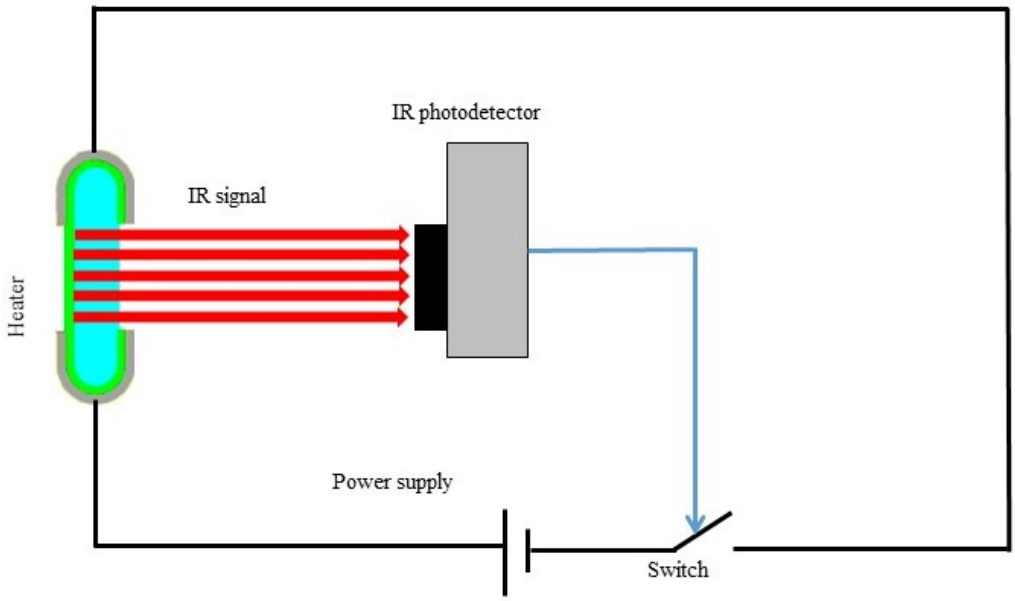

Figure 2-15: Schematic of BPS with IR Photodetector imaging ITO heater. The IR photodetector is connected to a switch between the power supply and silver pads. Schematic courtesy of Artyom Kossolapov.

2.7 Polarity Switching System

When a voltage is applied to the ITO heater an electro-chemical reaction can occur with the water. It is believed that this reaction is a migration of the Indium within the ITO. Over the course of an experiment, a deposit begins to form on the surface the heater. An example of this deposit is shown in Figure 2-16a. This deposit can change the surface properties of the ITO. A clear non-uniformity in the heat generation was visible as the deposit began to form on the surface. This was likely due to a localized increase in the electrical resistance within the ITO film. The time frame of this reaction was on the order of hours when voltages up to 30 V are applied to the ITO film at atmospheric pressure and saturation temperature. At high pressure (10 bar) and temperature (180 C) the reaction occurred much quicker, on the order of 5 to 10

seconds.

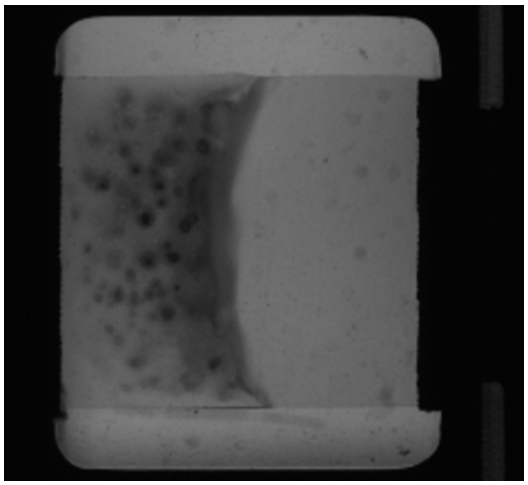

(a) HSV picture of deposit forming as a result of an electro-chemical reaction between ITO and water.

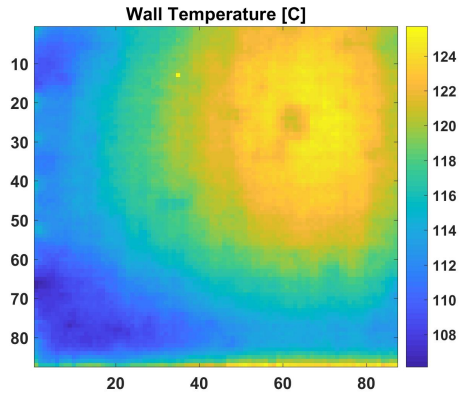

(b) Temperature distribution non-uniformity due to electro-chemical reaction of ITO.

To extend the lifetime of the ITO heaters, it was necessary to develop a method of mitigating this electro-chemical reaction. Noting the build-up time for the reaction to occur and that the reaction is electrically driven, the ITO heater was tested using AC power. No reaction was observed with the AC power because of the rapidly alternating polarity of the system. Unfortunately, AC power is not optimal for supplying power to the heater as the heat flux would not be constant. Instead, a polarity switching system (PSS) was implemented to switch the polarity of the heater pads while using DC power.

The PSS consists of four SPST solid-state relays controlled by a function generator. The relays are placed between the DC power supply and the ITO heater. The relays are connected in pairs such that one pair is connected to the negative terminal of the power supply and the other pair is connected to the positive terminal of the power supply. Conversely, one of each pair is connected to either side of the heater such that each side of the heater has a connection to both the positive and negative terminals of the power supply. The opening and closing of the relays is controlled by the function generator. The function generator outputs a square-wave to control the input of the relays, which triggers the opening and closing of each relay. A positive voltage across the input of the relay will close the switch between the power supply

and the heater and enable power to the heater. The key is the pairing of the relays such that only one set of relays is open a given moment; one relay connected to the negative terminal of the power supply and one side of the heater, and another relay connected to the positive terminal of the power supply and the opposite side of the heater. As these relays open and close in pairs, by the alternating square-wave from the function generator, the "polarity" of each of the pads of the heater will alternate with them.

The function generator outputs a 5 Hz square-wave signal which swaps the polarity of the pads ten times per second. With this system in place, no electro-chemical reaction was observed for experimental times up to ten hours with voltages up to 60 V being applied. A schematic of the PSS is shown in Figure 2-17. The effect of the polarity switching system on a steady-state system can be seen in Figure 2-20. Note the single counts measurement every 250 frames appears consistently lower than the rest. This frame is slightly lower than the rest of the frames as this is the frame where the polarity switching system is triggered, and the power is briefly interrupted. This clearly has a very minimal effect on the test as the heater returns to normal temperature the next immediate frame.

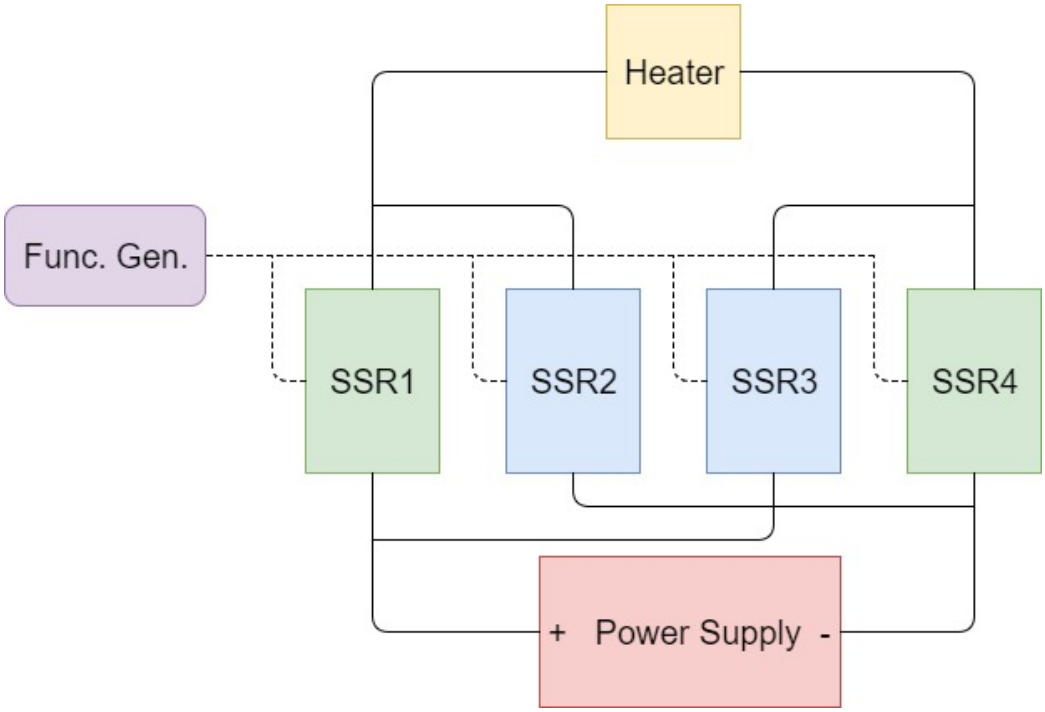

Figure 2-17: Schematic of the polarity switching system. The relays open and close in pairs as designated by their color coding.

2.8 Experimental Methods

This section outlines the methods used for collecting the flow boiling data. Standard operating procedures for operating the loop, setting up the equipment and using the post-processing scripts are given in the appendices.

To begin the experiment the first step is to mount and align the IR and HSV cameras. The schematic for orienting the cameras is given in Figure 2-18. The IR camera must be aligned with the ITO heater such that the measured counts distribution is as flat as possible. This can be checked using the linear profile tool within the WinIRC program [48]. If there is a slope in the counts then either the camera or beam splitter must be re-aligned to flatten the distribution. Similar to the IR camera, the HSV camera and optical mirrors must be aligned such that the backlight provides a uniform image of the heater surface.

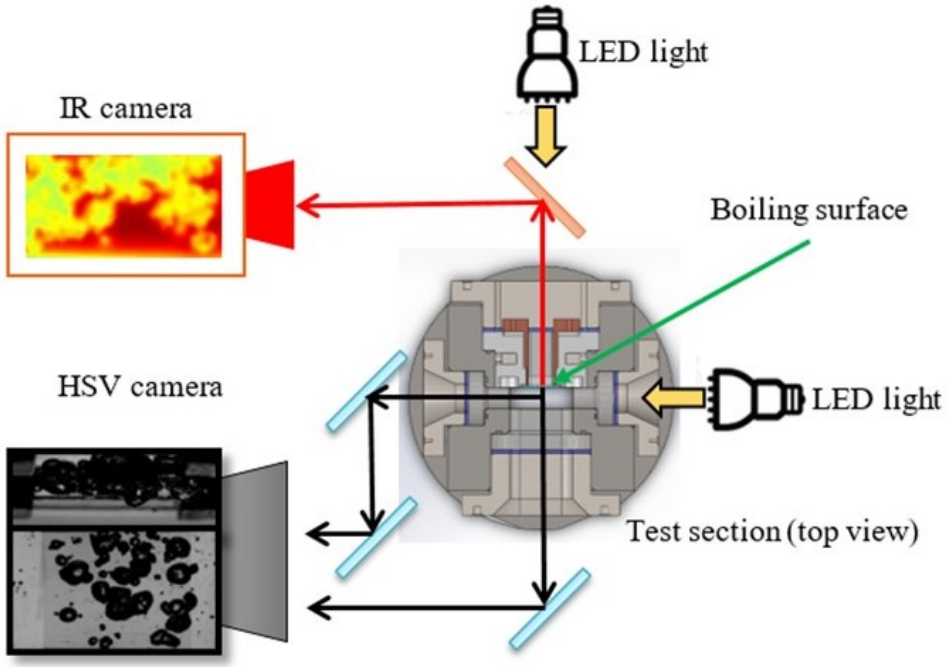

Figure 2-18: Picture of the orientation of the HSV and IR cameras with respect to the test section and heater. Also shown are the LED backlight and beam splitter used.

Once the cameras are in position the flow loop can be filled using the filling procedure. There are two methods for degassing the loop, either using the flow

membrane or degassing at saturation conditions with a high-point vent. After filling the loop, the pump can be turned on and degassing using the membrane can begin by following the degassing SOP. This step usually takes about two hours. Following degassing, the loop can be heated up using the cable heaters set to full power. The heaters provide enough power to heat the loop from room temperature to 90 C in about one hour. A calibration curve must be obtained using the IR camera as the loop is heating up. This consists of collecting 500 frames of video every five degrees. This provides a method for calibrating the optical system and determining the quantum efficiency of the setup, which is later used in the radiation-conduction model. When the loop reaches saturation a second round of degassing can occur using the high-point vent. Here, the pump is turned off and the walls are allowed to boil where the cable heaters are wrapped around the tubes. The vapor and non-condensables rise to the high-point of the system where they can be vented periodically. This method takes about two hours to complete.

The data collection process uses one of two methods. To collect HSV and IR data simultaneously the two cameras must be synchronized. Since the HSV has a limited on-board frame buffer there is a limit of 40,000 frames that can be collected. At a frame rate of 20,000 fps this equates to two seconds of data. Once collected, the HSV camera must off-load its buffer onto the computer which takes approximately 5 minutes. This limits data collection to a single heat flux step at a time. The steps to collecting data is then to manually input the desired voltage on the power supply, pre-trigger the cameras and high-speed data acquisition system (HSDAS), and trigger the system. This method has the benefit of collecting both HSV and IR data but takes significantly longer due to the time required to off-load the HSV data.

The second method for collecting data is much quicker, however no HSV data is collected. The IR camera directly writes to the computer RAID-array on-the-fly. The theoretical maximum number of frames that can be recorded by the IR camera is simply limited by the amount of available space on the computer drive. Instead of collecting one heat flux video at a time, a stepped power curve can be used along with an extended IR camera recording time to collect data on the entire boiling curve

in one go. The stepped boiling curve consists of 30 4-second steps. Each step consists of a one second ramp from the previous power to the target power and a three second steady-state at the target power. The first second at the target power is used to allow the system to equilibrate. The final two seconds are used to collected IR video. This method has the benefit of collecting IR data much quicker, enabling a complete nucleate boiling curve to be collected in two minutes.

The stepped power was generated using a combination of two Chroma 62050P-100-100 programmable DC power supplies and a RIGOL DG1022U function generator. The Chroma power supplies have a signal following function where the power supply will output 10x the reference signal [51]. The function generator can be programmed to provide the reference signal with the voltages matching the power inputs desired using a provided Excel spreadsheet program [52].

A sample stepped boiling curve is shown in Figure 2-19. This curve is the result of the measurements from the HSDAS, which records the applied current and voltage at 2500 samples per second. The average power for each step is given along with the instantaneous heat flux measurement. The average is only taken for the final two seconds of the step and does not account for the ramp or the one second before data is collected. The cut-off at the end occurs once CHF has been reached. The power input and measured camera average counts from a complete step is plotted in Figure 2-20. The output counts follows the heat input as expected. The counts level off when the ramp from the heat input stops, after one second, and reaches the steady-state section of the step. The counts are essentially flat for the remaining three seconds of the step, re-affirming a steady-state condition has been reached.

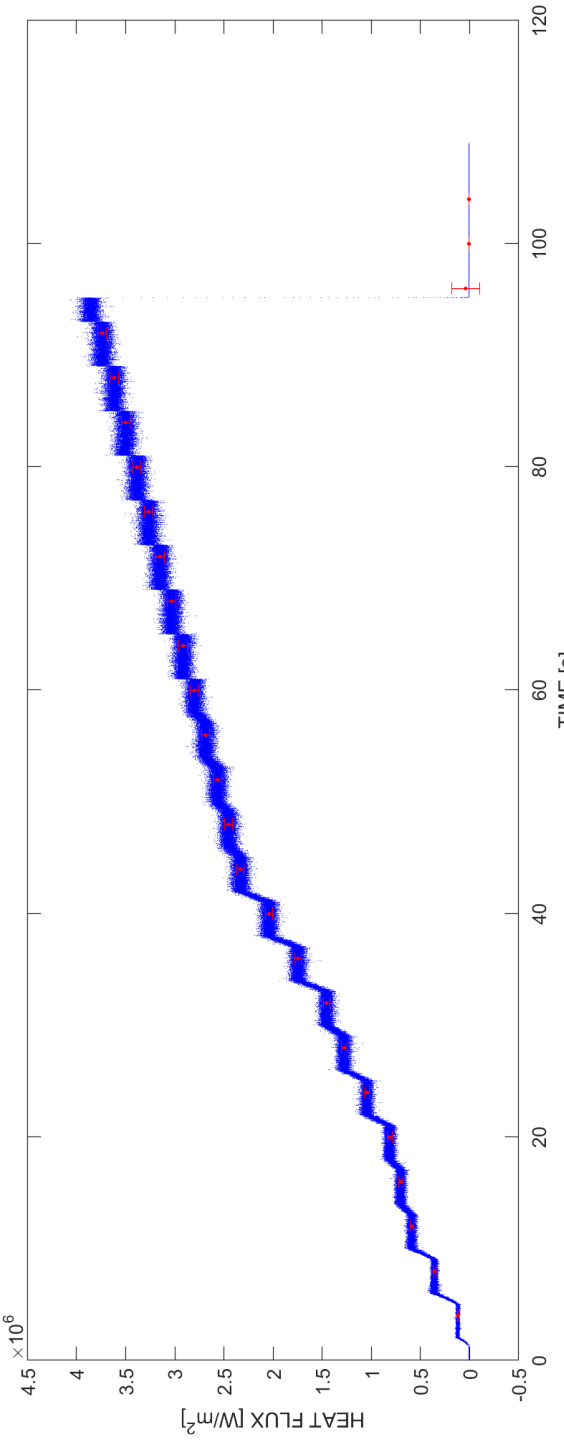

Figure 2-19: Example of stepped power curve for 1 bar, 10 K subcooling, 1000 $\frac{kg}{m^2 s}$ flow rate.

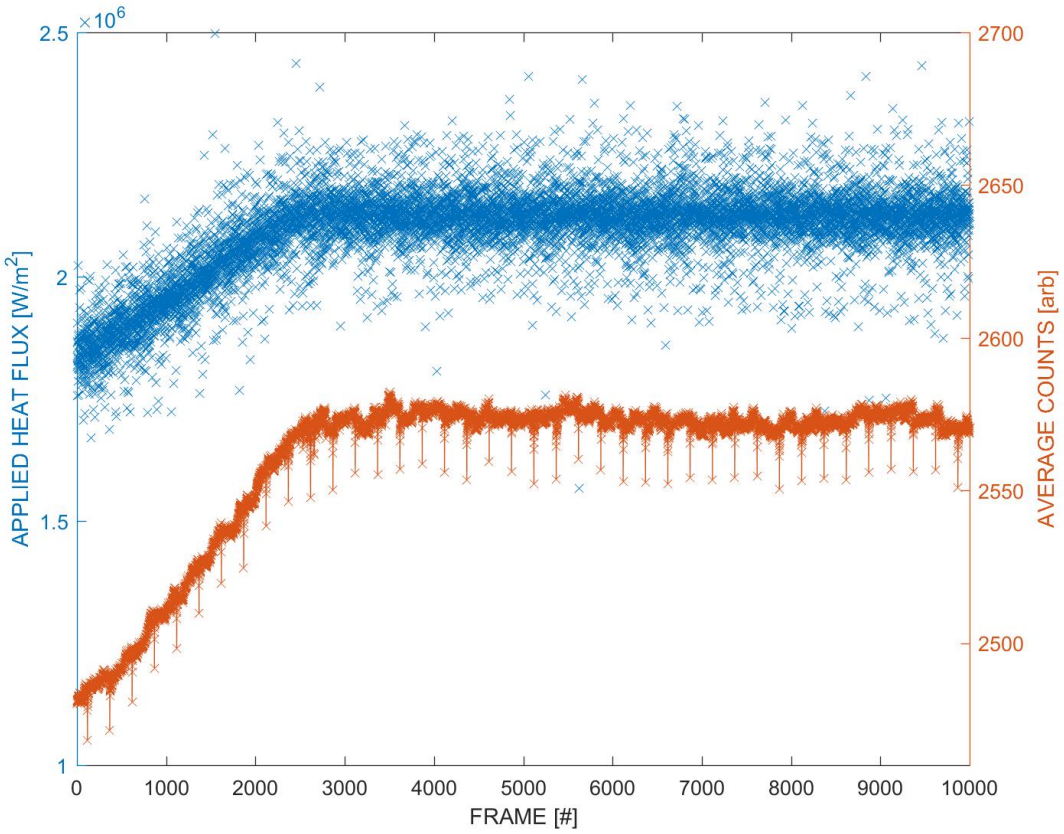

Figure 2-20: Measured heat flux (via current and voltage measurement) and measured counts from IR camera. The counts reach steady-state approximately the same time the power input reaches a plateau. Also note the frames where the PSS is triggered and there is no power input resulting a briefly diminished value of counts.

Chapter 3

Post-Processing, Results and Analysis

3.1 Test Matrix

The scope of the test matrix is shown in Figure 3-1. The flow conditions considered include mass fluxes of 1000, 1500 and 2000 $\frac{kg}{m^2 s}$, subcoolings of 5, 10 and 20K, and 1, 2, 5 and 10 bar absolute pressure. The flow rate is limited by the maximum power of the circulation pump and the pressure is limited by the pressure and temperature ratings of the flow loop components. Note that, in Figure 3-1, each color corresponds to a different heater.

For each flow regime, 30 heat fluxes were chosen to collect data, starting in the single-phase regime and continuing through the nucleate boiling regime of the boiling curve, up to CHF. The first five heat fluxes for each boiling curve were chosen such that the heat transfer remained in the single-phase forced convection regime to estimate the single-phase heat transfer coefficient. The remaining heat fluxes were spaced at no more than 500 $\frac{kW}{m^2}$ apart, with the final five points generally spaced only 100 $\frac{kW}{m^2}$ apart. This approach provides a good resolution of points throughout the nucleate boiling curve, while providing extra data points near CHF.

	1 Bar		
	Mass Flux		
Subcooling (K)	1000	1500	2000
5			
10			
20			
	2 Bar		
	Mass Flux		
Subcooling (K)	1000	1500	2000
5			
10			
20			
	5 Bar		
	Mass Flux		
Subcooling (K)	1000	1500	2000
5			
10			
20			
	10 Bar		
	Mass Flux		
Subcooling (K)	1000	1500	2000
5			
10			
20			

Figure 3-1: Test matrix for pressurized subcooled flow boiling experiment. The color associated with each regime indicates which heater was used to conduct the test.

3.2 Post-Processing of IR Data and Boiling Curve Results

The raw data collected by the IR camera consists of over 300,000 frames of data for each boiling curve. Each frame is 640 x 96 pixels, where each pixel is a 13-bit number, called "counts". The counts are representative of the intensity of the IR light measured by the camera at that pixel. The raw data contains very little information on the fundamental boiling parameters, and temperature and heat flux distributions. The majority of the data reported in this work comes from post-processed data using mechanistic calibration techniques and various image processing algorithms to extract the desired boiling information.

3.2.1 IR Calibration with the Radiation-Conduction Model

To process the data, the first step is to separate the frames into the respective heat flux steps as outlined in Section 2.8. Once the steady-state steps have been extracted, the data is fed through a radiation-conduction calibration model to extract the complete time-resolved surface temperature and heat flux distributions. This technique was developed by Bucci et al. [17] and is briefly summarized here.

Previous methods of calibrating the IR camera output have typically relied upon an empirical curves of camera counts versus a measured surface temperature using thermocouple attached to the boiling surface. While simple, this method does not account for radiative emissions from the substrate nor reflections from the ambient environment. As such, these types of calibrations can be inaccurate, in particular during fast transient heat transfer.

The main benefits of using a coupled radiation-conduction calibration technique are the enhanced accuracy of the mechanistic model and the capability of determining the heat flux distribution on the boiling surface. The conduction model yields the complete temperature distribution within the substrate. Given the z-axis temperature profile, that is the temperature profile from the surface to the rear of the heater, the

heat flux entering the substrate at the boiling surface can be determine using Fourier's Law:

$$q''_{sapphire} = -k\frac{dT}{dz} \approx -k\frac{\Delta T}{\Delta z} \tag{3.1}$$

Where k is the thermal conductivity of the substrate. The heat flux to water can then be determined as:

$$q''_{water} = \frac{P}{A} - q''_{sapphire} \tag{3.2}$$

Where P is the electric power applied to the heater, and A is area of the heater over which the power is distributed.

For the work presented here, measuring the heat flux using this post-processing technique is a crucial step as it enables the direct measurement of all of the fundamental boiling quantities previously mentioned as well as the heat flux partitioning. Once the heat flux distribution has been quantified using the radiation-conduction model, the heat flux partitioning can be determined by using image analysis tools to detect the presence of bubbles, recent departures of bubbles, or single-phase heat transfer.

The radiation model requires two primary calculations, the first is a calculation of the IR light emission from the ITO, sapphire and background, respectively, and the second is a calculation of how much signal from each source reaches the IR camera. Note that all of the equations and quantities given here are spectrally dependent. Most of the materials used in this work have varying spectral behavior. For instance, ITO is almost completely transparent in the visible wavelengths, while also completely opaque in the IR. Accurately measuring and calculating the optical properties across the entire spectrum used by the IR camera is very important in the execution of the radiation model. Simply using spectrally averaged properties simplifies the problem, but introduces another source of error that can be quite significant with some materials [17].

The Planck equation along with the material specific emissivity is used to deter-

mine the intensity of light (or photon flux) emitted by a specific material.

$$N_{p,\lambda}(T,\lambda) = \frac{2\pi c}{\lambda^4(e^{\frac{c_2}{\lambda T}} - 1)} \tag{3.3}$$

Here $N_{p,\lambda}$ is the spectral photon flux, c is the speed of light, T is the temperature at the location of interest, λ is the wavelength and c_2 is a constant with a value of $1.439 \cdot 10^{-2} mK$. Integrating this equation over the wavelength of interest yields the total photon flux emission.

The next calculation requires a model of the optical system to calculate the radiometric propagation of light through the system to determine how much IR light recorded by the IR camera originates from the ITO film (the desired signal) and how much is undesirable signal that is emitted by the sapphire or surrounding environment. The model consists of two parts, the radiometric propagation of light through the heater, which is a participating media problem due to the sapphire substrate, and the quantum efficiency of the cold optics such as the spectral beam splitter and the IR camera lens. The solution to the participating media problem for ITO is the apparent transmissivity and reflectivity, shown in Equations 3.4 and 3.5, respectively. These equations accurately track the emission from ITO to establish what fraction of the emitted light is actually collected by the IR camera. They are derived by tracking the propagation of the ITO signal, from its emission, and tracking the absorption in sapphire, and the transmissions and reflections as it becomes incident on the various interfaces within the heater.

$$\tau_{\lambda,app} = \frac{(1-\rho_{\lambda,hs})\tau_{lambda,s}(1-\rho_{\lambda,sa})}{1-\rho_{\lambda,hs}\rho_{\lambda,sa}\tau_{\lambda,s}^2} \tag{3.4}$$

$$\rho_{\lambda,app} = \rho_{\lambda,sa} + \frac{\rho_{\lambda,hs}\tau_{\lambda,s}^2(1-\rho_{\lambda,sa})^2}{1-\rho_{\lambda,hs}\rho_{\lambda,sa}\tau_{\lambda,s}^2} \tag{3.5}$$

Here, $\rho_{\lambda,hs}$ is the measurable ITO-sapphire interface spectral reflectivity, $\rho_{\lambda,sa}$ is the measurable sapphire-air interface spectral reflectivity, $\tau_{\lambda,s}$ is the measurable transmissivity through sapphire. The apparent emissivity for ITO can be calculated from the Kirkoff equation, see Equation 1.10, and Equations 3.4 and 3.5.

When calculating the total emission in a participating media problem, the emission at each point in the z-axis (perpendicular to the surface face) of the participating media must be calculated, and then integrated over the thickness of the substrate. This is referred to as the apparent emissivity. Importantly, this requires knowledge of the axial temperature distribution within the substrate to evaluate Equation 3.3 at each axial point. This is a key feature of the radiation-conduction algorithm as it is one of the two linkages that couples the radiation model to the conduction model.

Figures 3-2 and 3-3, depict schematics of the algorithm used to calculate the apparent forward and backward emissivity of the sapphire (the participating media) as part of the ITO heater. Since light can be emitted either towards the ITO or away from the ITO, an analysis must be done to account for the propagation of each to determine the total amount of light exiting the heater that originates from the sapphire. The subsequent reflections, transmissions and absorptions are accounted for, yielding the apparent emissivity of the sapphire.

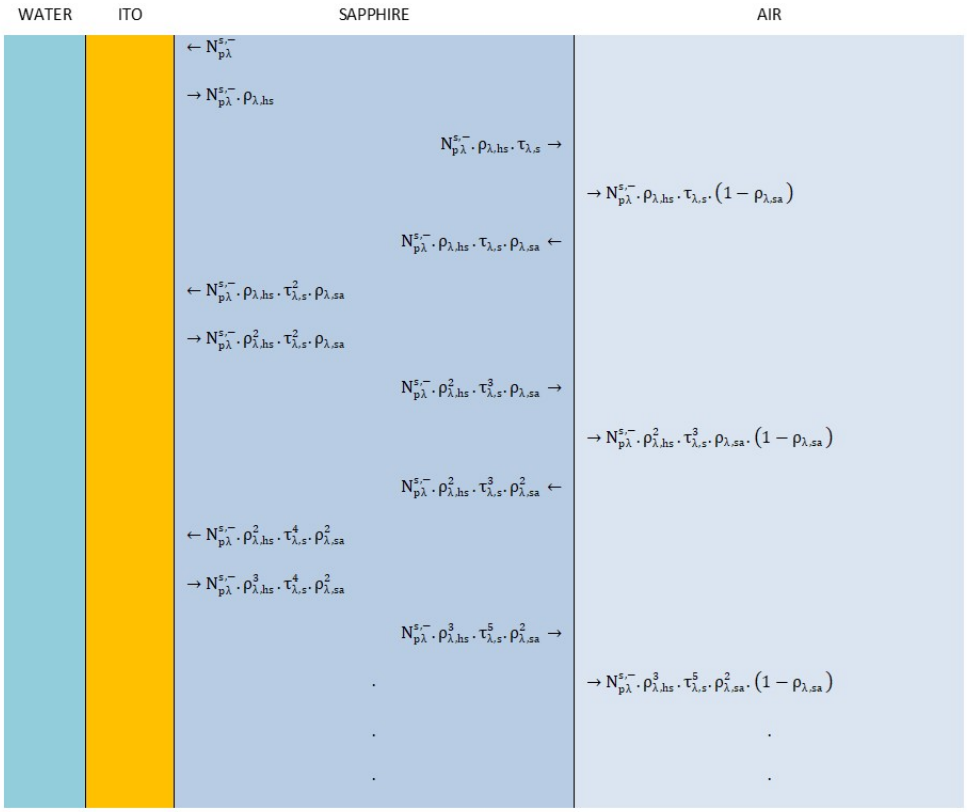

Figure 3-2: Multiple absorption and reflection determining the apparent backward emissivity $\epsilon^{-}_{\lambda,app}$. Figure adapted from [17].

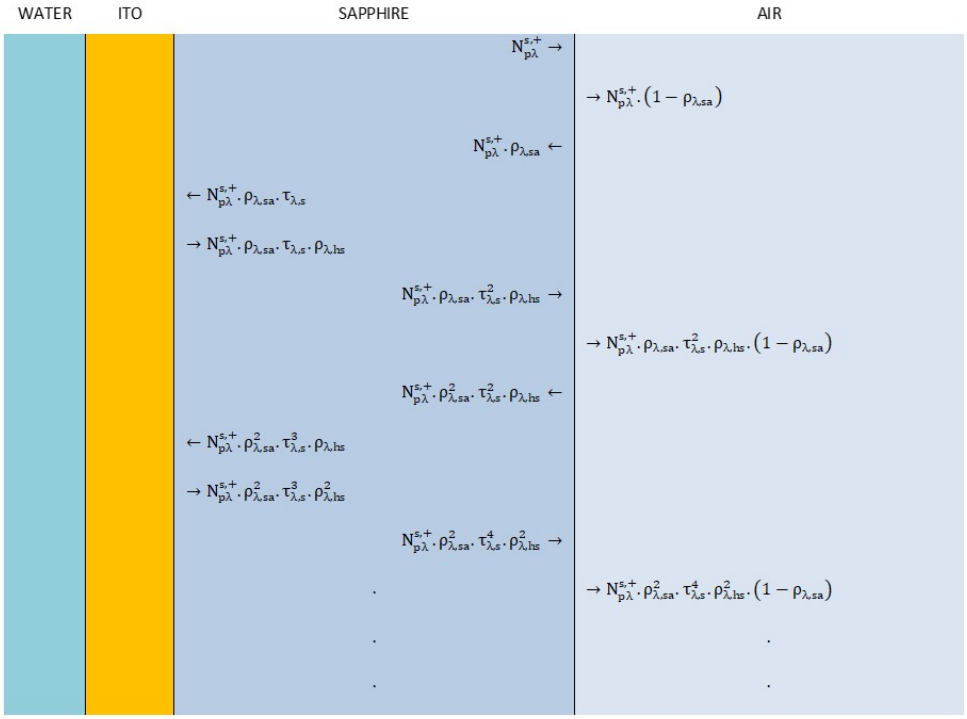

Figure 3-3: Multiple absorption and reflection determining the apparent backward emissivity $\epsilon_{\lambda,app}^{+}$. Figure adapted from [17].

The total light leaving the heater surface is calculated by adding the light from the ITO, the light from the sapphire and the light from the surrounding environment.

$$Np_\lambda = Np_{\lambda,T_h}\tau_{\lambda,app} + Np_{\lambda,T_a}\rho_{\lambda,app} + Np^{s,+}_{\lambda,T(z)}\epsilon^{+}_{\lambda,app} + Np^{s,-}_{\lambda,T(z)}\epsilon^{-}_{\lambda,app} \tag{3.6}$$

After integrating over the IR camera's specturm to calculate the total IR light leaving the heater, the amount of signal actually recorded by the IR camera is then calculated using the lens focal number and optical setup transmission efficiency.

$$N_{p,camera} = N_p \frac{\tau_{os}}{4n_f^2} \tag{3.7}$$

N_p is the number of photons exiting the rear-side of the heater, $N_{p,camera}$ is the number of photon received by the camera, τ_{os} is the aggregate transmission of the optics, and n_f is the lens focal number.

The last remaining step is to correlate the photons received by the IR camera, to the counts output of the camera.

$$N_{p,camera} = \frac{R - (nc_{ew} + \dot{n}c_{dc} \cdot t_{int})}{t_{int}} \cdot \frac{W_e}{(nc_{fw} - nc_{ew})} \cdot \frac{1}{QE \cdot A_{pixel}} \tag{3.8}$$

Here R is the counts, nc_{fw} and nc_{ew} are the counts values of the full and empty wells, respectively, nc_{dc} is the number of counts from the dark current, t_{int} is the integration time of the camera, W_e is the electron well size, QE is the quantum efficiency of the camera sensor and A_{pixel} is the size of a pixel on the sensor. Most of these values are available from manufacturer specifications. The first term is a correction of the counts to account for the dark current, electrons excited from the ground state due to thermal energy, and account for the baseline electrons excited in the well. The next term converts the counts to photons by scaling the well size with the range of counts possible. The final term accounts for inefficiencies in the camera and normalizes the area.

To summarize, given the axial temperature distribution of the substrate, the radiation model compares the measured counts from the camera with the expected counts from the ITO-sapphire substrate. If there is a discrepancy between the mea-

sured counts and the calculated counts, the surface temperature is updated and the conduction model is run again.

The conduction model used in this work is a 3-D implicit conduction model with a mesh size corresponding to the pixel size and array of the IR camera (86 x 86 at 115 μm/pixel) and a time step corresponding to the integration time of the IR camera. To reduce computational cost, the mesh outside of the region of interest (the active ITO area) has a lower refinement. The mesh is shown in Figure 3-4. The boundary conditions used were adiabatic on the north, south, east and west boundaries, adiabatic on the rear-side of the heater, an imposed temperature for the active area on top of the ITO heater, and an imposed single-phase heat transfer coefficient for the non-heated areas of the top surface. It is possible the adiabatic boundary conditions on the side could lead to an over-prediciton of the surface convection heat transfer in the single-phase regime for substrates with a high thermal conductivity.

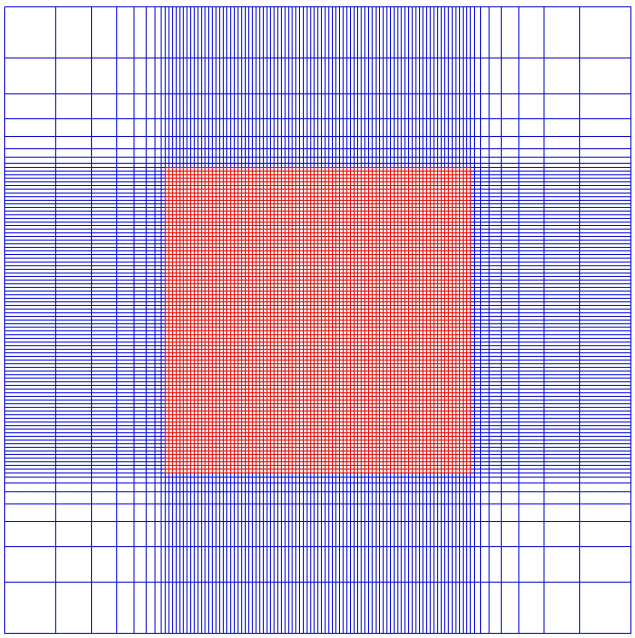

Figure 3-4: Top view of the discretized domain (x-y mesh). Figure adapted from [17].

The output of the conduction model is a 3-D temperature distribution within the

sapphire substrate. The temperature distribution calculated here is then fed into the radiation model to calculate the surface temperature of the ITO. Iterating between the models until a solution is converged upon yields the ITO surface temperature distribution as well as the temperature distribution throughout the rest of the heater. This has the added benefit of the ability to calculate the surface heat flux distribution using Fourier's law, Equation 3.1. Figure 3-5 shows the flow chart of the iterative sequence between the radiation and conduction models.

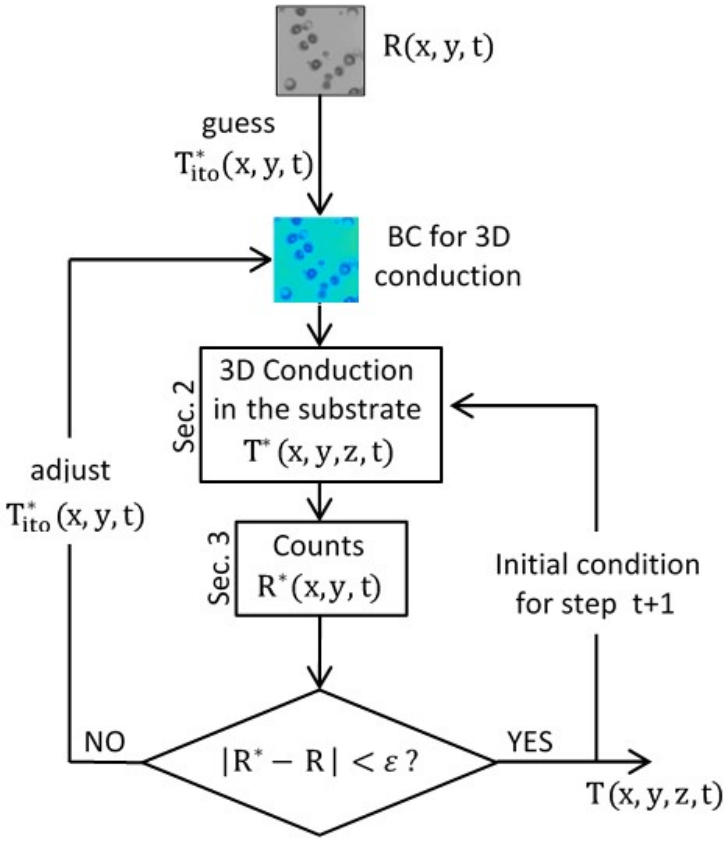

Figure 3-5: Flow chart of the coupled conduction-radiation model. A typical value of ϵ is 10^{-3} Figure adapted from [17].

The output of the coupled radiation-conduction model are the 2-D time-resolved surface temperature and heat flux distributions, shown in Figure 3-6. The temperature and heat flux distributions are the keystones to the remaining post-processing analyses. The nucleation site density, bubble frequency, growth time, wait time and

heat flux partitioning all depend upon the temperature and heat flux distributions as an input.

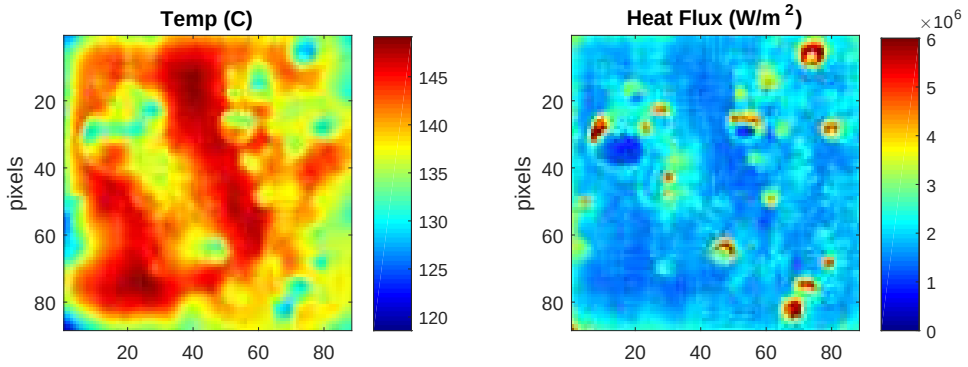

Figure 3-6: Sample output of the coupled radiation-conduction model. On the left is the 2-D surface temperature distribution, on the right is the 2-D surface heat flux distribution.

3.2.2 Boiling Curves

Boiling curves are generated using the temperature data as well as the measured voltage and current data from the DC power supply. The average temperature is measured by taking the time and space average temperature from the IR data.

$$T_{avg} = \frac{\sum_{x,y,t} T(x,y,t)}{N_{pixels} \cdot N_{frames}} \tag{3.9}$$

The average heat flux generated by the ITO is calculated using the time averaged power from the voltage and current data, and the active heater area.

$$q''_{heater} = \frac{1}{A_{heater}} \cdot \frac{\sum_{i=1}^{N_{DAS}} V_i \cdot I_i}{N_{DAS}} \tag{3.10}$$

The heat flux to water is calculated by subtracting the heat conducted into the sapphire using Equation 3.2.

Sample boiling curves are shown in Figures 3-7, 3-8 and 3-9, while the remaining boiling curves are given in Appendix A.

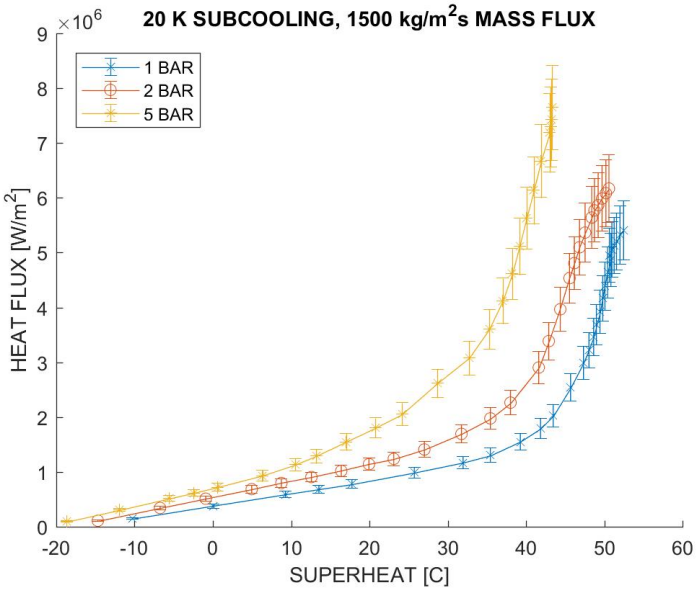

Figure 3-7: Boiling curves for 20 K subcooling and 1500 $\frac{kg}{m^2 s}$ mass flux with varying pressure at 1, 2 and 5 bar. The 1, 2 and 5 bar tests shown here were conducted on the "Yellow", "Green" and "Blue" heaters, respectively. See Figure 3-1.

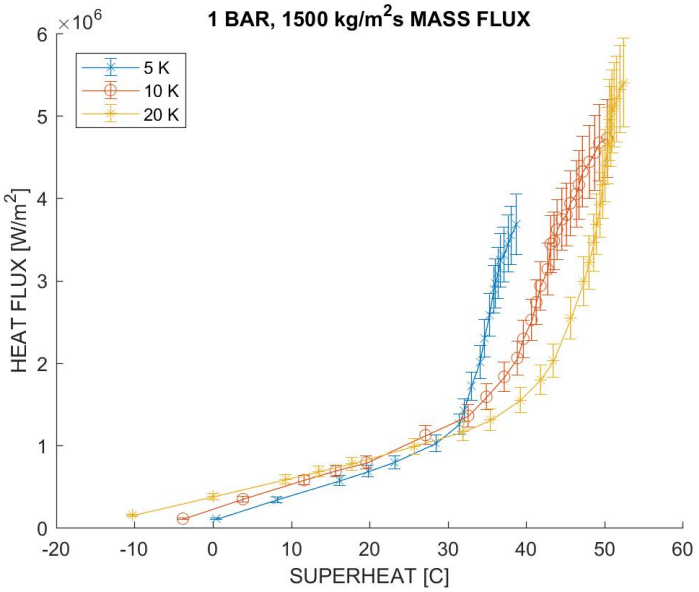

Figure 3-8: Boiling curves for 1 bar pressure and 1500 $\frac{kg}{m^2 s}$ with varying subcooling at 5, 10 and 20 K below T_{sat}. The 5, 10 and 20 K subcooling tests shown here were conducted on the "Red", "Green", and "Yellow" heaters, respectively. See Figure 3-1.

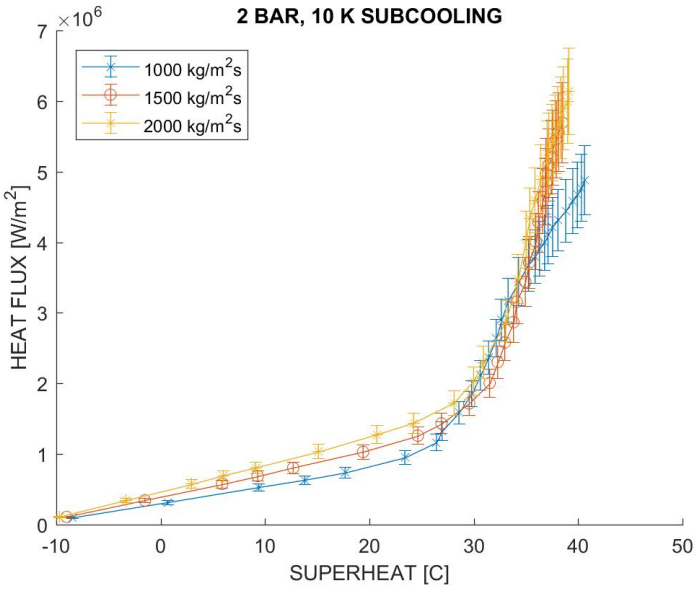

Figure 3-9: Boiling curves for 2 bar pressure and 10 K subcooling with varying mass flux at 1000, 1500 and 2000 $\frac{kg}{m^2 s}$. All tests shown here were conducted on the "Blue" heater. See Figure 3-1.

The boiling curve, as discussed in Section 1.4.2, provides an overview of the surface average heat transfer. In this work, a specific heat flux is applied and the resulting temperature is measured using the IR camera. As the applied heat flux is increased, the surface temperature also increases. The relation between the applied heat flux and the wall superheat is given by the heat transfer coefficient, which in single-phase forced convection is the slope of the boiling curve.

$$q'' = h \cdot (T_{wall} - T_{bulk}) \tag{3.11}$$

Initially, the boiling curve has a constant slope which is proportional to the single-phase heat transfer coefficient. This is consistent with the single-phase forced convection heat transfer regime previously described. Once the boiling surface has reached the requisite superheat to initiate nucleation, e.g. as governed by the Young-Laplace equation, see Equation 1.1, the slope of the boiling curve will increase as a result of the increased heat transfer from nucleate boiling. Consequently, the point at which the boiling curve changes slope is considered the point of the onset of nucleate boiling (ONB) [53].

For the data shown in Figures 3-7, 3-8 and 3-9, the trend in ONB is clear. ONB occurs first at the lowest mass flux, the lowest subcooling and the highest pressure. This is expected and in agreement with the physics of nucleation. Nucleating at higher pressures requires a lower superheat because of the lower surface tension, in accordance with Equation 1.1. A greater subcooling at the inlet requires more heat from the surface to establish the thermal boundary layer to support nucleation. Thus as the subcooling is increased, the heat flux input required is also increased. The single-phase heat transfer coefficient should not depend upon the subcooling significantly, in particular for the subcoolings used in this work. As such the superheat required for nucleation should be higher with a larger subcooling. Also, as previous work has shown [54, 55], a greater subcooling requires a larger superheat to initiate boiling.

Finally, ONB occurs at a lower heat flux as the flow rate is reduced. A lower mass flux will have a smaller single-phase heat transfer coefficient (as indicated by the shallower slope), i.e. the build-up of a thicker thermal boundary layer, leading to earlier ONB. Consider what occurs when the mass flux is reduced to zero. At this limit the heater is essentially in pool boiling, where ONB is expected to require a lower superheat.

Of note is how the behavior of some of the boiling curves relative to others, as will be shown in the next section, depends upon the nucleation site density as well as other boiling parameters. Several different heaters were used to complete the test matrix, and it is clear the nucleation site density varies from heater to heater. When analyzing the boiling curves, the heater used for each curve will need to be considered. For this reason, the test matrix, Figure 3-1, is color-coded based on the heater used to execute each test.

3.3 Nucleation Site Density

This section outlines the post-processing algorithm used to determine the nucleation site density from the IR data. A comparison model by Hibiki-Ishii is presented. The

experimental data is compared with the model and the results are discussed and put in context along with the boiling curves and CHF values.

3.3.1 Nucleation Site Density Post-Processing

To determine the nucleation site density (NSD) a script, developed by Seong [56], was leveraged to evaluate the relative 'activity' of each pixel from the IR temperature and heat flux distributions calculated in Section 3.2.1. The algorithm used in the script tracks the time-averaged change in temperature and heat flux. The principle behind the algorithm is the expectation that where bubbles are nucleating there will be large fluctuations in the temperature and heat flux. When a bubble is growing there will be a large heat flux at the location of the nucleation site along with a cooling of the surface due to the evaporation of the micro-layer. As the bubble continues to grow, the micro-layer underneath the bubble will evaporate leaving a dry area at the base of the bubble. When this occurs a hot spot will form where there is little heat transfer between the wall and the vapor phase. The cycling that occurs between the cool spot during the initial bubble growth and the hot spot during the end of the bubble growth will cause the nucleation area to have a higher activity than locations where constant single-phase heat transfer is occurring.

A sample output of the NSD activity algorithm is shown in Figure 3-10. Once the algorithm is complete the output is analyzed using image processing techniques to identify the high activity areas. In addition to the automatic site detection, the user can manually identify or remove nucleation sites.

From Figure 3-10 it is clear where nucleation sites are present and where only single-phase heat transfer occurs. The automatic site selection also accurately identified the center of each nucleation site. For higher heat fluxes it can be much more difficult to manually identify which areas are nucleation sites. Moreover, for higher pressures it is also increasingly difficult to identify nucleation sites as the size of the bubbles are much smaller. For the 10 bar data, the bubbles were too small to identify on the IR images so no NSD analysis was carried out.

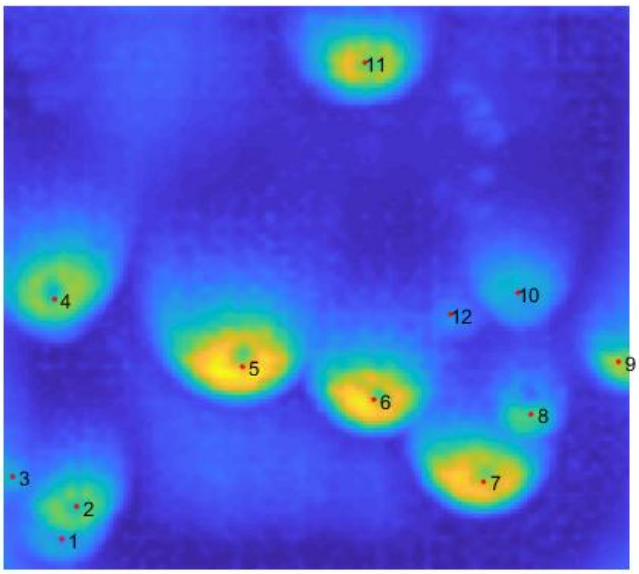

Figure 3-10: "Activity map" for 1 bar, 5 K, 1000 $\frac{kg}{m^2 s}$

3.3.2 Nucleation Site Density Comparison Model

For this work, Hibiki and Ishii's model [4] for nucleation site density was chosen as a reference model to compare the collected experimental data with theory. This model incorporates pressure, surface contact angle and cavity size to estimate the density of activatable cavities on the boiling surface, and as such is a good reference for the current work. The model is summarized in Equations 3.12- 3.15.

$$N'' = \overline{N''} \cdot \left\{1 - exp\left(-\frac{\Theta^2}{8\mu_c^2}\right)\right\} \cdot \left\{exp\left(f(\rho^+)\frac{\lambda'}{R_c}\right) - 1\right\} \tag{3.12}$$

$$\rho^+ = log\left(\frac{\rho_l - \rho_g}{\rho_g}\right) \tag{3.13}$$

$$f(\rho^+) = -0.01064 + 0.48246\rho^+ - 0.22712\rho^{+^2} + 0.05468\rho^{+^3} \tag{3.14}$$

$$R_c = \frac{2\sigma \cdot (1 + (\rho_g/\rho_f))/p}{exp\{h_{fg}(\Delta T_{sup})/(R_g T_w T_{sat})\} - 1} \tag{3.15}$$

Here $\overline{N''}$ is a reference value for the nucleation site density, 4.72 x 10^5 sites/m^2, Θ is the static contact angle for the heated surface in radians and μ_c is a reference angle for a nucleation site equal to 0.722 rad, λ' is a reference length scale to compare to the cavity size and has a value of 2.5 x 10^{-6} m. R_c is the minimum cavity radius for a given pressure and wall superheat. R_g is the gas constant for water. T_{sup} is the wall superheat and h_{fg}, ρ_l, ρ_g, σ, T_w, and T_{sat} are as previously defined.

Of interest is in this model is the implicit assumption that there is no minimum cavity size for which nucleation can occur. Note that, as the superheat increases, the minimum cavity size decreases leading to potentially unphysical cavity sizes contributing to the overall nucleation site density. Additionally, this model does not take into account any potential interaction between nucleation sites.

3.3.3 Nucleation Site Density Results

The complete results for the nucleation site density, for all of the measurable conditions, are given in Appendix A. Shown in Figure 3-11 is a sample result of the nucleation site density analysis, and in Figure 3-12 the measured nucleation site density is plotted in comparison to the Hibiki-Ishii model. Generally, the nucleation site density curves follow the expected behavior of increased nucleation site density as pressure increases and as mass flux decreases.

From Figure 3-12 there is a significant discrepancy between the experimental data and the data from the Hibiki-Ishii model. The number of nucleation sites measured experimentally is different than the number predicted by the model by two orders of magnitude or more. This is not entirely unexpected as the reference value for nucleation site used in the model, $\overline{N''}$, is calibrated to the data considered when developing the model which included metallic substrates like stainless-steel and copper. This work used a much smoother ITO surface. However, there is a significant discrepancy in the overall behavior of the nucleation site density curve as the superheat is increased. The experimental data does not increase exponentially. When viewed in a linear scale, as in Figure 3-11, there is an initial rapid increase at low superheats followed by a linear behavior once fully-developed nucleate boiling is reached.

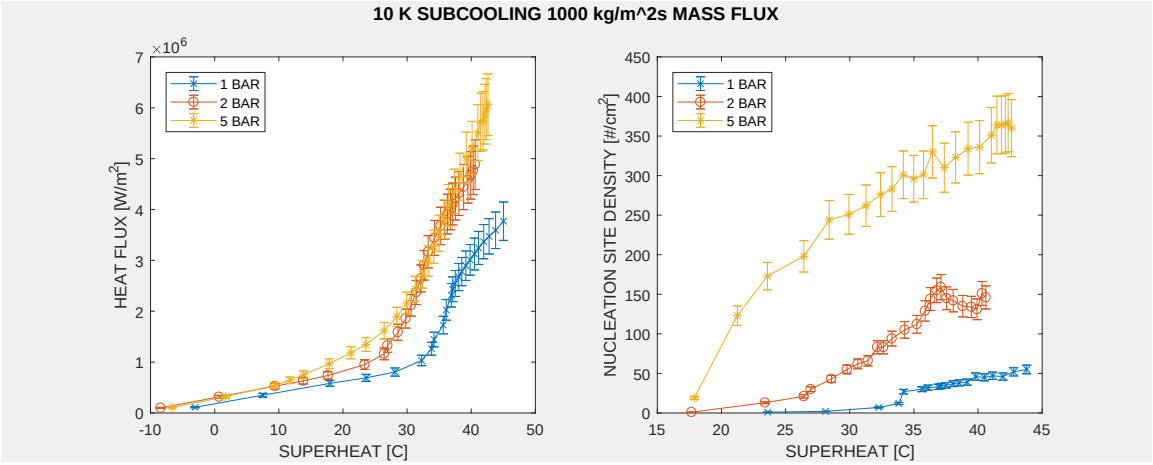

Figure 3-11: Nucleation site density result for 10 K, 1000 $\frac{k}{m^2 s}$, 1, 2 and 5 bar. Shown on the left is the boiling curve for reference. The 1 bar and 2 bar data was collected using the "Green" heater, the 5 bar data was collected using the "Blue" heater. See Figure 3-1.

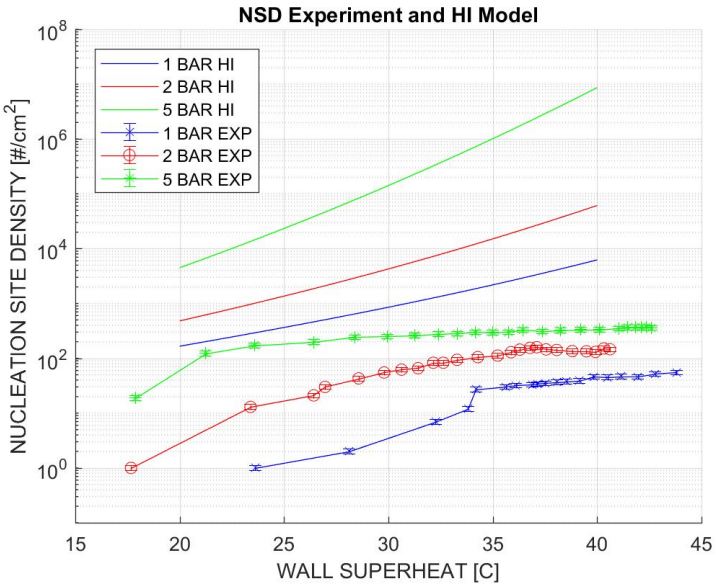

Figure 3-12: Comparison of experimentally measured nucleation site density to the Hibiki-Ishii model for nucleation site density for 10K subcooling at 1000 $\frac{kg}{m^2 s}$.

Nonetheless, there appears to be consistent saturation effect as the critical heat flux is approached.

The saturation effect was discussed by Gilman and Baglietto [3], where there could be a thermal deactivation of nearby potentially active nucleation sites when a bubble forms. As the bubble grows, the heat removed from the surface due to the phase change process cools the potential nearby nucleation sites, effectively deactivating them as they can no longer reach the required superheat to nucleate a bubble. Gilman and Baglietto proposed a Complete Spatial Randomness (CSR) model to modify the Hibiki-Ishii model and account for such the thermal deactivation effect.

For tests that used the same heater the nucleation site density has a consistent behavior. When comparing tests that used two (or more) different heaters the results are not always inline with the expected trend. For instance, consider Figure 3-13. As Figure 3-1 shows, for 2 bar and 5 K subcooling one heater was used for the 1000 and 1500 $\frac{kg}{m^2 s}$ tests and another was used for the 2000 $\frac{kg}{m^2 s}$ test.

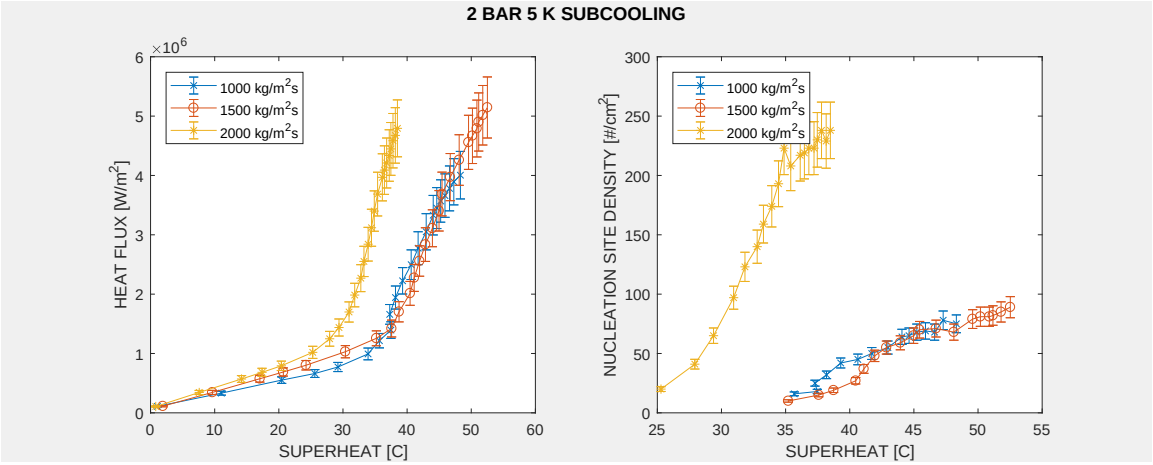

Figure 3-13: Boiling curve and nucleation site density for 2 bar, 5K and all mass fluxes. The 1000 and 1500 $\frac{kg}{m^2 s}$ data was collected using the "Green" heater and the 2000 $\frac{kg}{m^2 s}$ data was collected using the "Red" heater. See Figure 3-1.

The boiling curves for this series do show a discrepancy where the 2000 $\frac{kg}{m^2 s}$ test has a much earlier ONB point than the other two, inconsistent with what would be expected where a higher mass flux would delay ONB. Further, when considering the CHF values for 1500 and 2000 $\frac{kg}{m^2 s}$, see Figure 3-28, the 2000 $\frac{kg}{m^2 s}$ condition has a

lower CHF value that the 1500 $\frac{kg}{m^2 s}$ case. CHF is expected to be higher with higher mass flux [57]. However, both of these abnormalities are resolved when the nucleation site density is considered. The 2000$\frac{kg}{m^2 s}$ condition has a significantly higher nucleation site density than either of the 1000 $\frac{kg}{m^2 s}$ or 1500$\frac{kg}{m^2 s}$ cases. The other cases have very similar nucleation site densities, as expected, as they both used the same heater. The 2000 $\frac{kg}{m^2 s}$ case used a separate heater and has a distinctively different nucleation site density. Nucleation occurs at a much earlier superheat, accounting for the earlier ONB on the boiling curve, and the saturated value is much higher than either of the other two cases. A higher nucleation site density, at high heat fluxes, results in a greater probability of bubbles from neighboring nucleation sites to coalesce. When multiple bubbles coalesce on the surface their dry spots can merge which can trigger CHF.

This result, along with the rest of the data, demonstrates the importance of accurately quantifying the nucleation site density and capturing the physics when considering a boiling model. Changes in the boiling surface, name the density and size of the nucleation sites can have a significant impact on the resulting boiling heat transfer. When characterized using a boiling curve the discrepancy between surfaces becomes clear.

3.4 Bubble Period, Growth Time and Wait Time

This section outlines the process used for determining the bubble period, growth time and wait time from the IR data. Boiling models for calculating the period, growth time and wait time are presented. The data is compared with the models and the results are discussed.

3.4.1 Bubble Period, Growth Time and Wait Time Post-Processing

The post-processing algorithm for analyzing the bubble period, growth time and wait time is described hereafter.

The method requires the nucleation site locations as determined from the activity

map outlined in Section 3.3.1. Once the location of a nucleation site is known, the time evolution of the temperature and heat flux can be plotted. A representation of these plots is shown in Figure 3-14. The logical progress of the temperature at the center of the nucleation yields the growth and wait times. When the bubbles grows, it draws heat from the surface to generate vapor which cools the surface. After the bubble departs the wall temperature will continue to rise until it reaches the superheat required to initiate the growth of another bubble. Thus, the temperature maxima indicate the beginning of the growth time, and the temperature minima indicate the beginning of the wait time.

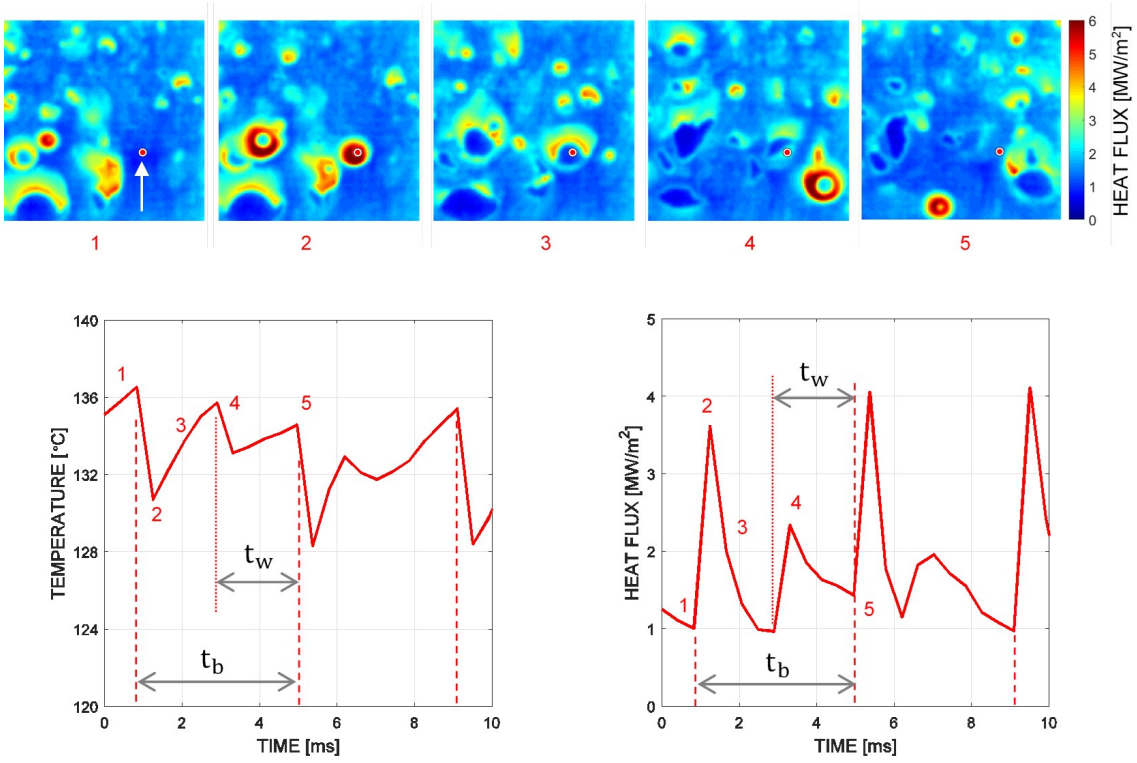

Figure 3-14: Depiction of the algorithm used to determine the growth time and wait time. Adapted from Richenderfer et al [60].

A similar analysis can be done using the heat flux where the heat flux increases during the growth time, due to the evaporation of the liquid phase. The heat flux decreases during the wait time since the heat transfer is essentially single-phase convection with a constantly decreasing ΔT as the superheated layer builds up near the wall.

The bubble frequency is simply the inverse of the bubble period, which can be determined from the growth and wait times.

$$f = \frac{1}{\tau} = \frac{1}{t_g + t_w} \tag{3.16}$$

3.4.2 Bubble Period, Growth Time and Wait Time Comparison Models

The Cole model [5] is a correlation for determining the bubble frequency from the bubble departure diameter. The Cole model is well established and has been implemented into several system codes. The frequency correlation is based on an analysis of a saturated pool boiling experiment using HSV. The main assumption is that CHF occurs when a newly formed bubble on the boiling surface coalesces with recently departed bubble that has insufficient velocity to rise away from the surface before the two bubbles coalesce. The assumption is quantified in Equation 3.17.

$$f \cdot D_d = u_b \tag{3.17}$$

Here, f is the nucleation frequency, D_d is the departure diameter and u_b is the velocity of the bubble after it has departed the surface. The velocity is solved for by equating the drag and buoyancy forces which yields an equation relating the bubble departure diameter to the bubble frequency.

$$f = \sqrt{\frac{4g(\rho_l - \rho_v)}{3\rho_l D_d}} \tag{3.18}$$

The wait time model used for comparison was recently developed at MIT [8]. The model is based off a conduction analysis using the same heater and boiling geometry used in this work. The model solves for the wait time as the time between when a bubble departs the surface, and when the surface reaches the requisite superheat to initiate boiling, in accordance with Hsu's criterion [59]. They propose a multi-layer conduction analysis, with an effective thermal diffusivity to account for the quenching

component of the heat transfer from the surface, to calculate the wait time.

$$t_{wait} = \frac{\pi}{4}\left(\frac{(\epsilon_s + \epsilon_w)\cdot(T_{sat}(P_0 + \frac{2\sigma}{R_c}) - T_{bulk}) - \epsilon_s \cdot (T_{wall} - T_{bulk})}{q''_{tot}} + \frac{R_c}{\sqrt{a_w}}\right)^2 \quad (3.19)$$

Here, ϵ_s and ϵ_w are the substrate and water effusivities, respectively. T_{sat} is the saturation temperature at the sum of the system pressure and the cavity over-pressure. a_w is the thermal diffusivity of the substrate. The other terms are as previously defined. The growth time model used is under development at MIT as part of bubble departure diameter model and is presented in the bubble departure diameter section.

3.4.3 Bubble Period, Growth Time and Wait Time Results

The complete results for the bubble period, growth time and wait time, for all measurable conditions are presented in Appendix C. Presented here is a sample comparison of the results for the 1 bar, 10 K subcooling and 1000 $\frac{kg}{m^2 s}$ mass flux, see Figure 3-15. The bubble departure diameter used as input for the models described in Section 3.4.2 was determined from the experimental data along with the wall temperature and heat flux. The cavity radius used was 5 μm, which is a typical value for for the ITO heaters used in this work [60].

The results show good agreement between the experimentally measured growth and wait times and the corresponding models. In particular, the wait time model captures the decreasing wait time with increased heat flux very well. The bubble period as calculated from the Cole model consistently over-predicts the experimentally measured bubble period. Moreover, as the Cole model does not directly take into account the wall superheat or heat flux, rather it relies upon the bubble departure diameter to reflect those trends. The curve depicting the Cole model in Figure 3.4.3 was calculated using a bubble departure diameter of 1.5 mm.

The results from the data taken at 1 and 2 bar show the wait time is consistently the dominant term in the bubble period. The growth time is consistently between 0.5 to 1 second, while the wait time is between 1 to 5 seconds with the exception of

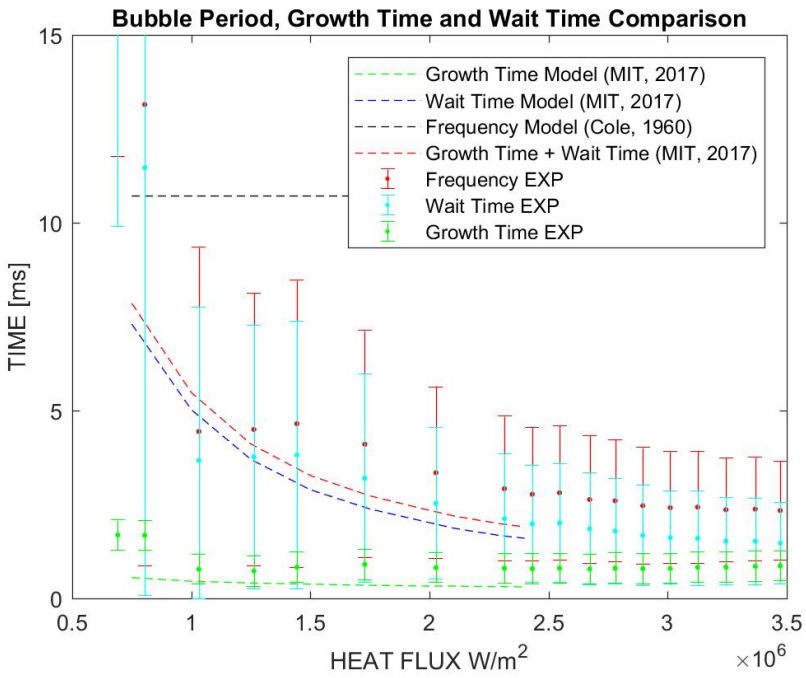

Figure 3-15: Comparison of experimental data for bubble period, growth time and wait time to models.

very low heat fluxes. The growth time does not change significantly as the heat flux (and wall superheat) increases. The wait time, and consequently the bubble period, decreases as the heat flux increases. This behavior is expected as the increased heat flux will regenerate the thermal boundary layer quicker, leading to nucleation quicker. For the experimental conditions explored in this work, there does not appear to be a significant dependence on the mass flux or subcooling for either the growth time or wait time. The wait time does appear to be lower for 2 bar, as is expected since the superheat required for 2 bar would be smaller.

Note, growth time and wait time data for 5 and 10 bar regimes was not generated due to a lack of spatial and temporal resolution with the IR camera.

3.5 Bubble Departure Diameter

This section outlines the algorithm used for determining the bubble departure diameter using the IR and HSV images. A model to compare the experimental data to is

presented and the results are discussed.

3.5.1 Bubble Departure Diameter Post-Processing

The bubble departure diameter is determined using a combination of the IR and HSV images. The algorithm was developed by Ravikishore Kommajosyula. The IR videos are leveraged to determine the location of active nucleation sites, as described in Section 3.3.1, and to determine when a bubble has departed the nucleation site. For clarification, departure can include either the bubble lifting off the surface and entering the bulk flow, or departing the nucleation site by sliding along the surface. Bubble departure is determined based on the time evolution of the temperature and heat flux images.

The HSV is used to determine the bubble diameter using an area detection image processing technique. A sample output is shown in Figure 3-16. The area highlighted in red is the measured bubble diameter. The green "x" markers indicate the location of a nucleation site. Note, this technique measures the projected bubble diameter using the front-view of the heater and determines the equivalent diameter from the projected area. This assumes minimal non-sphericity of the bubble. Ideally, the equivalent diameter would be calculated from the measured volume of the bubble.

The measured departure diameter is only accepted if it meets two criteria. The first is the bubble must have a minimum circularity defined by:

$$C = \frac{4\pi A}{P^2} \tag{3.20}$$

Here A is the area, and P is the perimeter. This number measures the circularity of the bubble and should be as close to one as possible. The second criteria is that the bubble must have a nearby nucleation site close to the centroid. This ensures the bubble originated near that nucleation site and is not counted twice.

Since the bubble departure diameter analysis requires synchronized HSV and IR data, only six data points were collected at each pressure. The conditions considered at each pressure were 10 K subcooling at 1000, 1500 and 2000 $\frac{kg}{m^2 s}$. Two heat

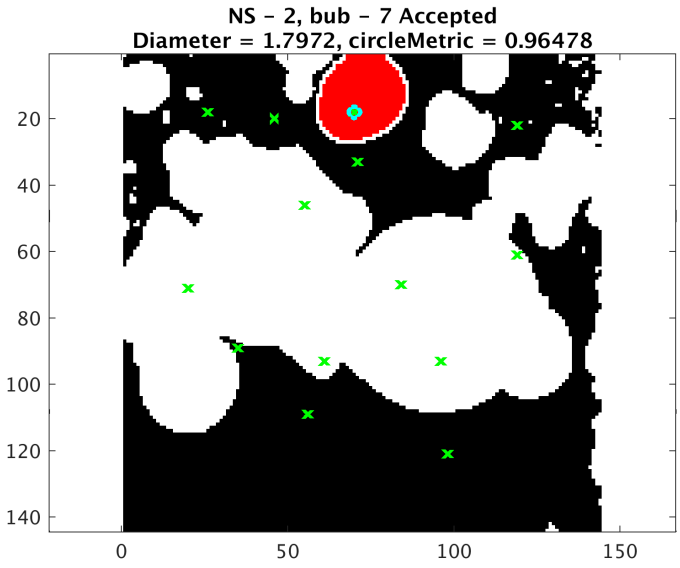

Figure 3-16: An accepted bubble departure diameter from the bubble departure diameter algorithm. Image courtesy of Ravikishore Kommajosyula

fluxes were captured at each condition. The first was determined by the first visual confirmation of boiling on the surface. The second heat flux was determined by the an estimation of the maximum heat flux possible where individual bubbles were still distinct. At high heat fluxes the bubbles on the surface can merge quite rapidly which makes post-processing the departure diameter near impossible.

3.5.2 Bubble Departure Comparison Model

The model chosen for comparison for the bubble departure diameter was developed by Mazzocco et al. [6] at MIT. The model reassesses the force balance on the bubble and add additional physics to account for the micro-layer evaporation and the heat transfer between the bubble and the surrounding fluid during the growth phase. In particular, the model accounts for heat transfer away from the bubble in subcooled flows. They note that in saturated flows, the superheated layer surrounding the bubble will continue to transfer heat and mass to the bubble. However, in subcooled flows, the bubble cap will experience condensation due to the fluid at the bubble cap being below the saturation temperature. The bubble growth phase is summarized in

the following equations:

$$R(t_g) = (K_{ML} + K_{FB})t^{0.5} \tag{3.21}$$

$$K_{ML} = 2\frac{\pi^2 + 1}{\pi^{5/2}} \cdot \frac{1}{\sqrt{Pr}} \cdot Ja\sqrt{\eta_l} \tag{3.22}$$

$$K_{FB} = \chi \cdot 2\sqrt{\frac{3}{\pi}} Ja_w^* \sqrt{\eta_l} \tag{3.23}$$

Here, R is the bubble radius, K_{ML} is the bubble growth rate constant from the evaporation of the micro-layer, K_{FB} is the growth rate constant due to heat transfer from the surrounding liquid, η_l is the thermal diffusivity of the liquid and Ja is the Jakob number. The other variables are as previously defined.

The model captures the separate effects between saturation and subcooled flows using a fitted parameter, χ.

$$\chi = A - \zeta B \tag{3.24}$$

A and B are fitted values, with $A = 1.55$ and $B = 0$ for saturated flows, and $A = 0$ and $B = 0.05$ for subcooled flow. ζ for subcooled flow is defined as:

$$\zeta = \frac{T_{sat} - T_{bulk}}{T_{wall} - T_{sat}} \tag{3.25}$$

The remainder of the model considers each force acting on the bubble and presents a formulation to quantify each force. The balance of the forces is presented with the lift-off criterion that the force away from the wall F_y must be greater than zero for lift-off to occur.

3.5.3 Bubble Departure Diameter Results

Mazzocco's model predicts the average value of the departure diameter well at higher nucleation temperatures. However, the model under-predicts the bubble diameter at

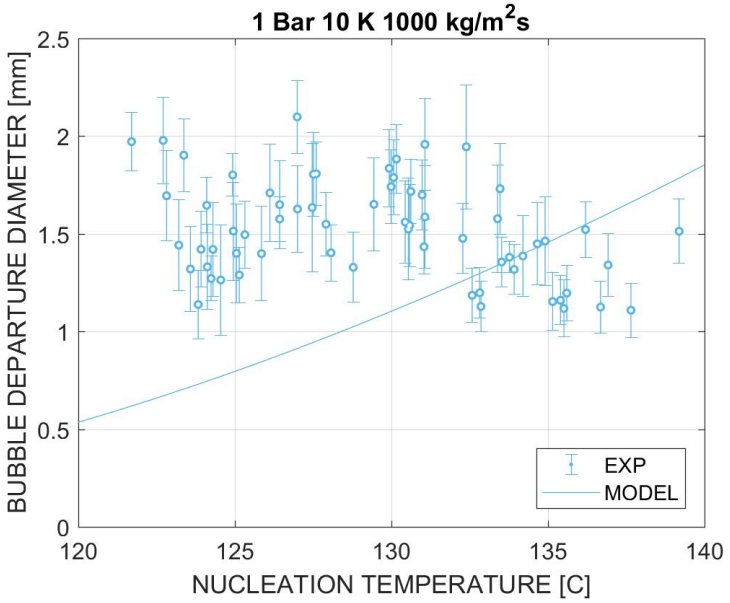

Figure 3-17: An accepted bubble departure diameter from the bubble departure diameter algorithm. Image courtesy of Ravikishore Kommajosyula

lower nucleation temperatures. Moreover, the data doesn't reflect quite as strong of a dependence on the nucleation temperature as the Mazzocco model. The bubble departure diameter for the 1 bar, 10 K subcooling and 1000 $\frac{kg}{m^2s}$ test case, shown in Figure 3-17 was nearly constant at approximately 1.5 mm. The bubble departure diameter for previously collected data at 500 $\frac{kg}{m^2s}$ is shown in Figure 3-18. The model matches well with the data collected at 500 $\frac{kg}{m^2s}$.

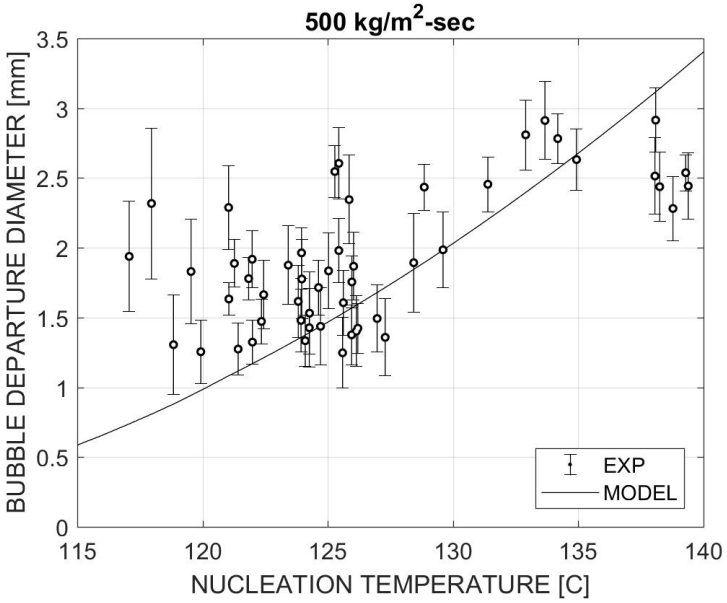

Figure 3-18: An accepted bubble departure diameter from the bubble departure diameter algorithm. Image courtesy of Ravikishore Kommajosyula

3.6 Heat Flux Partitioning

This section outlines the algorithm used for determining the partitioned heat flux from the experimental data, the heat flux partitioning model from Kurul and Podowski, and presents the complete heat flux partitioning data from the subcooled flow boiling experiments.

3.6.1 Heat Flux Partitioning Post-Processing

An image processing technique, developed by Jee Seong [56], was used to determine the heat flux partitioning of the flow boiling data using the heat flux and temperature distributions obtained from the radiation-conduction algorithm. The principle behind the algorithm is to identify the separate dry, evaporation and wetted areas on the heater. To do so, the heat flux distribution is leveraged to identify each of the regions based on the relative heat flux at each pixel. Similar approaches were used by Jung [28] and Jung and Kim [29] for pool boiling. The assumption made is the circular high heat flux regions are attributed to evaporation and are characteristic of bubble growth, with a low heat flux dry spot forming within the evaporation ring. The remaining area

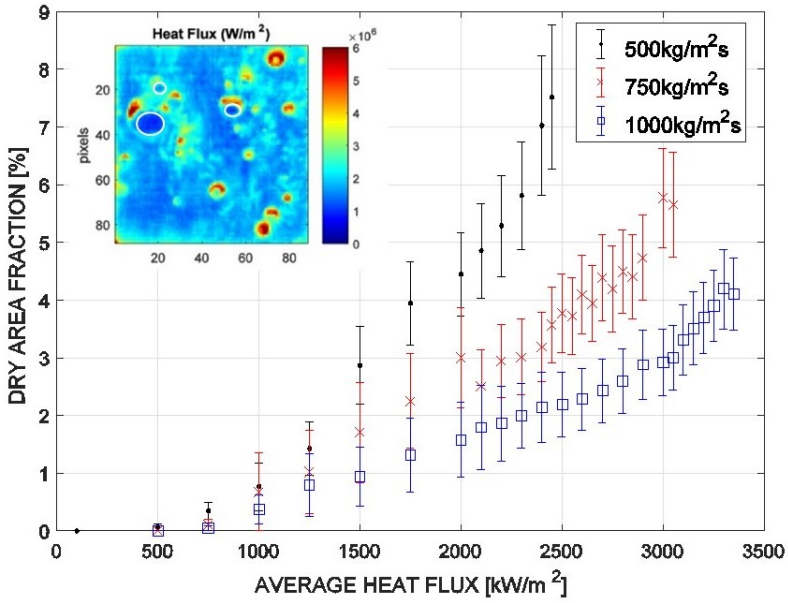

Figure 3-19: Dry area fraction as a function of applied heat flux. Also shown is a heat flux distribution from a single IR frame. The areas encircled in white are the dry regions.

is deemed single-phase heat transfer. A forced convection heat transfer coefficient is calculated using the single-phase heat transfer points of the boiling curve to determine the amount of single-phase heat transfer attributed to forced convection. Quenching is attributed to the remaining single-phase heat transfer that occurs, and is calculated as $q''_q = q''_{sp} - q''_{fc}$.

Figure 3-19 depicts the dry area fraction of the heater and the identification of the dry area within the bubbles as seen in the pictured heat flux distribution frame. The regions identified as dry area are tabulated and the collective heat flux from each of those pixels is then averaged to determine the average dry area heat flux. A similar analysis is done for the evaporation and single-phase heat transfer (including forced convection and quenching). For the calculated dry area itself, the trend is as expected. The fraction of the heated area which is dry increases with the applied heat flux. This is due to more nucleation sites being active and an increase in the nucleation frequency for each site as the heat flux and wall superheat increase. This leads to a greater number of bubbles growing on the boiling surface at a given instant, which in turn yields a great dry area fraction due to the dry spots under each of the

bubbles where the micro-layer has evaporated.

3.6.2 Heat Flux Partitioning Comparison Model

The heat flux partitioning model by Kurul and Podowski, called the "RPI Model", is one of the most popular heat flux partitioning models and has been the starting point for many researchers in attempts to refine the model. The model is lauded for its predominantly mechanistic approach to partitioning the wall heat flux between the separate heat transfer mechanisms. The model uses fundamental boiling variables including the wall superheat, bulk fluid subcooling, nucleation site density, nucleation frequency, wait time, bubble departure diameter and single-phase heat transfer coefficient to model three different partitioned heat fluxes: single-phase forced convection, evaporation and quenching.

$$q''_e = N'' f \cdot \frac{\pi}{6} D_d^3 \cdot \rho_v h_{fg} \tag{3.26}$$

Here q''_e is the evaporation heat flux and $\frac{\pi}{6} D_d^3$ is the volume of a spherical bubble with a volume equal to the departure volume. The other terms N'', f, ρ_v and h_{fg} are as previously described. The model calculates the evaporation heat flux by assuming all of the vapor generation to form the vapor bubble comes from the wall. The nucleation site density and frequency scale to account for multiple nucleation site and the frequency with which each site nucleates a bubble.

$$q''_q = f \cdot N'' K (\frac{\pi}{4} D_d^2) \cdot 2\sqrt{\frac{\rho_l c_{p,l} k_l t_w}{\pi}} \cdot (T_{wall} - T_{bulk}) \tag{3.27}$$

The quenching term, q''_q, is calculated assuming once a bubble departs the surface, cool subcooled water rushes in to replace the volume previous occupied by the bubble. The factor $K \frac{\pi}{4} D_d^2$ is the area of influence for this mechanism. The factor K typically accounts for the additional nearby area that is effected. A schematic of this geometry is shown in Figure 3-20. The square root term accounts for the conduction from the heated wall to subcooled liquid that re-establishes the thermal boundary layer that was disrupted by the departing bubble.

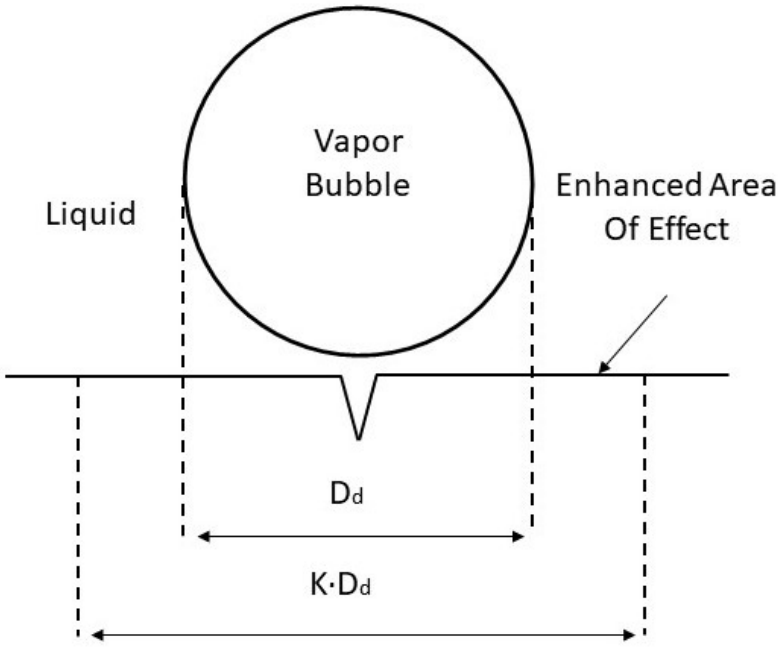

Figure 3-20: Schematic of the effect of the K term from the RPI model for the quenching heat flux.

$$q''_{fc} = (1 - N''K\frac{\pi}{4}D_d^2) \cdot h_{fc} \cdot (T_{wall} - T_{bulk}) \tag{3.28}$$

The final term is the single-phase forced convection heat transfer, q''_{fc}. As the boiling area of effect was previous determined in the quenching term, the forced convection area of influence is simply the remaining area of the heated surface. The heat transfer coefficient h_{fc} is calculated via correlation.

This model is mechanistic in that it builds the individual heat fluxes using quantifiable boiling variables with the single exception of the K term in the area of influence of the quenching term. As previously stated, the goal of this work is provide experimental data and insight on subcooled flow boiling for inspiration and validation of mechanistic boiling models like the RPI model or more advanced models.

3.6.3 Heat Flux Partitioning Results

The complete results for the heat flux partitioning, for all measurable conditions are presented in Appendix D. Presented here is the heat flux partitioning for the 1 bar

pressure, 10 K subcooling and 1000 $\frac{kg}{m^2 s}$ regime. It is important to note the mechanisms described in the RPI model for each term and the experimentally measured mechanisms for each term do not always correspond. For example, the evaporation term in the RPI model is captured using the bubble volume. In the experiment, the evaporation heat flux is measured at the surface by indentifying the areas where the micro-layer evaporation is measured. The physics of each mechanism for both the RPI model and the experimental measurement are given in Table 3.1.

	RPI Model	**Experiment**
Evaporation	Volume of Bubble	Micro-layer Evaporation
Quenching	Rebuilding Boundary Layer	Enhancement of Single-Phase
Forced Convection	Heat Transfer Coefficient	Heat Transfer Coefficient
Sliding Conduction	-	Enhancement of Single-Phase
Areas of Effect	Nucleation Site Density and Nucleation Frequency	Directly Measured

Table 3.1: Summary of mechanisms for heat flux partitioning for the RPI model and the measured experimental data.

The four curves quantify the average partitioned heat fluxes at each measured step along the boiling curve. Note the single-phase (green) curve is the sum of the quenching (cyan) and forced convection (blue) curves, $q_{sp} = q_q + q_{fc}$. Each of the partitioned heat fluxes follow the expected trends when considering the physics. The forced convection term starts as the dominant term, and accounts for the entire heat removal from the surface when there are no nucleation sites active. As the heat flux is increased, the contribution from the forced convection term reduces as the area of the heater where only forced convection occurs decreases due to the boiling area increasing. For this case, when CHF is reached, the forced convection term accounts for less than 10% of the total heat removed from the surface.

The evaporation term begins at zero when there are no bubbles nucleating. As the applied heat flux increases, the wall superheat also increases which leads to activation

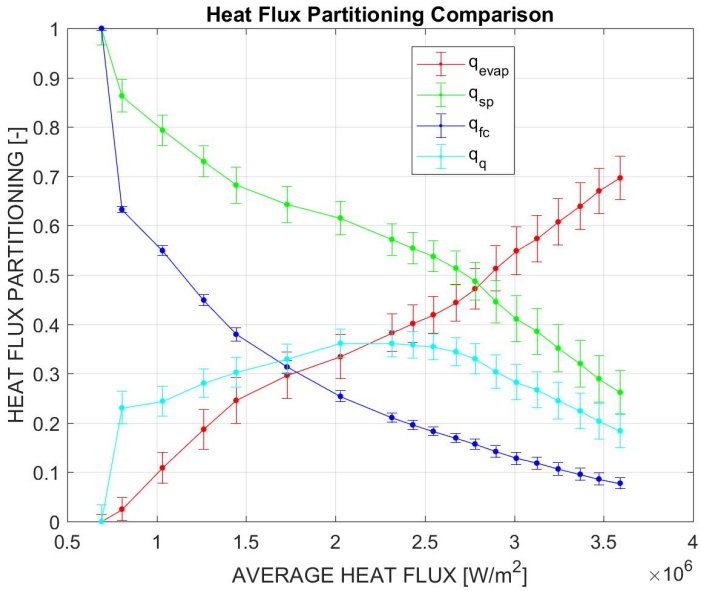

Figure 3-21: Experimentally measured fractional heat flux partitioning for 1 bar pressure, 10 K subcooling and 1000 $\frac{kg}{m^2 s}$ test case.

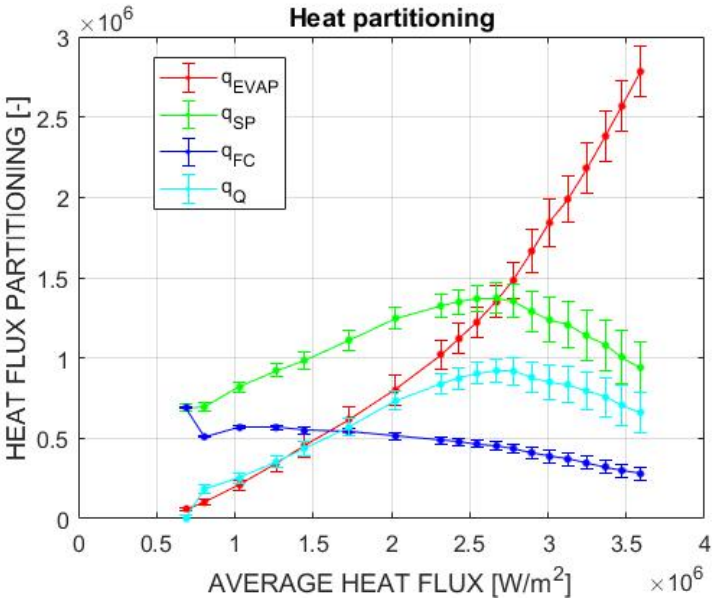

Figure 3-22: Experimentally measured total heat flux partitioning for 1 bar pressure, 10 K subcooling and 1000 $\frac{kg}{m^2 s}$ test case.

of more sites. As more sites are activated the fractional area over which boiling takes place increases. Moreover, the frequency of bubbles nucleating at each site also increases, as shown in Section 3.4.3, which results in a greater amount of evaporation heat transfer. The quenching term has an initially large effect on the total heat transfer. Indeed at low heat fluxes, a more significant amount of energy is transferred to the liquid during the quench phase, before conditions for a new nucleation can be obtained. Quenching continues to increase as more nucleation sites are activated, resulting in more instances of quenching occurring as bubbles depart the surface. However, the relative amount of quenching decreases as the wait time decreases at higher heat fluxes.

Since both the heat flux partitioning and the individual boiling variables were measured independently, the measured values of the boiling variables can be input into the RPI heat flux partitioning model and a direct comparison between the results of the model and the results of the experiment can be made. This comparison is shown in Figure 3-23. A summary of the input variables and their measurement technique is shown in Table 3.2.

In Figure 3-23, the results of the RPI model are shown as the dashed lines. The trends are vastly different from those seen experimentally, namely the quenching term is extremely over-predicted. At just above 1 MW/m^2 of total input heat flux, the quenching term accounts for 90% of the heat removed from the surface. This is clearly unphysical and is due to a possible weakness in the RPI model.

Variable	**Measurement**
Wall Superheat	Radiation-Conduction Algorithm
Nucleation Site Density	Activity Map
Wait Time	Temporal Temperature Profile
Frequency	Temporal Temperature Profile
Bubble Departure Diameter	HSV + NSD Detection
Heat Transfer Coefficient	Boiling Curve
Bulk Fluid Temperature	Imposed Condition
Boiling Area of Effect	Built-in RPI model

Table 3.2: Variables used for RPI model and the method of measurement.

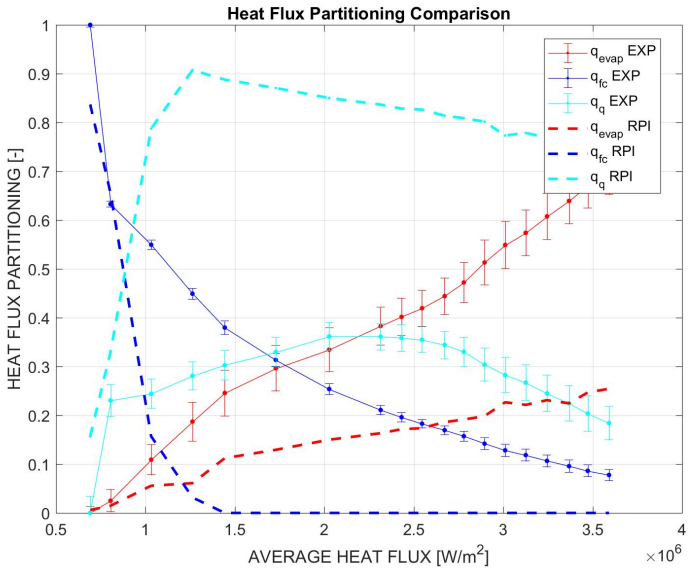

Figure 3-23: Comparison of the experimental measured heat flux partitioning and the heat flux partitioning results from the RPI model using the experimental measured boiling variables as inputs. The operating condition is 1 bar, 10 K, 1000 $\frac{kg}{m^2 s}$

Considering Equation 3.27, the boiling area term will rapidly grow with the nucleation site density. Further, there are no physics in place to account for the fractional area of effect to increase beyond unity. Indeed this is the case for Figure 3-23. An artificial limit of unity was imposed on the boiling fractional area to yield the results shown here, seen in Figure 3-24.

The nucleation site density input must account for the interaction of the nucleation sites independent of the heat flux partitioning model. The boiling fractional area input must account for the instantaneous active nucleation site density. Clearly, using a correlation for nucleation site density model such as the Hibiki-Ishii model with an unbounded solution will yield results similar to Figure 3-23.

Knowing the weakness of the area term in the RPI model prevents a useful comparison of the experimental data to the model, an exception was made to use the experimentally measured areas of influence as an input to the RPI model rather than use the mechanistic term as initially defined in the model. The fractional areas calculated from the heat flux partitioning analysis and input into the RPI model are

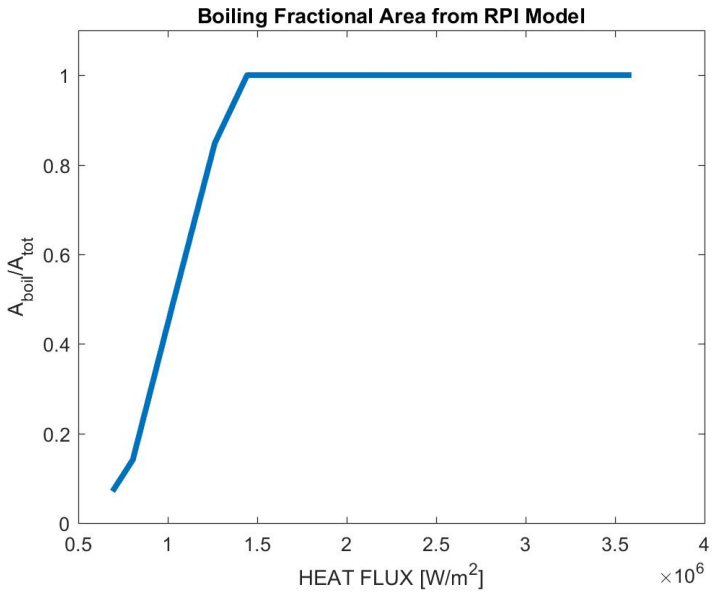

Figure 3-24: The fractional boiling area used for the quenching term in the RPI model. The operating condition is 1 bar, 10 K, 1000 $\frac{kg}{m^2 s}$

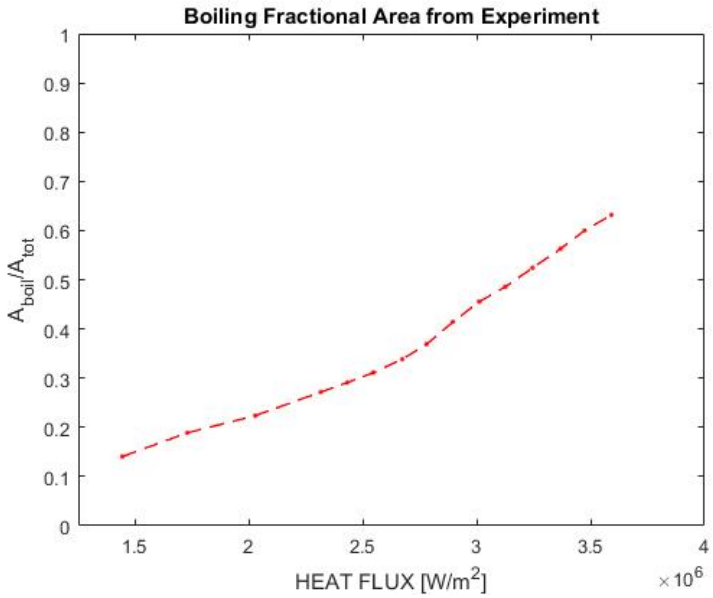

Figure 3-25: The experimentally measured fractional boiling area. The operating condition is 1 bar, 10 K, 1000 $\frac{kg}{m^2 s}$

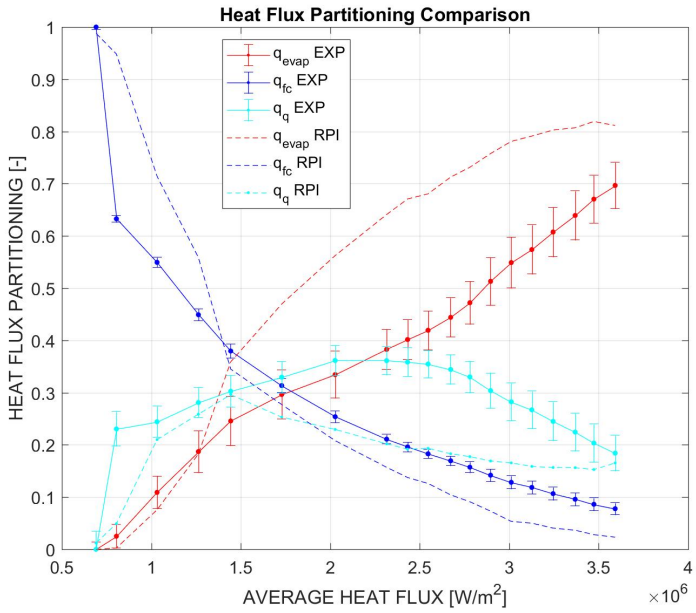

Figure 3-26: Comparison of the experimental measured heat flux partitioning and the heat flux partitioning results from the RPI model using the experimental measured boiling variables as inputs.

shown in Figure 3-25.

The result of the new comparison is much improved. The model appears to capture the overall trends well, however it still comes up short when accurately partitioning the individual heat fluxes. The forced convection term is well predicted, however, there is still some significant discrepancies between the experimental evaporation and quenching terms and their respective counterparts from the RPI model. Namely, the evaporation term is significantly over-predicted. Again, this could be a result from a short-coming in the RPI model.

When the equation for the evaporation term (Equation 3.26) is considered a significant assumption appears. The evaporative heat flux is modeled using the total volume of the departed bubble. This implicitly assumes all of the energy used for the phase change process originates from the heated surface. This approach does not account for the evaporation of the thin superheated layer surrounding the bubble. This superheat layer is described by Collier and Thome [53] and other researchers, such as Mazzocco et al. [6], have proposed models which incorporate the heating from

this layer in their calculation of bubble growth.As a matter of fact, this superheat energy is transferred to the fluid during the quenching phase and it is accounted for in the quenching term.

As such, the heat transfer from the superheat layer around the bubble is accounted for twice, once in the quenching term and once in the evaporation term. This results in an over-estimation of the evaporation heat transfer term at the wall. This is further motivation concerning the need for models that account for bubble interaction, coalescence and sliding.

An additional point of comparison with the mechanistic heat flux partitioning models exists in the evaluation of the heat transfer coefficient with respect to the nucleation site density. Both the evaporation heat flux and the quenching heat flux have a linear dependence on the nucleation site density in the RPI model. The force convection partitioned heat flux goes as $1 - N''$. However as shown in Figures 3-21 and 3-26, the forced convection term has very little effect in the fully-developed nucleate boiling regime. Thus, there should be a near linear behavior between the heat transfer coefficient and the nucleation site density, if the physics of the RPI and other mechanistic models hold true.

The heat transfer coefficient is plotted against the nucleation site density, for all measurable data, in Appendix B. The result for 1 bar pressure and 10 K subcooling, for all mass fluxes is shown in Figure 3-27. A linear fit is applied to fully developed region of the heat transfer coefficient and nucleation site density curve for each data set. The result shows there does appear to be a linear trend in the data in the fully developed boiling region. The first few points have a noticeably shallower slope due to the significance of the the forced convection heat transfer at lower heat fluxes. There is an increase in the heat transfer coefficient as more nucleation sites become active until the linear trend begins once fully-developed nucleate boiling is reached.

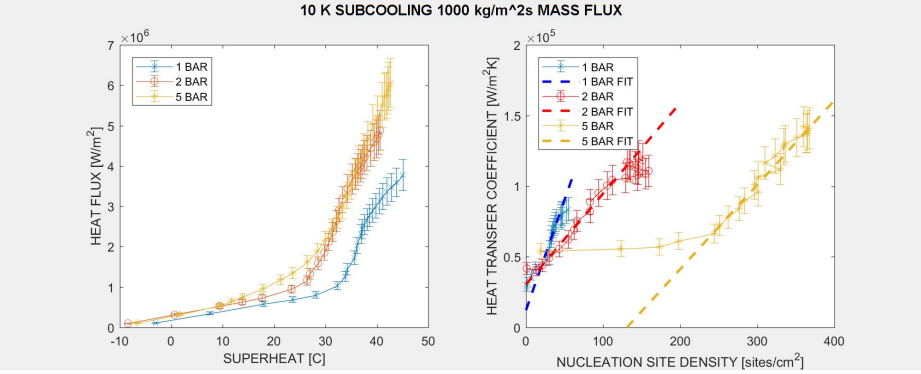

Figure 3-27: The boiling curve (left) and heat transfer coefficient against nucleation site density (right) is shown for 1 bar and 10 K regimes.

3.7 Critical Heat Flux Values

The measured values of the critical heat flux for each condition are reported in Figure 3-28. The values follow the expected trend of increased critical heat flux with increasing pressure, mass flux and subcooling [57]. The one exception is the CHF value for the 2 bar, 5 K, 2000 $\frac{kg}{m^2 s}$ test case. The CHF value is lower than the corresponding flow regime at 1500 $\frac{kg}{m^2 s}$. The expected trend is a higher CHF value at a higher mass flux according to the Groeneveld Look-up Table. However, different heaters were used for the each of the tests. Recalling Figure 3-13, the measured nucleation site density curve for the two heaters have a significant discrepancy. The "Red" heater used for the 2000 $\frac{kg}{m^2 s}$ test has a much higher nucleation site density with an earlier ONB superheat temperature than the "Green" heater used in the 1500 $\frac{kg}{m^2 s}$ test case. The maximum number of active nucleation sites at CHF is also much higher for the "Red" heater. The lower CHF value for the 2000 $\frac{kg}{m^2 s}$ test can be explained by the interaction between the increased number of active nucleation sites. The closer proximity of the nucleation sites leads to a higher chance of coalescence of multiple bubbles on the heater surface. As the bubbles coalesce, the dry spots at the base of the bubbles will merge to create a larger dry spot. The large dry area can spread and cause a DNB event.

The tabulated values in Figure 3-28 are consistently larger than the values expected using the tables and correction factors given by Groeneveld et al. This is not

	1 Bar		
	Mass Flux (kg/m^2s)		
Subcooling (K)	1000	1500	2000
5	3540	3679	4317
10	3770	4867	5207
20	4313	5403	6084
	2 Bar		
	Mass Flux (kg/m^2s)		
Subcooling (K)	1000	1500	2000
5	4004	5145	4944
10	4881	5694	6137
20	5247	6170	7241
	5 Bar		
	Mass Flux (kg/m^2s)		
Subcooling (K)	1000	1500	2000
5	6025	7197	7679
10	6197	7330	8003
20	7195	7716	8990
	10 Bar		
	Mass Flux (kg/m^2s)		
Subcooling (K)	1000	1500	2000
5	7668	9063	10800
10	8070	9360	10850
20	9005	10424	11452

Figure 3-28: Tabulated values for the point of critical heat flux for each condition in the test matrix. The cell color indicates which heater was used for the test.

unexpected as the Groeneveld table is tabulated for CHF in tubes, with a significantly longer heated length. The heater used in this work has a significantly smaller heated length. A longer heated length will allow the thermal boundary layer to completely develop. This will necessarily result in a lower CHF value than the one expected by the heater used in this work.

	1 Bar		
	Mass Flux (kg/m2s)		
Subcooling (K)	**1000**	**1500**	**2000**
5	2270	2603	2845
10	2341	2633	2875
20	2483	2692	2935
	2 Bar		
	Mass Flux (kg/m2s)		
Subcooling (K)	**1000**	**1500**	**2000**
5	2475	2892	3102
10	2532	2948	3167
20	2645	3058	3298
	5 Bar		
	Mass Flux (kg/m2s)		
Subcooling (K)	**1000**	**1500**	**2000**
5	2855	3521	3762
10	2884	3601	3860
20	2940	3760	4055
	10 Bar		
	Mass Flux (kg/m2s)		
Subcooling (K)	**1000**	**1500**	**2000**
5	3470	4365	4727
10	348	4470	4800
20	3502	4680	4944

Figure 3-29: Tabulated values for the expected point of critical heat flux for each condition in the test matrix calculated using the Groeneveld Look-up Tables [57].

Chapter 4

Uncertainty Analysis

4.1 Pressure

The pressure was measured using pressure transducers at the inlet and outlet of the pump and at the intlet of the test section. The pressure for data collection was set based on the pressure read by thet transducer at the inlet of the test section. For this work the pressure transducer used was a PX309 from Omega Engineering. The manufacturer reported accuracy is 1% of the full range, or 0.1 bar. [61].

4.2 Subcooling

The subcooling was determined using one of two thermocouples, one placed at the entrance of the test section and one placed at the exit. The thermocouples were purchased from McMaster-Carr with a stated accuracy of 0.75% of the reading. The fluid temperature varied during the course of the experiment due to the duration and variability of the heat input from the heater. The temperature excursion was typically about 0.2°C from the stated temperature. For the high pressure and temperature experiments an estimated uncertainty of the temperature would be 1.5°C. For atmospheric testing, an uncertainty of 1°C is appropriate.

4.3 Mass Flux

The uncertainty for the mass flux is determined by the accuracy of the flow meter used. For this work an Omega Engineering FTB-1400 flow meter was with a NIST-traceable calibration. The manufacturer reported accuracy is 1.0% of the reading [39]. The turbine flow meter measures the volumetric flow rate. The mass flux is then calculated using the density and the channel area. The density is quantified using steam tables and the system pressure and temperature. The temperature is known with a 1.5% uncertainty. The density difference over a 1.5% change in temperature is 1.5 $\frac{kg}{m^3}$, or 0.1% uncertainty at 10 bar pressure and 10 K subcooling. This is negligible compared to the uncertainty in the flow meter reading. The flow channel was machined with a precision of 0.1mm. The uncertainty in the area is then 1.05%. The total uncertainty is 1.8% or 18 $\frac{kg}{m^2 s}$ when measuring 1000 $\frac{kg}{m^2 s}$.

4.4 Camera Timing and Synchronization

The camera timing and synchronization was addressed by Phillips [12]. For tests with the IR and HSV video, the discrepancy between triggers was found to be less than 300 μs.

4.5 Surface Temperature

The heater surface temperature is a result of the IR camera calibration and the output of the radiation-conduction algorithm. Bucci et al. [17] validated the calibration model using an single-phase heat transfer test with an exponential power input. The output of the radiation-conduction algorithm was accurate to with 0.1°C of the analytic solution.

The reported average wall superheat temperature comes from an averaging of the values from each pixel and each frame recorded at a given heat flux and regime. The standard deviation of this average is typically between 5 to 6°C for atmospheric pressure regimes. This is expected as the temperature will fluctuate during nucleate

boiling. To report the uncertainty in the mean value, the standard error is required, which is shown in Equation 4.1.

$$\sigma_{\overline{x}} = \frac{\sigma_{T_{wall}}}{n_{pixels}} \tag{4.1}$$

Since the population used to determine the average temperature consists of 86x86x5000 pixels, the total population is then 36,980,000. The statistical uncertainty in the average temperature is 0.1%, for a measurement of 150°C, the uncertainty would be 0.15°C.

4.6 Surface Heat Flux

The heat flux is determined using the measure voltage and current from the power supply and ITO heater area that is defined using silver pads. The voltage and current were measured using a high-speed data acquisition system (HSDAS) to collect data at 2,500 Hz, the same as the frame rate of the IR camera. The average voltage and current is then determined from the collected data. The statistical error is small with respect to the error of the equipment due to the number of data points available. The accuracy of the voltage measurement is 0.001 V from the HSDAS. The current is determined by measuring the voltage across a shunt of known resistance. The voltage measurement is passed through voltage dividers before being sampled by the HSDAS. The voltage dividers have a C value of 11.34 and 10.1 These values amplify the error from the HSDAS measurement. The propagated error between the voltage and current is 1.96%.

The main source of error for the heat flux is ITO heater area. This area is set during the manufacturing process and is specified to be 1 cm^2. However, there is some discrepancy between the heaters used. All heaters came from the same batch. A conservative estimate of the tolerance in the heater area is 0.75 mm for each dimension, this accounts for not only the initial uncertainty in the heater area but also any change to the heater area that might occur during testing, such as the silver pads beginning to peal off the heater. The propagated uncertainty is then an 11% uncertainty in the

heat flux due to the area.

The total propagated uncertainty is 11.2%. The error for a 2 $\frac{MW}{m^2}$ would be 224 $\frac{kW}{m^2}$.

4.7 Nucleation Site Density

Uncertainty in the nucleation site density comes from two sources. The first is the quantification of the area of the heater, and the second is the counting of the nucleation sites. The uncertainty in the heater area was already quantified in the previous section.

Quantification of the nucleation sites is dependent upon the algorithm used to identify the nucleation sites from the activity map described in Section 3.3.1 and the spatial resolution of the camera. The temporal resolution is not of significant consequence since the activity maps averages all of the frames collected for the heat flux data point. The uncertainty will scale with the size of the bubble IR footprint in relation to the resolution of the pixels. The resolution of a single pixel is approximately 115 μm. Using the bubble departure diameter as a reference value, with the most conservative case being the 5 bar conditions with an approximate footprint of 0.5 mm, a conservative estimate of the total uncertainty would be 20%.

4.8 Bubble Period, Growth Time and Wait Time

The bubble period, growth time and wait time are determined using the temporal temperature and heat flux profiles of a given nucleation site. The measured values are then averaged across each nucleation site in a batch, and then the nucleation sites (batches) are averaged. The statistical uncertainty of this approach is small compared to the temporal resolution of the IR camera with respect to the values reported. The typical standard deviations for the bubble period and wait time are 2.5 ms and 2 ms, respectively. The standard deviations are omitted from the data in Appendix C for clarity. The uncertainty in the mean value will depend upon the integration time and

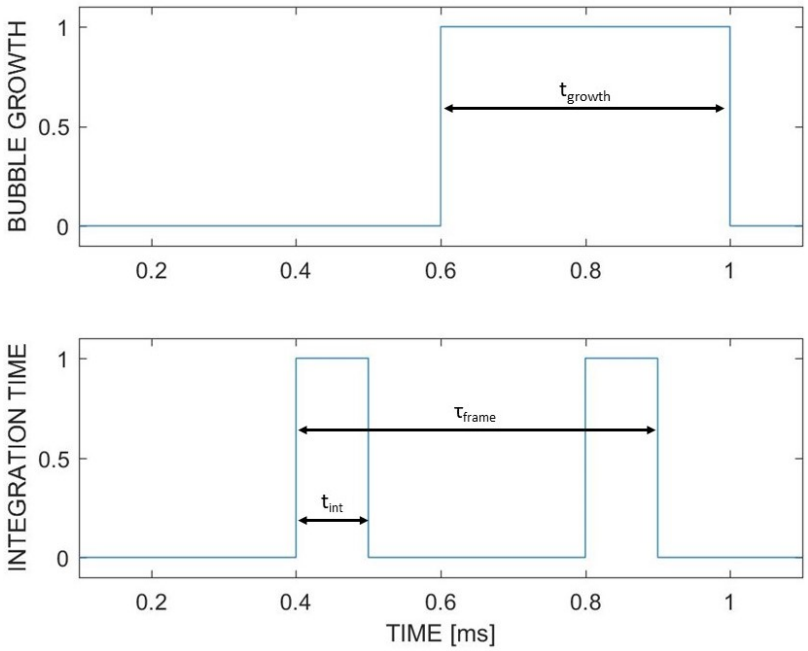

Figure 4-1: Depiction of the error in the growth time due to the camera integration time.

frame rate of the camera.

Figure 4-1 depicts how the camera integration time and frame rate contribute the error in the measurement of the growth time. The top plot shows the growth time of the bubble, while the bottom plot shows the integration time of the camera relative to the growth time. Depicted is the most conservative scenario for estimating the error. The bubble growth period begins and ends outside of the integration time of the camera. In this scenario, the maximum under-prediction of the growth time is 0.4 ms, where the bubble begins to grow at the beginning of the first frame, and then departs the surface just before the beginning of the subsequent frame. The best case scenario is the growth time is perfectly predicted by starting at the beginning of the frame, and ending at the end of the frame or the end of any subsequent frame.

4.9 Bubble Departure Diameter

The error in the bubble departure diameter is determined by the resolution of the HSV camera. Recall, the IR camera is used to locate the nucleation site and the moment

the bubble departs, but the HSV camera is used for quantification of the bubble departure diameter.The bubble departure diameter is measured using the front view project area. In the case of highly non-spherical bubble the resulting bubble departure diameter could be erroneous. The bubble departure diameter can be determined to within one pixel of the camera, thus the error is the ratio of the resolution of the camera to the size of the measured bubble departure diameter. The resolution of the HSV camera is 67 μm per pixel. The errors for bubble departure diameters of 0.5, 1.0 and 1.5 mm are 4.5%, 6.7% and 13.4%, respectively.

The standard deviation of the average measured departure diameter is plotted with the data.

4.10 Heat Flux Partitioning

The uncertainy from the heat flux partitioning is attributed to the quantification of the area of effect for each component. Similar to the bubble departure diameter, the area is quantification is limited by the resolution of the IR camera. The uncertainty in the area is quantified using Equation 4.2.

$$\delta A = \frac{\partial A}{\partial D} \cdot \delta D = \frac{\partial}{\partial D}\left(\frac{\pi D^2}{4}\right)\delta D = \frac{\pi D}{2}\delta D \tag{4.2}$$

For an area with a diameter of 1 mm, the error is:

$$\frac{\delta A}{A} = \frac{\frac{\pi D \delta D}{2}}{\frac{\pi D^2}{4}} = \frac{2\delta D}{D} = 23\% \tag{4.3}$$

This assumes the area is circular, such as the evaporation area of the bubble. For irregular shapes the quantification can be different. The standard deviation of the measured heat flux partitioning is plotted with the data.

Chapter 5

Summary and Conclusions

5.1 Summary

A high-pressure flow facility was designed and constructed to run experimental flow boiling tests up to 10 bar and 180 C. A custom test section was designed to enable high-speed IR thermometry and high-speed video diagnostics for data collection. Two original safety systems were created, a burnout prevention system and a polarity switching system, which enable safe operation of the loop up to CHF.

A unique database was created for high-pressure, high-temperature flow boiling data using IR thermometry. The complete nucleate boiling curve, including CHF, was collected at 1, 2, 5 and 10 bar pressure, with 5, 10 and 20 K subcooling at 1000, 1500 and 2000 $\frac{kg}{m^2 s}$ using IR thermometry.

An IR camera was used at 2,500 Hz at a 115 μm resolution, along with a HSV camera operated at 20,000 Hz with a 67 μm resolution. Advanced post-processing techniques were used to post-process the IR and HSV data to extract individual boiling parameters including the nucleation site density, bubble period, growth time, wait time and bubble departure diameter. A radiation-conduction post-processing algorithm allowed for the determination of the time-resolved 2-D surface temperature and heat flux distributions. Additionally, a new image processing technique was used to determine the complete heat flux partitioning of the flow boiling data.

An analysis of the data was performed to compare the results of each post-

processed variable with predictive boiling models. The individual boiling variables were used to compare the experimentally measured heat flux partitioning with the heat flux partitioning from the RPI model. Insights were made when a clear discrepancy between the data and the predictive models appeared.

5.2 Conclusions

The nucleation site densities measured were much lower than what is predicted by Hibiki-Ishii, by almost two orders of magnitude. This was not unexpected as the average nucleation site density tuning factor for the correlation was based on experimental data using metallic surfaces. The ITO used in this work is nano-smooth with imperfections due to the machined sapphire substrate. However, the measured nucleation site density did not increase exponentially with wall superheat as predicted by Hibiki-Ishii model. Instead, the nucleation site density reached a plateau just before the critical heat flux was reached. This suggested there was a saturation effect, likely due to interaction between neighboring nucleation sites.

A comparison of boiling curves that used different heaters demonstrated the effect nucleation site density has on the boiling physics. When a heater with a significantly higher nucleation site density (likely due to the presence of larger cavities) was used, the onset of nucleate boiling occurred at a lower than expected superheat, and the value of critical heat flux was also lower than expected. Additionally, at fully developed nucleate boiling, a linear trend was observed between the nucleation site density and heat transfer coefficient, as predicted by the RPI model.

The bubble period, growth time and wait time data agreed well with the MIT growth time and wait time models. The Cole model, which correlates the bubble frequency to the departure diameter, over-predicted the bubble period significantly, and did not follow the trends of decreasing period at higher heat fluxes. This suggests there are additional physics involved which are not captured in the Cole model. The wait time was found to be the dominant term in the bubble period, and decreased significantly as the heat flux was increased. The growth time remained near constant

with increasing heat flux and superheat. These trends were consistent between the various pressure, subcooling and mass flux regimes. The wait time was marginally higher for 1 bar regimes than it was for 2 bar regimes.

The heat flux partitioning results showed the evaporation heat flux is small at lower heat fluxes but increases to account for over 50% of the total heat flux as CHF is approached. The quenching term increases with the evaporation term initially, but the relative contribution decreases at higher heat fluxes as the wait time decreases.

The experimentally measured boiling variables were input into the RPI heat flux partitioning model to compare the predicted heat flux partitioning to the experimentally measured heat flux partitioning. When the complete RPI model was used the result was illogical as the quenching term was the dominant term even at very low heat fluxes where forced convection is known to be the dominant term. This was due to a flaw in the area of effect treatment in the RPI model. The unbounded nucleation site density allows the effective quenching area to exceed unity, yielding a nonsensical result. In fact, to evaluate the fractional boiling area, the actual number of bubbles on the heater surface, rather than the theoretical number of nucleation sites.

When the experimentally measured areas were input along with the boiling variables the result was better, but still did not accurately predict the heat flux partitioning. The evaporation term was over-predicted while the quenching term was under-predicted. This is due to the evaporation term double counting the contribution from the superheat layer surrounding the bubble.

5.3 Technical Contributions

1. A new pressurized flow boiling facility was created capable of conducting pressurize flow boiling tests up to 10 bar. The facility incorporates high-speed IR and high-speed video diagnostics, operated with the highest frame rate possible while capturing the full heater area. Advanced IR post-processing algorithms and techniques capable of quantifying a completed set of boiling variables were implemented. The facility also incorporates two safety systems enabling flow

boiling tests up to critical heat flux to be conducted safely.

2. An original database was generated for subcooled flow boiling. The database consists of a complete set of synchronized flow boiling data including 2-D surface temperature and heat flux distributions, along with measurements of nucleation site density, bubble period, growth time and wait time. This database is unique in that it is the only database to measure all the the requisite flow boiling parameters necessary to validate mechanistic heat flux partitioning models. The database was generated using the maximum frame rate and resolution possible with the IR camera technology. The database has already been used by several researchers to develop and validate mechanistic flow boiling models and can continue to be leveraged to inspire and validate future models and simulations.

3. This work presents the first complete experimental heat flux partitioning of subcooled flow boiling data at 1 and 2 bar pressure. The experimentally determined partitioned heat fluxes can serve as a benchmark for current and future mechanistic heat flux partioning models. Such models can use the boiling variables from the database as input for the governing equations of the model and compare the output of the model to directly measured partitioned heat fluxes.

4. Insights into the behavior and trends of the measured flow boiling variables were presented, including novel experimental insight into the saturation of the nucleation site density at high heat flux.

5.4 Suggested Future Work

5.4.1 Separate Effects Testing and Characterization of Nucleation Sites

The active nucleation site density has a significant role in the physics and mechanisms in boiling heat transfer as discussed in Section 3.3.3. Two separate heaters in identical

test conditions can yield significantly different results based on the surface properties of the heaters.

It has been shown that CHF can be controlled by engineering the boiling surface to control the porosity, wettability and surface roughness [62]. A similar study using engineered surfaces to control the cavity size distribution and density can be conducted to quantify the effects of the nucleation site density and morphology on boiling heat transfer. The nucleation sites could be engineered into a nano-smooth surface using a focused ion beam or another method of engineering cavities. Such a study could provide valuable insight as to how the nucleation site density can be accurately incorporated into mechanistic models for flow boiling heat transfer.

5.4.2 Fluorine Tin Oxide

The Indium Tin Oxide (ITO) heaters used in this work have a significant electrochemical reaction with water when a high voltage is used. The reaction caused an opaque film to form on the surface of the heater, the electrical resistance of the heater to increase, and a non-uniformity in the heat generation to occur. At atmospheric pressure and saturation temperature this reaction is slow and takes place over the course of a few hours of testing. However, at high-pressure and high-temperature conditions this reaction can occur within seconds. This issue was circumvented with the use of the polarity switching system, however, it is not an ideal solution.

Future work could incorporate a Fluoride Tin Oxide (FTO) film instead of an ITO film. FTO has been shown to be more chemically inert and resilient than ITO [63]. ITO also undergoes a phase change around 200 C [26], using FTO could enable higher temperature and pressure testing beyond the ITO phase change temperature.

5.4.3 Elongated Heater Testing

This work used a 1 cm by 1 cm heated area for conducting tests. Considering the characteristic size of a bubble at atmospheric pressure is 1-2 mm this heater does not provide a significant heated length for a study on the sliding and coalescence of

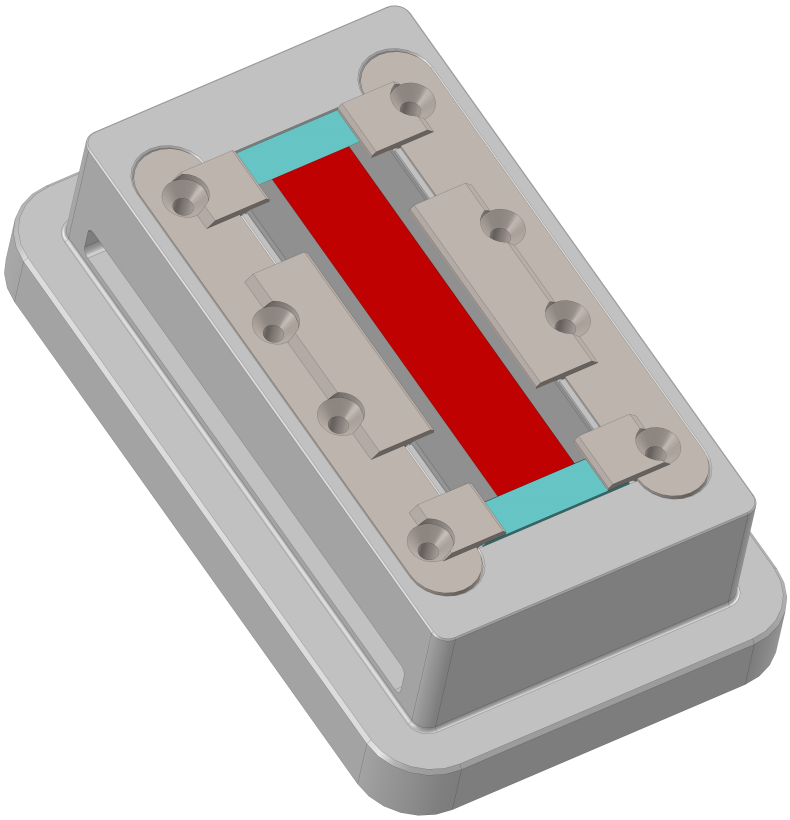

Figure 5-1: Elongated ITO-sapphire heater for tests with a longer heated length. Image Courtesy of Megan McCandless

bubbles. However, the heater cartridge designed for this work is capable of using heaters with a much longer heated area. Figure 5-1 shows a heater with a heated length five times greater than the one used in this work. This heater could be leveraged to explore the effect of the additional heated length, the coalescence of bubbles and the effect of sliding bubbles on the heat flux partitioning in subcooled flow boiling.

5.4.4 Next Generation Infrared Cameras

The IRC806HS camera used for this work was on the cutting edge of IR cameras just a few years ago when this work began. Since then, a new generation of high-speed cameras have been made available with improved specifications. Namely, the FLIR x6900 and the Telops Fast M3K are capable of achieving a higher-resolution and frame rate. This work was limited in the measurable parameters at 5 and 10 bar due to

insufficient spatial and temporal resolutions. Incorporation of new IR cameras, while expensive, can improve the quality of the data and increase the explorable regimes.

Bibliography

[1] Neil Todreas and Mujid Kazimi. *Nuclear Systems: Thermal Hydraulic Fundamentals*, volume 1. Taylor & Francis, 2 edition, 2012.

[2] Emilio Baglietto, Etienne Demarly, and Ravikishore Kommajosyula. Prediciting critical heat flux with multiphase cfd: 4 years in the making. In *Proceedings of the ASME Fluids Engineering Division Summer Meeting*, volume FEDSM2017. ASME, August 2017.

[3] Lindsey Gilman and Emilio Baglietto. A self-consistent, physics-based boiling heat transfer modeling framework for use in computational fluid dynamics. *International Journal of Multiphase Flow*, 95:35–53, October 2017.

[4] Takashi Hibiki and Mamoru Ishii. Active nucleation site density in boiling systems. *International Journal of Heat and Mass Transfer*, 46(14):2587–2601, July 2003.

[5] Robert Cole. A photographics study of pool boiling in the region of critical heat flux. *AIChE Journal*, 6(4):533–538, December 1960.

[6] T Mazzocco, W Ambrosini, R Kommajosyula, and E Baglietto. A reassessed model for mechanistic prediction of bubble departure and lift off diameters. *International Journal of Heat and Mass Transfer*, 117:119–124, February 2018.

[7] Novak Zuber. The dynamics of vapor bubbles in nonuniform temperature fields. *International Journal of Heat and Mass Transfer*, 2(1-2):83–98, March 1961.

[8] Matteo Bucci, Pierre Guenoun, and Emilio Baglietto. A mechanistic bubble waiting time model for nucleate boiilng. *Prepared for submission*, 2017.

[9] R. M. Podowski, D. A. Drew, R.T. Lahey, and M.Z. Podowski. A mechanistic model of the ebullition cycle in forced convection subcooled flow boiling. In *International topical meeting on nuclear reactor thermal-hydraulics*, number 8 in NURETH, pages 1535–1542, Tokyo, Japan, 1997.

[10] N Kurul and M Podowski. Multidimensional effects in forced convection subcooled boiling. In *Heat Transfer 1990: Proceedings of the Ninth International Heat Transfer Conference*, volume 2, pages 21–26, 1990.

[11] Nilanjana Basu, Gopinath Warrier, and Vijay Dhir. Wall heat flux partitioning during subcooled flow boiling: Part 1 - model development. *Journal of Heat Transfer*, 127:131–140, February 2005.

[12] Bren Phillips. *Experimental Investigation of Subcooled Flow Boiling Using Synchronized High Speed Video, Infrared Thermography, and Particle Imaging Velocimetry*. PhD thesis, Massachusetts Institute of Technology, 2014.

[13] Rosie Sugrue and Jacopo Buongiorno. A modified force-balance model for predicting bubble departure diameter in subcooled flow boiling. In *NURETH-15*, Pisa, Italy, May 2013.

[14] R. L. Judd and K. S. Hwang. A comprehensive model for nucleate pool boiling heat transfer including micro-layer evaporation. *Journal of Heat Transfer*, 98(4):623–629, 1976.

[15] Victor Del Valle and D Kenning. Subcooled flow boiling at high heat flux. *International Journal of Heat and Mass Transfer*, 1985.

[16] Gopinath Warrier and Vijay Dhir. Heat transfer and wall heat flux partitioning during subcooled flow nucleate boiling-a review. *Journal of Heat Transfer*, 2006.

[17] Matteo Bucci, Andrew Richenderfer, Guanyu Su, Thomas McKrell, and Jacopo Buongiorno. A mechanistic ir calibration technique for boiling heat transfer investigations. *International Journal of Multiphase Flow*, 83:115–127, 2016.

[18] Tae Hoon Kim, Eric Kommer, Serguei Dessiatoun, and Jungho Kim. Measurement of two-phase flow and heat transfer parameters using infrared thermometry. *International Journal of Multiphase Flow*, 40:56–67, 2012.

[19] W.H. Jens and P.A. Lottes. Analysis of heat transfer, burnout, pressure drop and density data for high-pressure water. techreport 4627, Argonne National Laboratory, May 1951.

[20] J. Thom. Prediction of pressure loss during forced ciriculation boiling of water. *International Journal of Heat and Mass Transfer*, 7:709, 1964.

[21] J Sgheiza and J Myers. Behavior of nucleation sites in pool boiling. *AlChE Journal*, 1985.

[22] T Theofanous, J Tu, A Dinh, and T Dinh. The boiling crisis phenomenon part i: nucleation and nucleate boiling heat transfer. *Experimental Thermal and Fluid Science*, 26:775–792, 2002.

[23] T Theofanous, T Dinh, J Tu, and A Dinh. The boiling crisis phenomenon part iil dryout dynamics and burnout. *Experimental Thermal and Fluid Sciences*, 26:793–810, 2002.

[24] I Golobic, J Petkovsek, M Baselj, A Papez, and D Kenning. Experimental determination of transient wall temperature distributions close to growing vapor bubbles. *Heat and Mass Transfer*, 2009.

[25] Craig Gerardi, Jacopo Buongiorno, Lin wen Hu, and Thomas McKrell. Infrared thermometry study of nanofluid pool boiling. *Nanoscale Research Letter*, 2011.

[26] Craig Gerardi. *Investigation of the pool boiling heat transfer enhancement of nano-engineered fluids by means of high-speed infrared thermometry.* PhD thesis, Massachusetts Institute of Technology, 2009.

[27] Enno Wagner and Peter Stephan. High-resolution measurements at nucleate boiling of pure fc-84 and fc-3284 and its binary mixtures. *Journal of Heat Transfer*, 131, 2009.

[28] J Jung, S Kim, and J Kim. Observations of the critical heat flux process during pool boiling of fc-72. *Journal of Heat Transfer*, 136, 2014.

[29] Satbyoul Jung and Hyungdae Kim. An experimental study on heat transfer mechanisms in the microlayer using integrated total reflection, laser interferometry and infrared thermometry technique. *Heat Transfer Engineering*, 36(12):1002–1012, 2015.

[30] Guan-Yu Su, Matteo Bucci, Thomas McKrell, and Jacopo Buongiorno. Transient boiling of water under exponentially escalating heat inputs. part i: Pool boiling. *International Journal of Heat and Mass Transfer*, 96:667–684, May 2016.

[31] Guan-Yu Su, Matteo Bucci, Thomas McKrell, and Jacopo Buongiorno. Transient boiling of water under exponentially escalating heat inputs. part ii: Flow boiling. *International Journal of Heat and Mass Transfer*, 96:685–698, 2016.

[32] Gregory L. DeWitt. *Investigation of downward facing critical heat flux with water-based nanofluids for In-Vessel Retention applications.* PhD thesis, Massachusetts Institute of Technology, 2011.

[33] Grundfos. *CR, CRI, CRN 1s, 1, 3, 5 , 10, 15, 20, CR, CRN 32, 45, 64, 90, 120, 150 High temperature (air-cooled top) Installation and Operating Instructions*, 2016.

[34] Eric C. Forrest. *Study of turbulent single-phase heat transfer and onset of nucleate boiling in high aspect ratio mini-channels to support the MITR LEU conversion.* PhD thesis, Massachusetts Institute of Technology, 2014.

[35] Flexicraft Industries, Flexicraft Industries, 2315 West Hubbard St, Chicago, IL 60612. *Hydropad Installation, Operationa and Maintenance.*

[36] Flexicraft, Flexicraft Industries, 2315 West Hubbard St, Chicago, IL 60612. *Hydropad Application & Design Guide.*

[37] Swagelok, www.swagelok.com. *Gaugeable Tube Fittings and Adapter Fittings*, revu edition, November 2017.

[38] PermSelect - MedArray, Inc., MedArray, Inc. 3915 Research Park Dr., Suit A-4 Ann Arbor, MI 48108, USA. *PDMSXA-1.0 Data Sheet*.

[39] Omega, One Omega Driver, Box 4047 Stamford, CT 06907-0047. *Series FTB-1400 Turbine Flow Meter User's Guide*.

[40] McMaster-Carr. High-temperature high-purity silicone o-ring. Internet Website, November 2017.

[41] Warren C Young and Richard G Budynas. *Roark's Formulas for Stress and Strain*. McGraw-Hill, 2002.

[42] Precision Ceramics. Shapal hi-m soft. Internet, www.precision-ceramics.com, November 2017.

[43] Radion Mogilevsky, Liudmila G. Sharafutdinova, and Scott D. Mittl. Optical properties of sapphire. *Proceedings of SPIE - The International Society for Optical Engineering*, 7056:6–, 08 2008.

[44] Ferro-Ceramic Grinding Inc. Sapphire properties. Internet.

[45] Diamond Coatings, Diamond Coatings Inc., 4830 S. 39th Street, Phoenix, AZ 85040. *Diamond Indium Tin Oxide (ITO) Datasheet*.

[46] Bren Andrew Phillips. Nano-engineering the boiling surface for optimal heat transfer rate and critical heat flux. Master's thesis, Massachusetts Institute of Technology, February 2011.

[47] IRCameras, LLC. *IRC800 Liquid Nitrogen Cooled Infrared Camera User's Guide*, 1.0 edition, May 2013.

[48] IRCameras. *DOC, OPERATING MANUAL, WINIRC*, nc edition, 2011.

[49] Vision Research, 100 Dey Road Wayne, NJ 07470 USA. *Phantom v12.1 Data Sheet*, June 2012.

[50] Vision Research. Phantom v-series family of digital high-speed cameras. Internet, June 2012.

[51] CHROMA Systems Solutions, Inc., 19772 Pauling, Foothill Ranch, CA 92610. *Programmable DC Power Supply Model 62000P Series*, May 2017.

[52] RIGOL Technologies, Inc. *DG1000 Series Dual-Channel Function/Arbitrary Waveform Generator*, December 2014.

[53] John G. Collier and John R. Thome. *Convective Boiling and Condensation*. Oxford Engineering Science Series. Oxford Science Publications, third edition, 2001.

[54] Takashi Sato and Hirohisa Matsumura. On the conditions of incipient subcooled-boiling with forced convection. *Bulletin of JSME*, 7(26), 1964.

[55] S Kandlikar. Heat transfer characteristics in partial boiling, fully developed boiling, and significant void flow regions of subcooled flow boiling. *Journal of Heat Transfer*, 120:395–401, May 1998.

[56] Jee H Seong and Matteo Bucci. Method for determining active nucleation site density for ir thermometry experiments. 2017.

[57] D.C. Groeneveld, J Shan, A Vasic, L Leung, A Durmayaz, J Yang, S Cheng, and A Tanase. The 2006 chf look-up table. *Nuclear Engineering and Design*, 237(15-17):1909–1922, September 2007.

[58] Pierre Guenoun, Etienne Demarly, Matteo Bucci, and Emilio Baglietto. A fully mechanstic approach for prediction of bubble wait time in flow boiling heat transfer. *Prepared for submission*, 2017.

[59] Y Hsu. On the size range of active nucleation cavities on a heating surface. *Journal of Heat Transfer*, 84(3):207–213, August 1962.

[60] Andrew Richenderfer, Artyom Kossolapov, Jee Hyun Seong, Giacomo Saccone, Etienne Demarly, Ravikishore Kommajosyula, Emilio Baglietto, Jacopo Buongiorno, and Matteo Bucci. Investigation of subcooled flow boiling and chf using high-resolution diagnostics. *In preparation for submission*, 2018.

[61] Omega Engineering, https://www.omega.com/pressure/pdf/PX309.pdf. *All Stainless Steel Transducer/Transmitter Multimedia Compatibility.*

[62] Melanie Tetreault-Friend, Reza Azizian, Matteo Bucci, Thomas McKrell, Jacopo Buongiorno, Michael Rubner, and Robert Cohen. Critical heat flux maxima resulting from the controlled morphology of nanoporous hydrophilic surface layers. *Applied Physics Letters*, 108(24), June 2016.

[63] M Aouaj, Rosy Diaz, Azzam Belayachi, F Rueda, and M Abd-Ledfil. Comparative study of ito and fto thin films grown by spray pyrolysis. *Materials Research Bulletin*, 44:1458–1461, 2009.

Appendix A

Boiling Curves and Nucleation Site Density Data

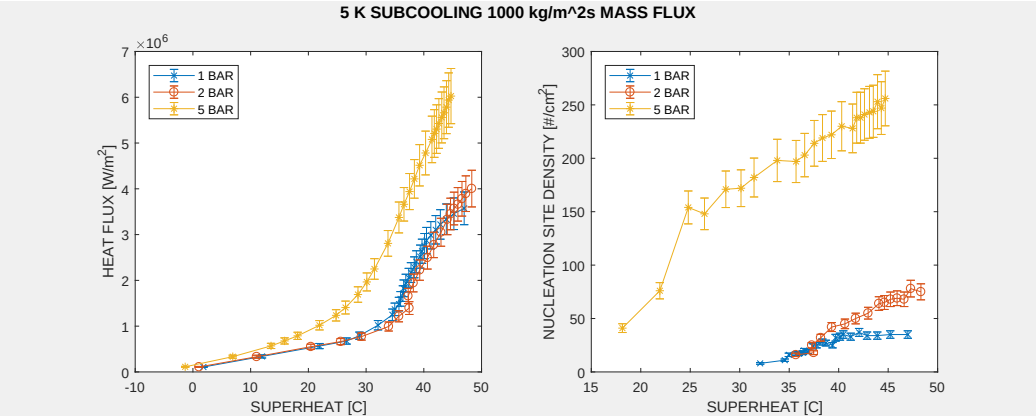

Figure A-1: Boiling curve and nucleation site density for 5 K, 1000 $\frac{kg}{m^2 s}$ all pressures.

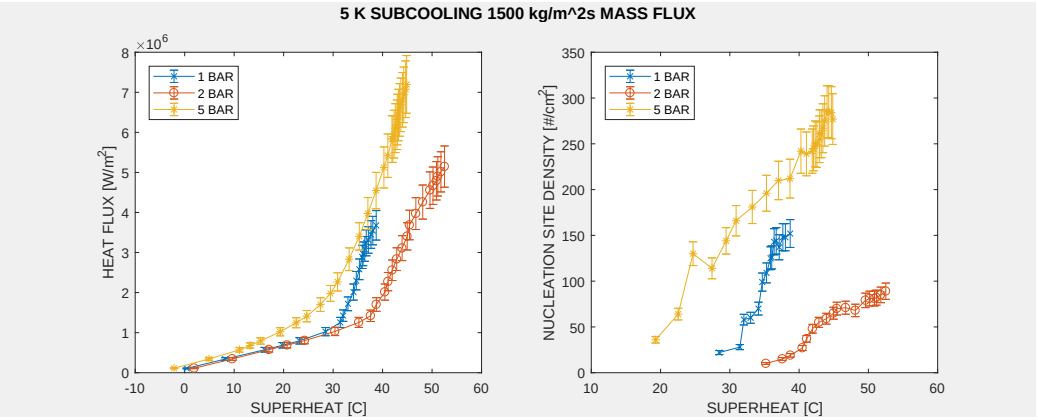

Figure A-2: Boiling curve and nucleation site density for 5 K, 1500 $\frac{kg}{m^2 s}$ all pressures.

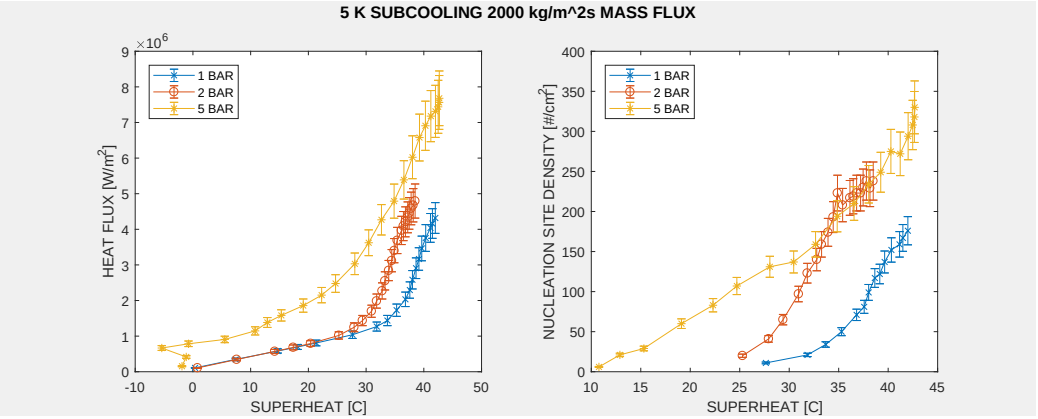

Figure A-3: Boiling curve and nucleation site density for 5 K, 2000 $\frac{kg}{m^2 s}$ all pressures.

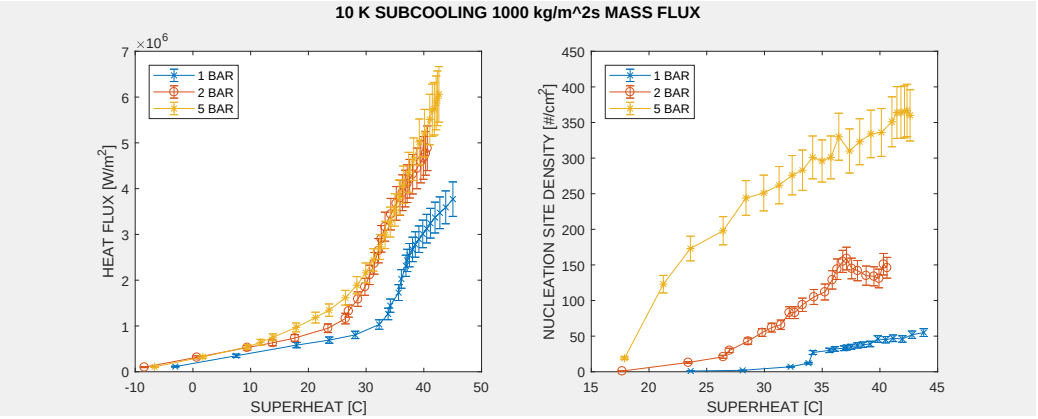

Figure A-4: Boiling curve and nucleation site density for 10 K, 1000 $\frac{kg}{m^2 s}$ all pressures.

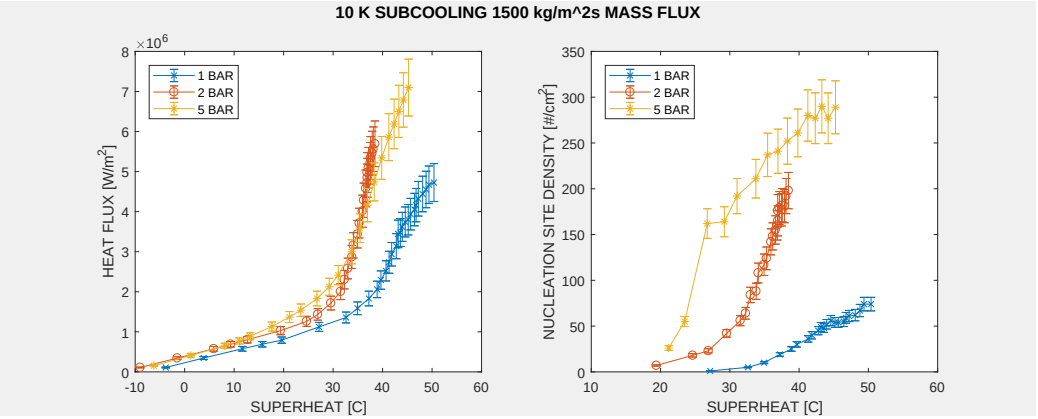

Figure A-5: Boiling curve and nucleation site density for 10 K, 1500 $\frac{kg}{m^2 s}$ all pressures.

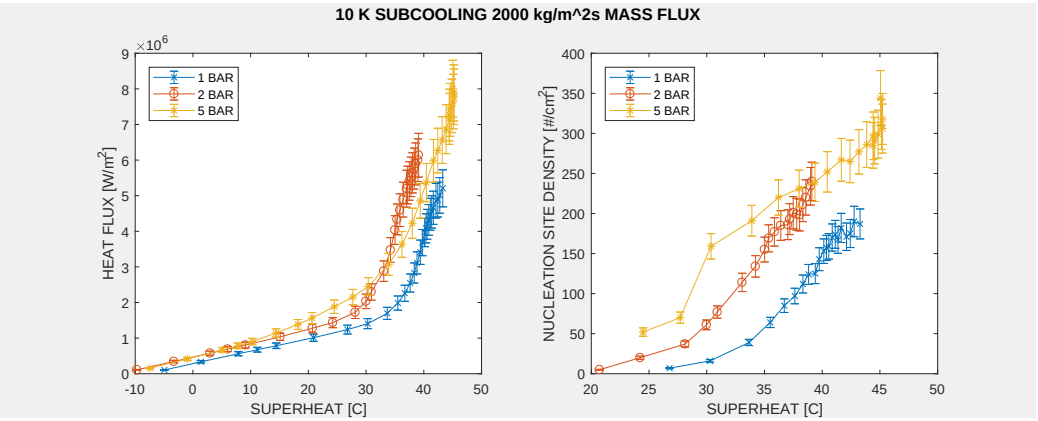

Figure A-6: Boiling curve and nucleation site density for 10 K, 2000 $\frac{kg}{m^2 s}$ all pressures.

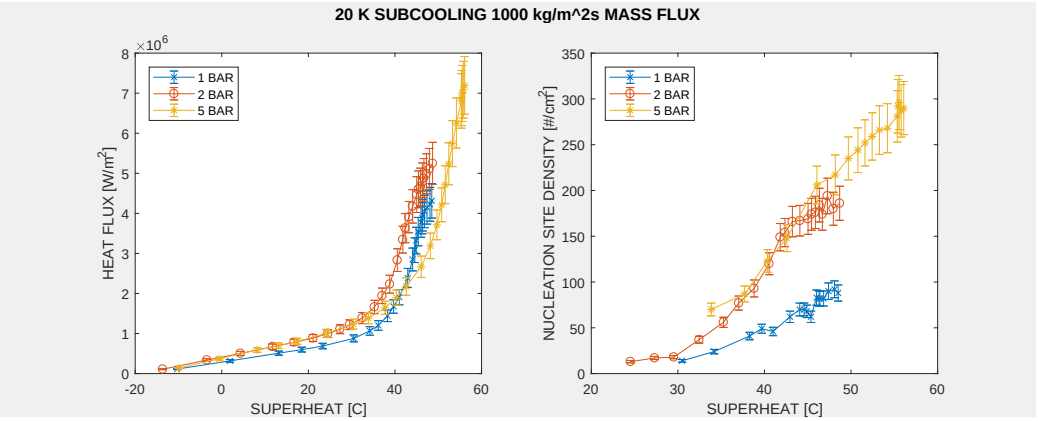

Figure A-7: Boiling curve and nucleation site density for 20 K, 1000 $\frac{kg}{m^2 s}$ all pressures.

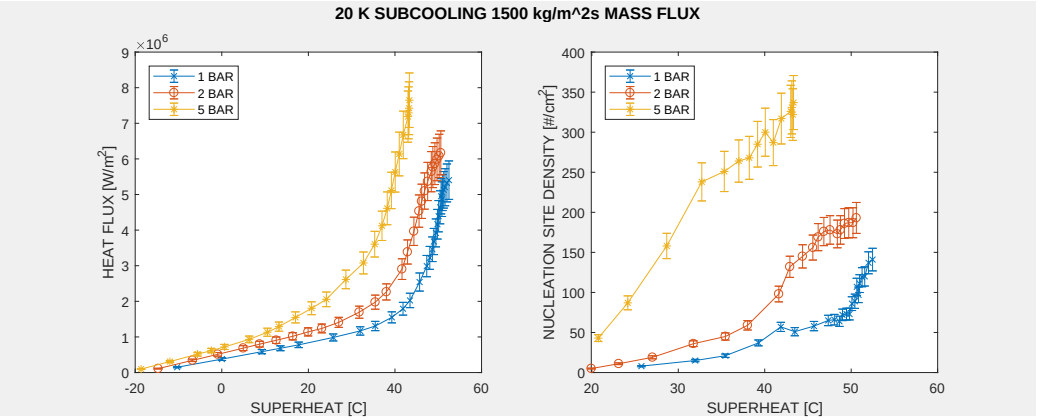

Figure A-8: Boiling curve and nucleation site density for 20 K, 1500 $\frac{kg}{m^2 s}$ all pressures.

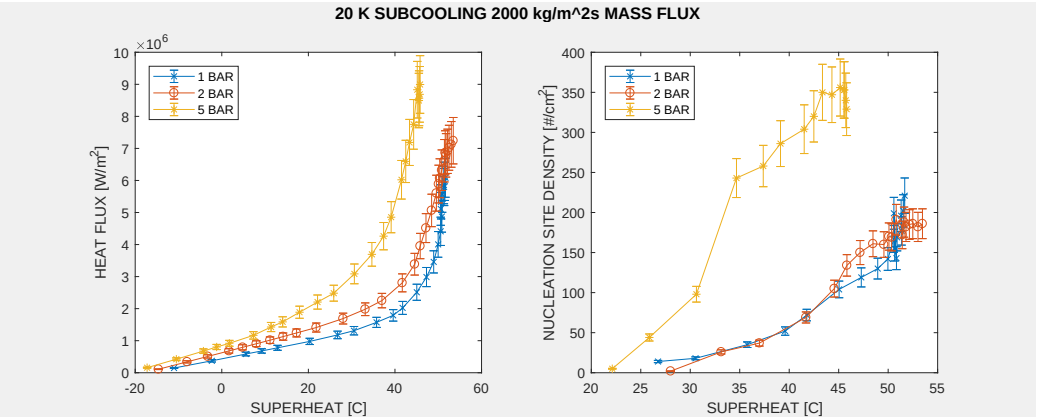

Figure A-9: Boiling curve and nucleation site density for 20 K, 2000 $\frac{kg}{m^2 s}$ all pressures.

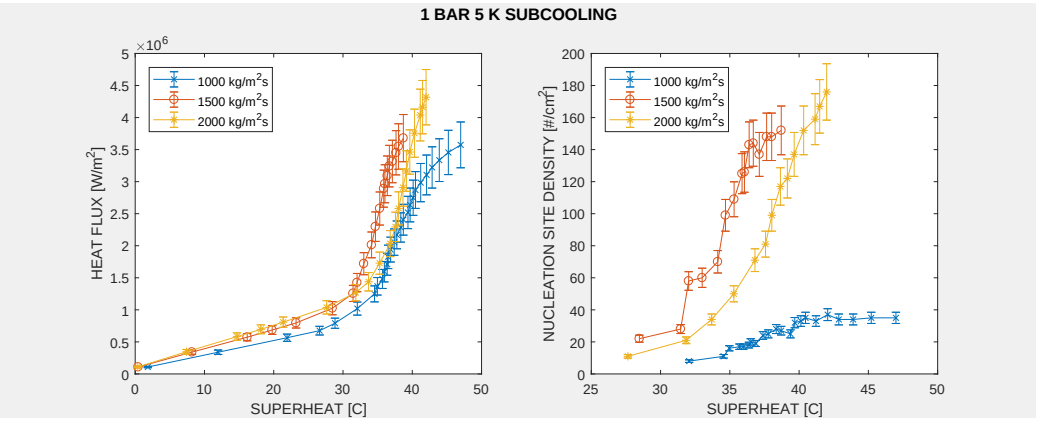

Figure A-10: Boiling curve and nucleation site density for 1 bar, 5 K all mass fluxes.

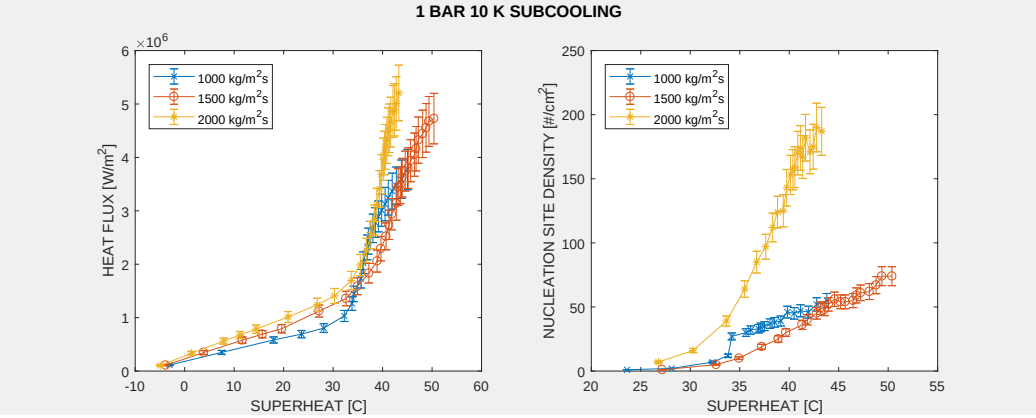

Figure A-11: Boiling curve and nucleation site density for 1 bar, 10 K all mass fluxes.

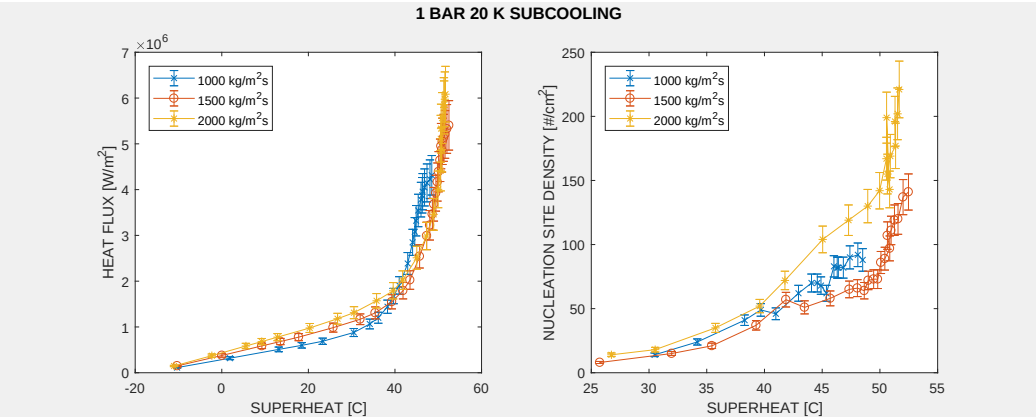

Figure A-12: Boiling curve and nucleation site density for 1 bar, 20 K all mass fluxes.

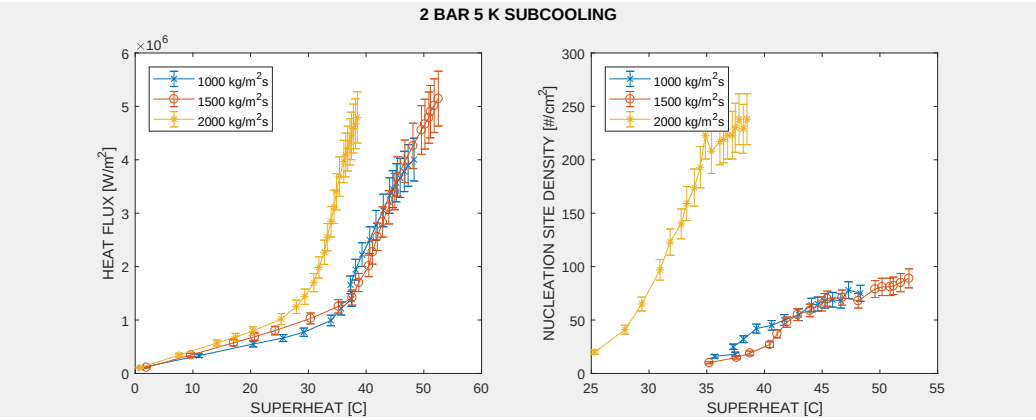

Figure A-13: Boiling curve and nucleation site density for 2 bar, 5 K all mass fluxes.

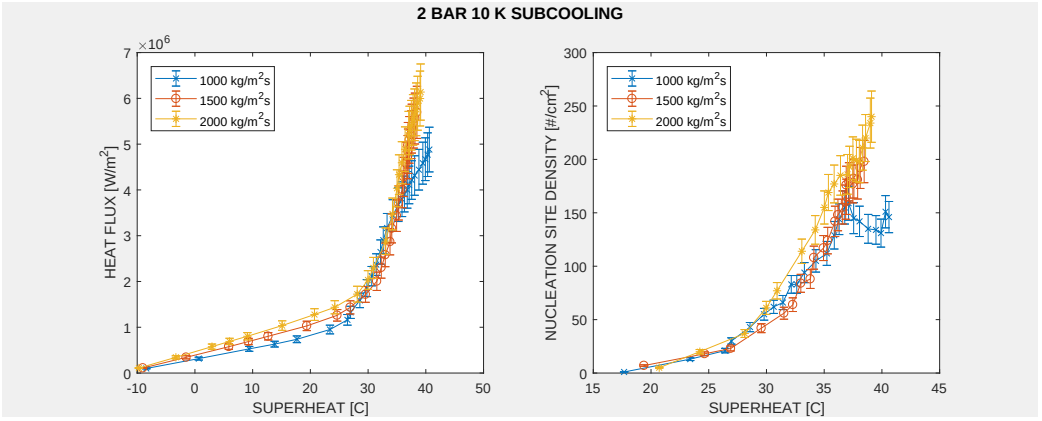

Figure A-14: Boiling curve and nucleation site density for 2 bar, 10 K all mass fluxes.

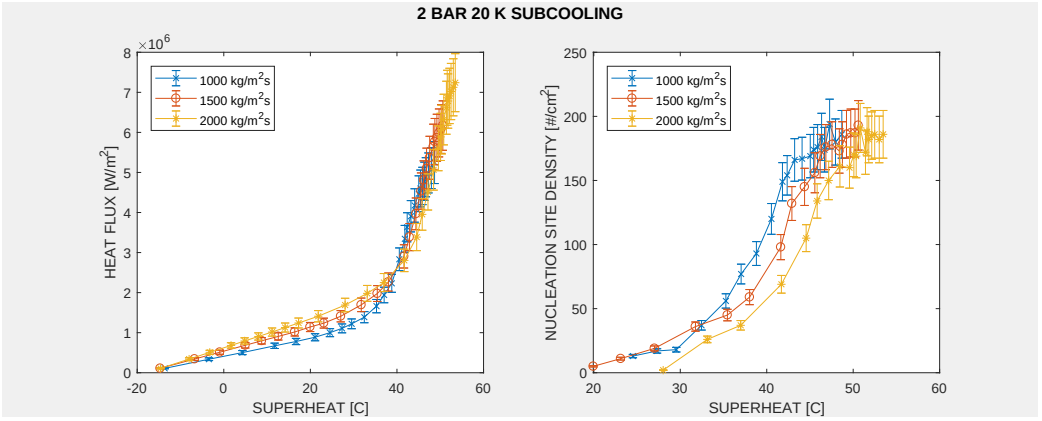

Figure A-15: Boiling curve and nucleation site density for 2 bar, 20 K all mass fluxes.

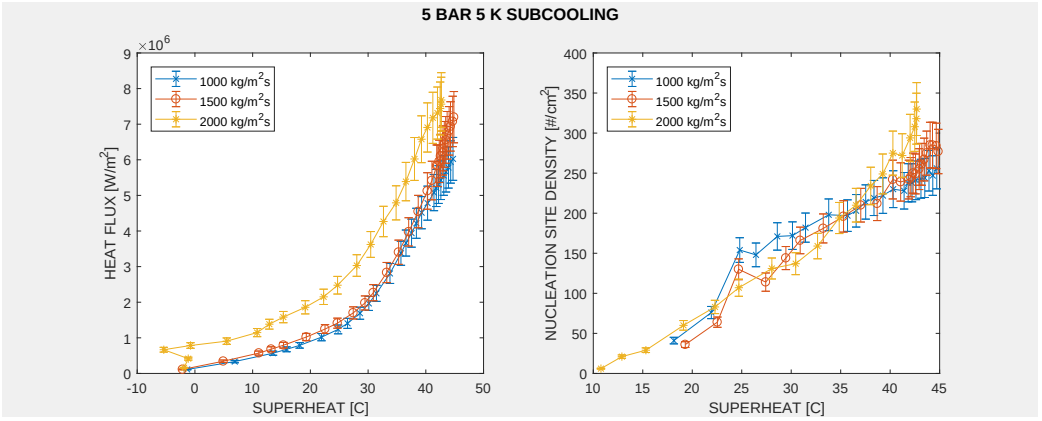

Figure A-16: Boiling curve and nucleation site density for 5 bar, 5 K all mass fluxes.

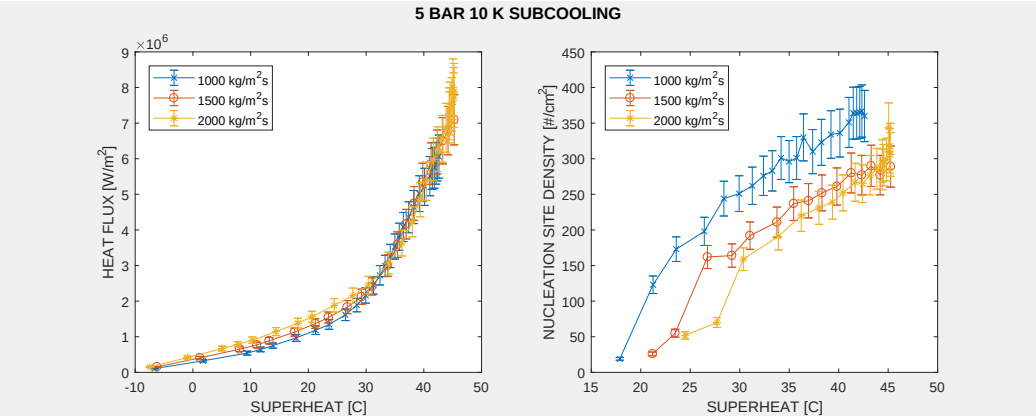

Figure A-17: Boiling curve and nucleation site density for 5 bar, 10 K all mass fluxes.

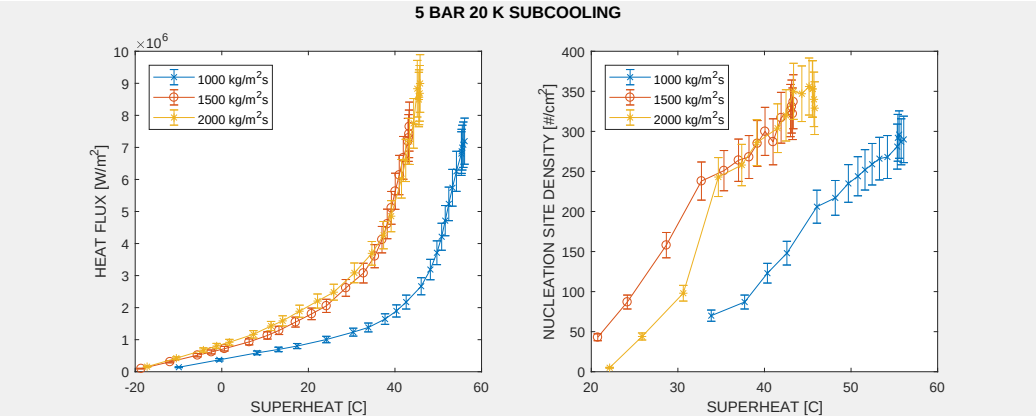

Figure A-18: Boiling curve and nucleation site density for 5 bar, 20 K all mass fluxes.

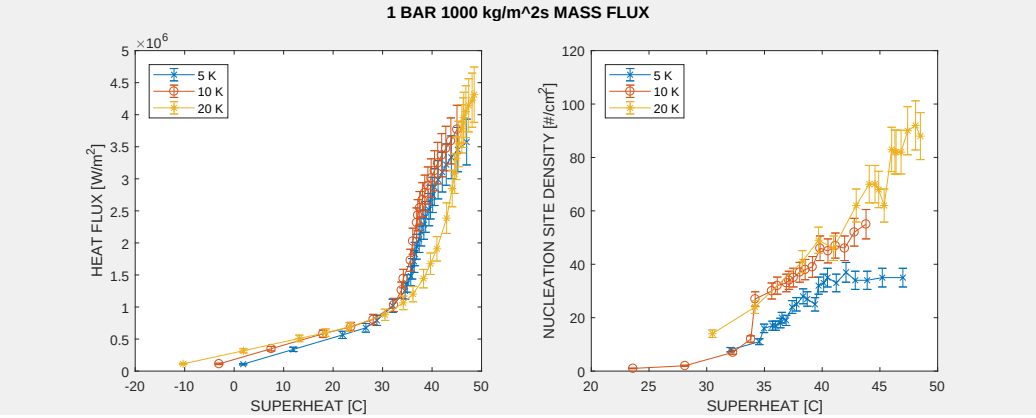

Figure A-19: Boiling curve and nucleation site density for 1 bar, 1000 $\frac{kg}{m^2 s}$ all subcoolings.

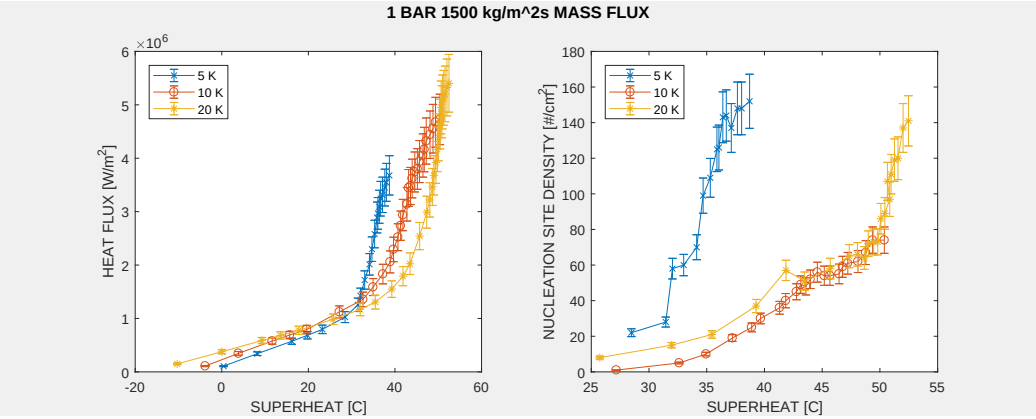

Figure A-20: Boiling curve and nucleation site density for 1 bar, 1500 $\frac{kg}{m^2 s}$ all subcoolings.

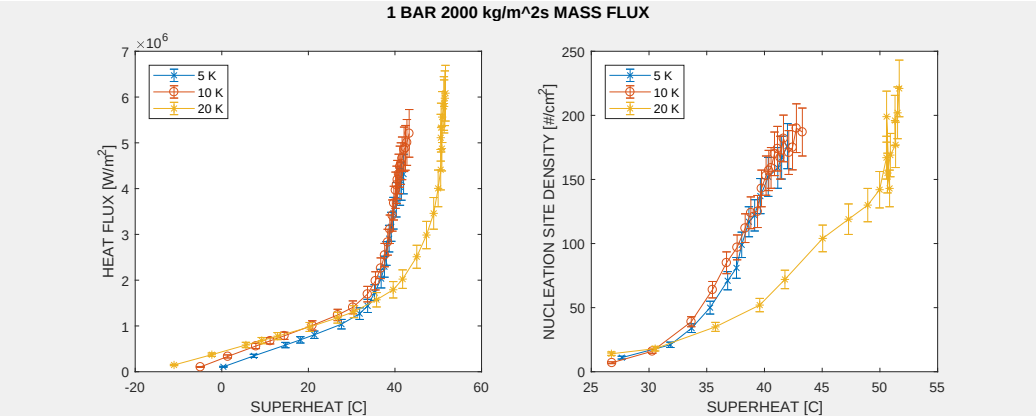

Figure A-21: Boiling curve and nucleation site density for 1 bar, 2000 $\frac{kg}{m^2 s}$ all subcoolings.

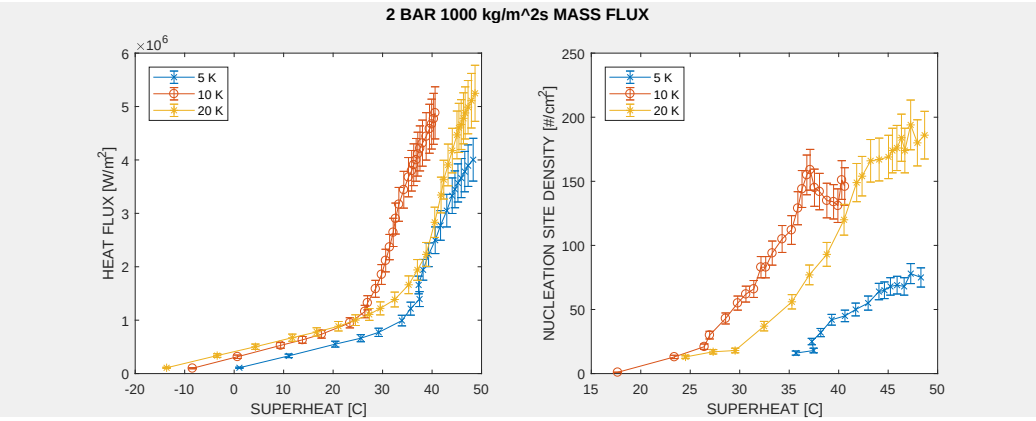

Figure A-22: Boiling curve and nucleation site density for 2 bar, 1000 $\frac{kg}{m^2 s}$ all subcoolings.

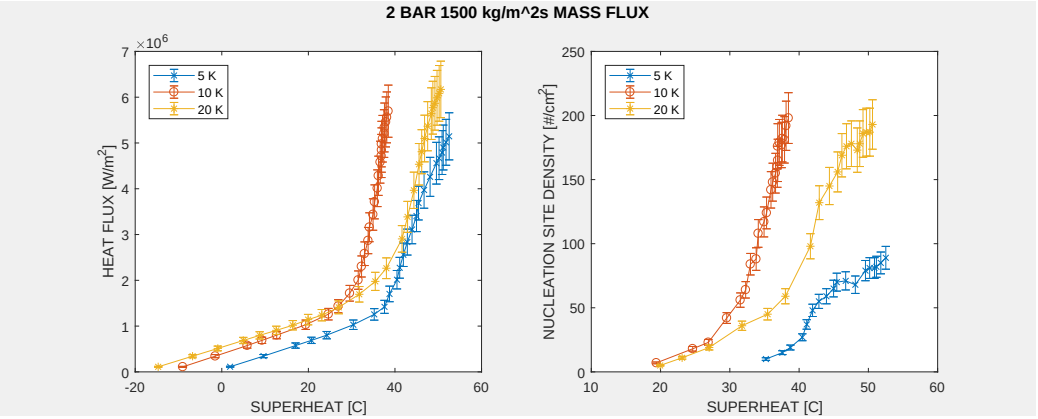

Figure A-23: Boiling curve and nucleation site density for 2 bar, 1500 $\frac{kg}{m^2 s}$ all subcoolings.

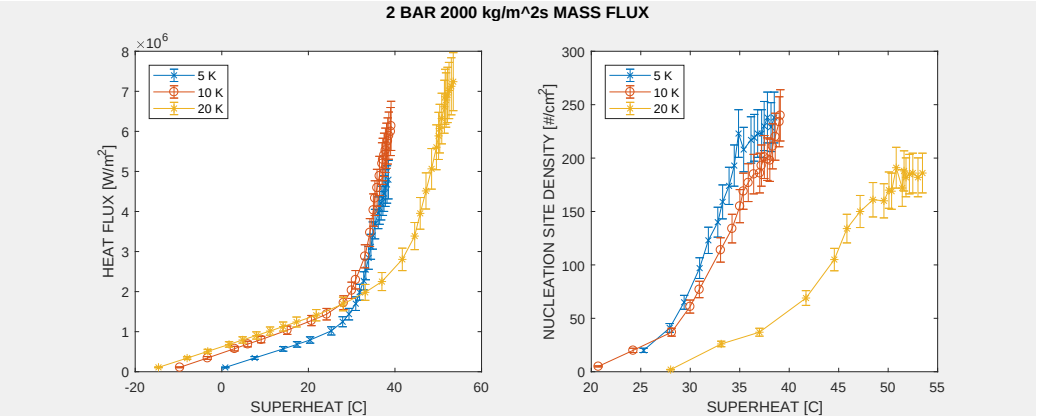

Figure A-24: Boiling curve and nucleation site density for 2 bar, 2000 $\frac{kg}{m^2 s}$ all subcoolings.

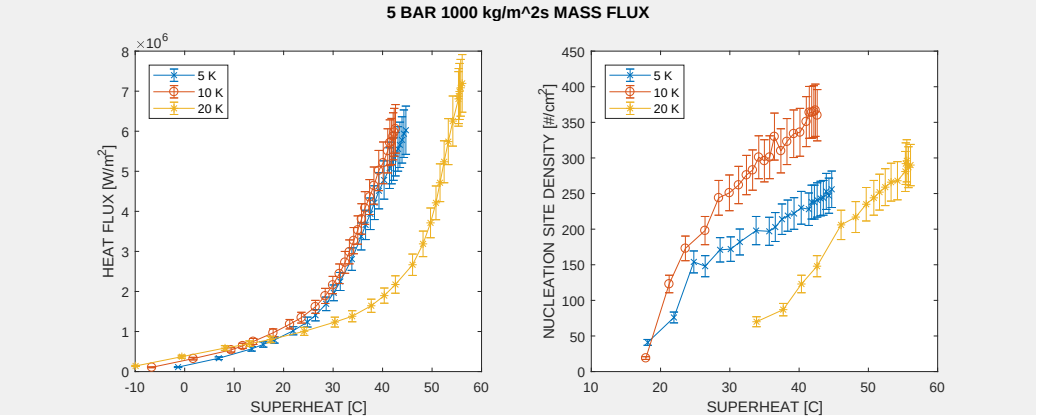

Figure A-25: Boiling curve and nucleation site density for 5 bar, 1000 $\frac{kg}{m^2 s}$ all subcoolings.

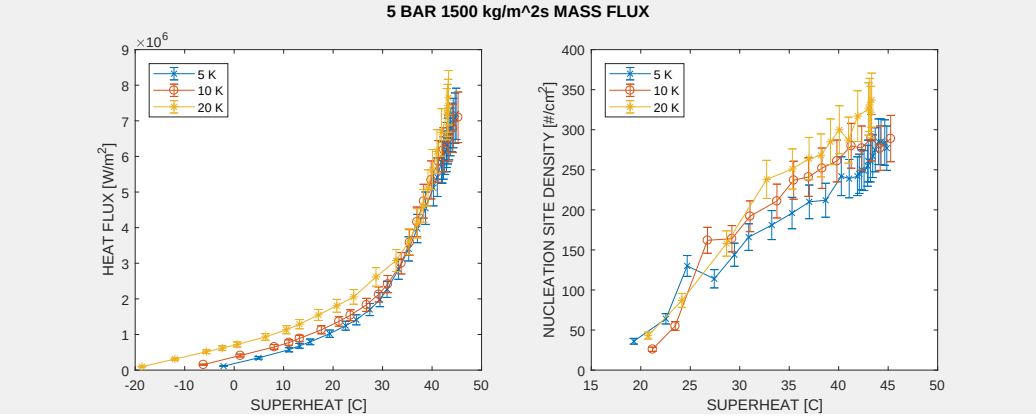

Figure A-26: Boiling curve and nucleation site density for 5 bar, 1500 $\frac{kg}{m^2 s}$ all subcoolings.

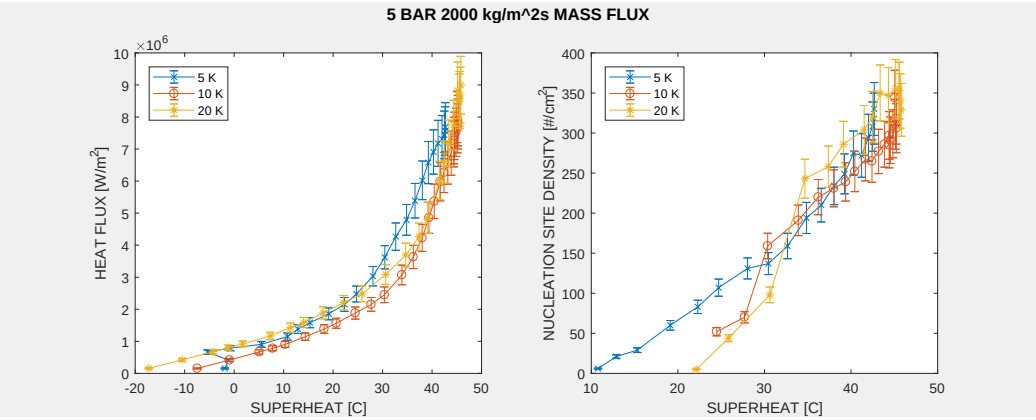

Figure A-27: Boiling curve and nucleation site density for 5 bar, 2000 $\frac{kg}{m^2 s}$ all subcoolings.

Appendix B

Heat Transfer Coefficient and Nucleation Site Density

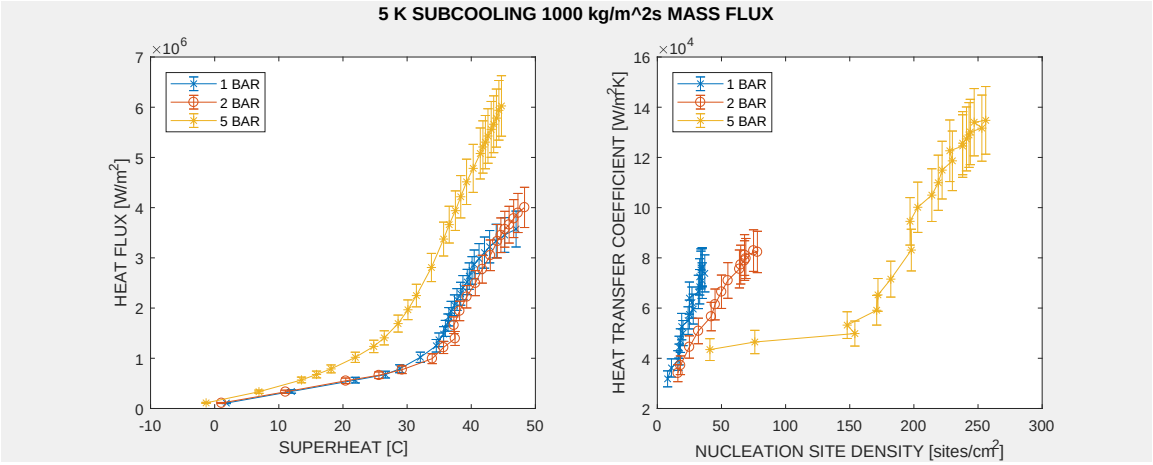

Figure B-1: Boiling Curves (left), Heat Transfer Coefficient versus Nucleation Site Density (right) for 5 K, 1000 $\frac{kg}{m^2 s}$, 1 and 2 bar.

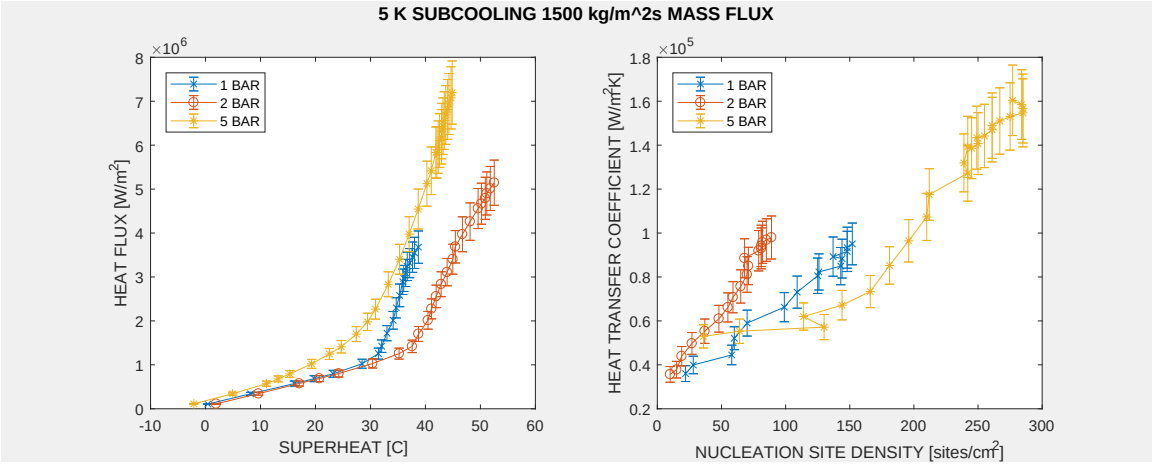

Figure B-2: Boiling Curves (left), Heat Transfer Coefficient versus Nucleation Site Density (right) for 5 K, 1500 $\frac{kg}{m^2 s}$, 1 and 2 bar.

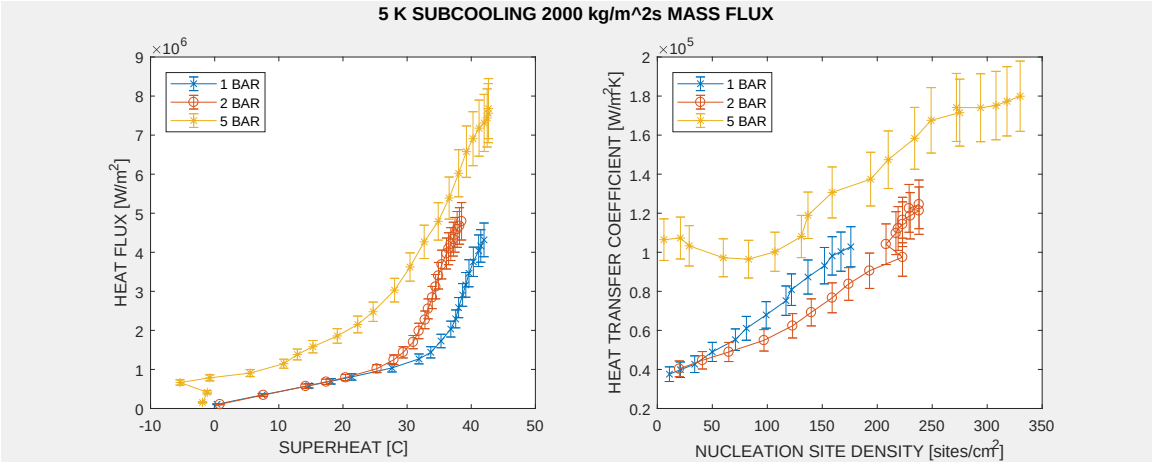

Figure B-3: Boiling Curves (left), Heat Transfer Coefficient versus Nucleation Site Density (right) for 5 K, 2000 $\frac{kg}{m^2 s}$, 1 and 2 bar.

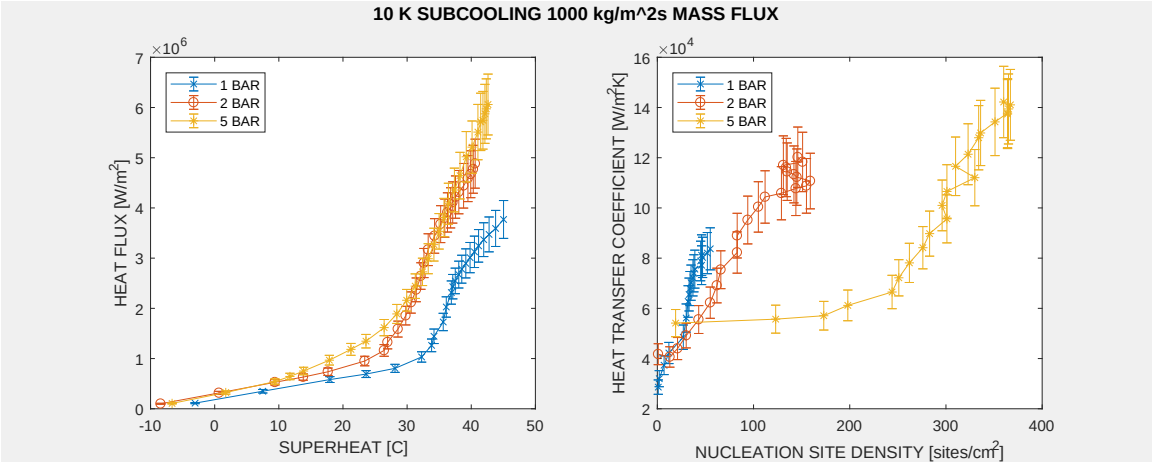

Figure B-4: Boiling Curves (left), Heat Transfer Coefficient versus Nucleation Site Density (right) for 10 K, 1000 $\frac{kg}{m^2 s}$, 1 and 2 bar.

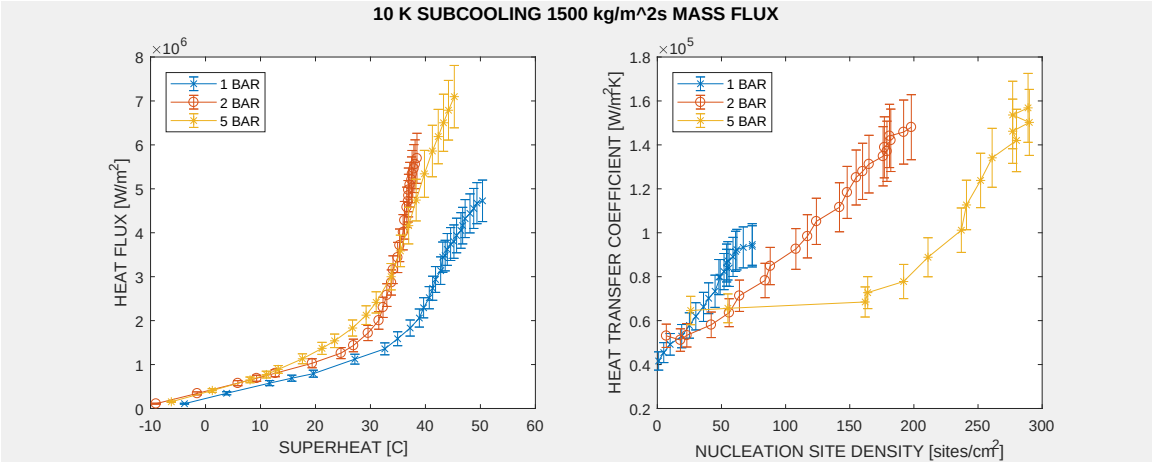

Figure B-5: Boiling Curves (left), Heat Transfer Coefficient versus Nucleation Site Density (right) for 10 K, 1500 $\frac{kg}{m^2 s}$, 1 and 2 bar.

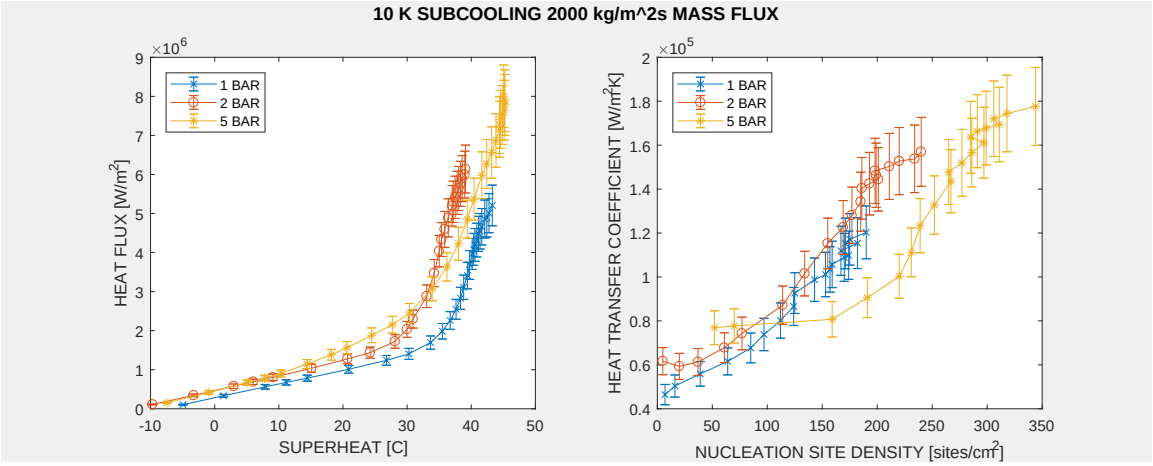

Figure B-6: Boiling Curves (left), Heat Transfer Coefficient versus Nucleation Site Density (right) for 10 K, 2000 $\frac{kg}{m^2 s}$, 1 and 2 bar.

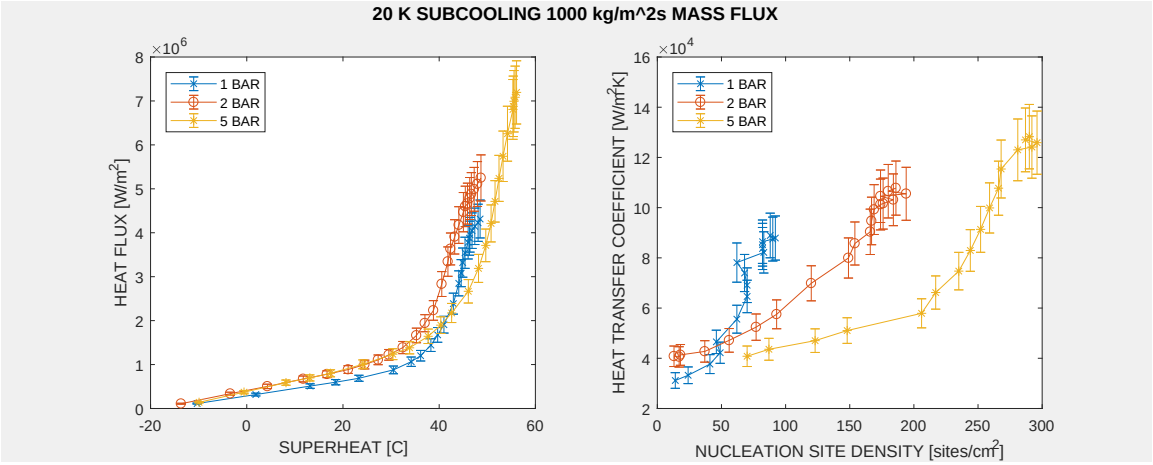

Figure B-7: Boiling Curves (left), Heat Transfer Coefficient versus Nucleation Site Density (right) for 20 K, 1000 $\frac{kg}{m^2 s}$, 1 and 2 bar.

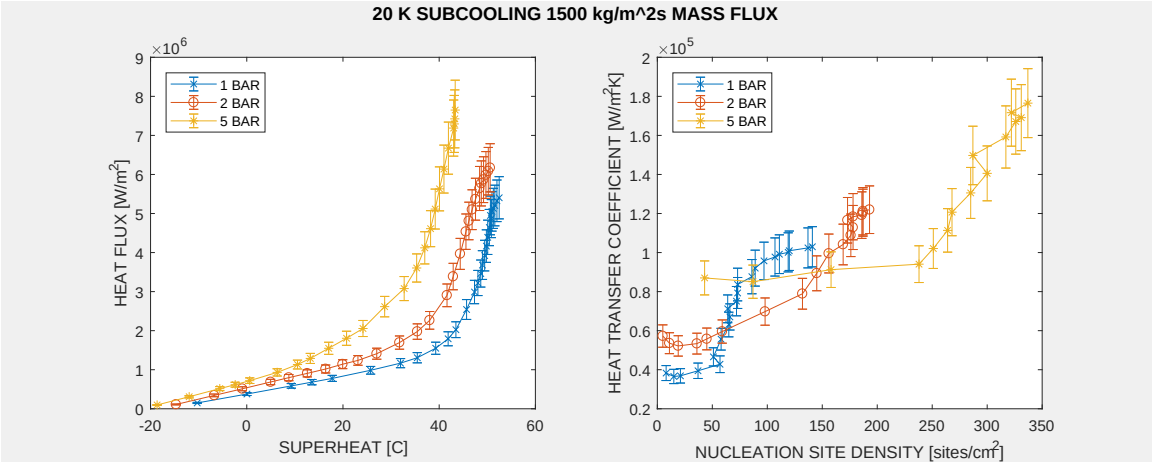

Figure B-8: Boiling Curves (left), Heat Transfer Coefficient versus Nucleation Site Density (right) for 20 K, 1500 $\frac{kg}{m^2 s}$, 1 and 2 bar.

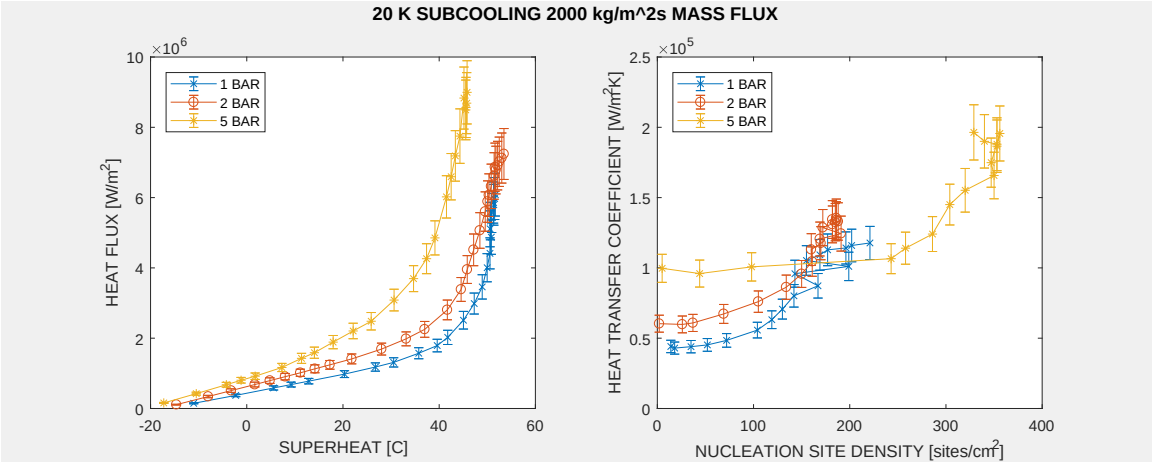

Figure B-9: Boiling Curves (left), Heat Transfer Coefficient versus Nucleation Site Density (right) for 20 K, 2000 $\frac{kg}{m^2 s}$, 1 and 2 bar.

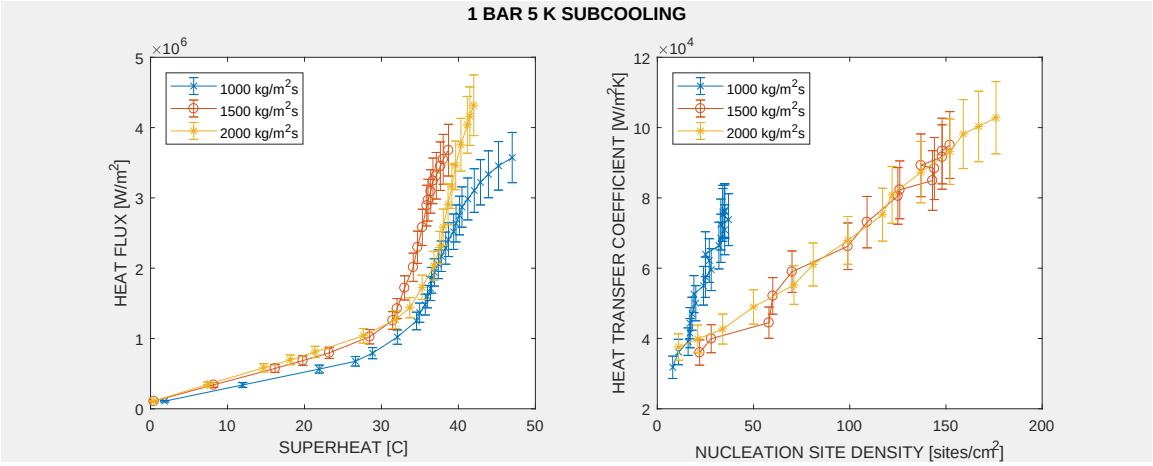

Figure B-10: Boiling Curves (left), Heat Transfer Coefficient versus Nucleation Site Density (right) for 1 bar, 5 K all mass fluxes.

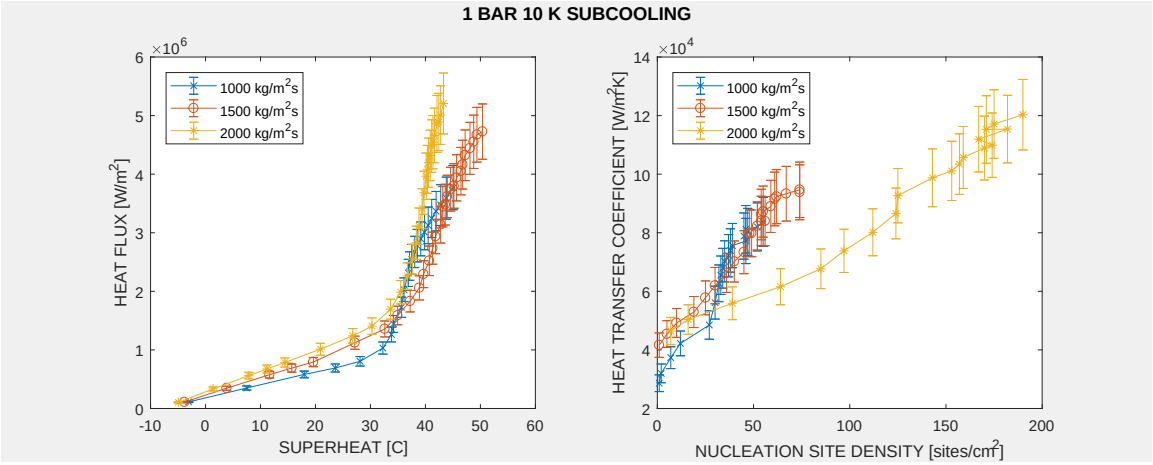

Figure B-11: Boiling Curves (left), Heat Transfer Coefficient versus Nucleation Site Density (right) for 1 bar, 10 K all mass fluxes.

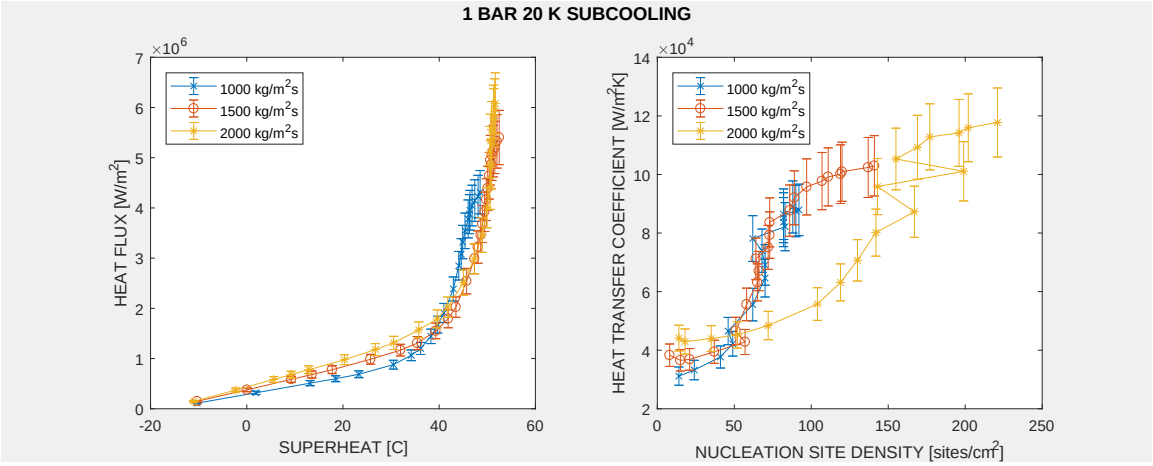

Figure B-12: Boiling Curves (left), Heat Transfer Coefficient versus Nucleation Site Density (right) for 1 bar, 20 K all mass fluxes.

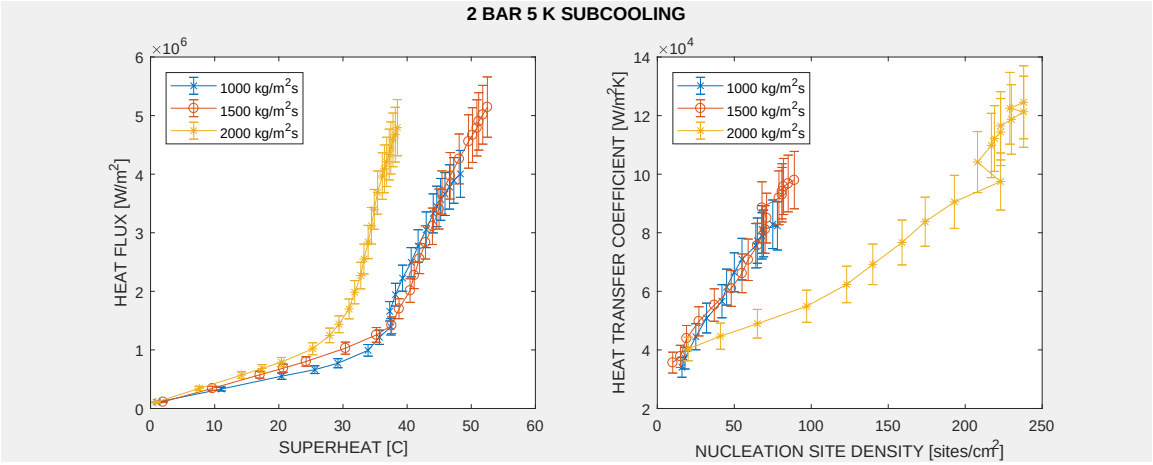

Figure B-13: Boiling Curves (left), Heat Transfer Coefficient versus Nucleation Site Density (right) for 2 bar, 5 K all mass fluxes.

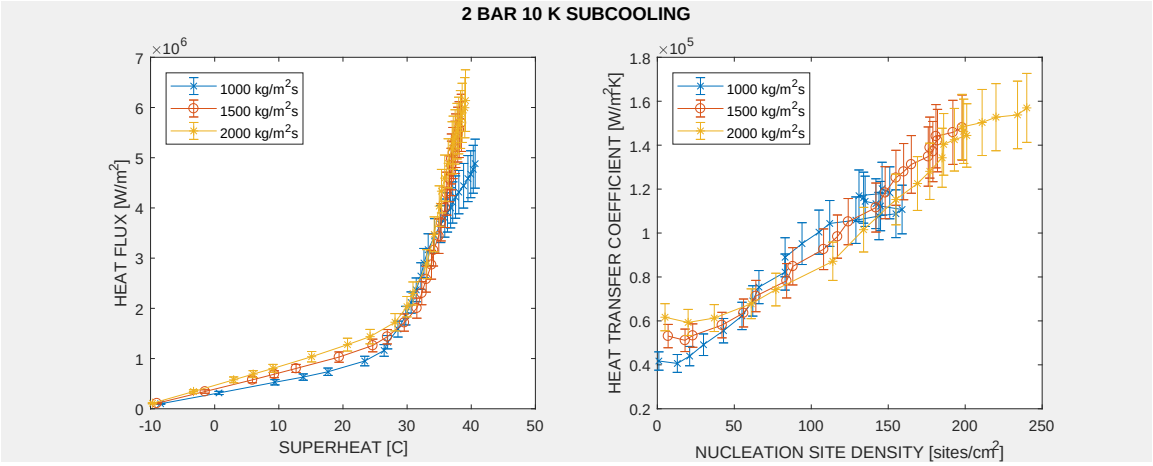

Figure B-14: Boiling Curves (left), Heat Transfer Coefficient versus Nucleation Site Density (right) for 2 bar, 10 K all mass fluxes.

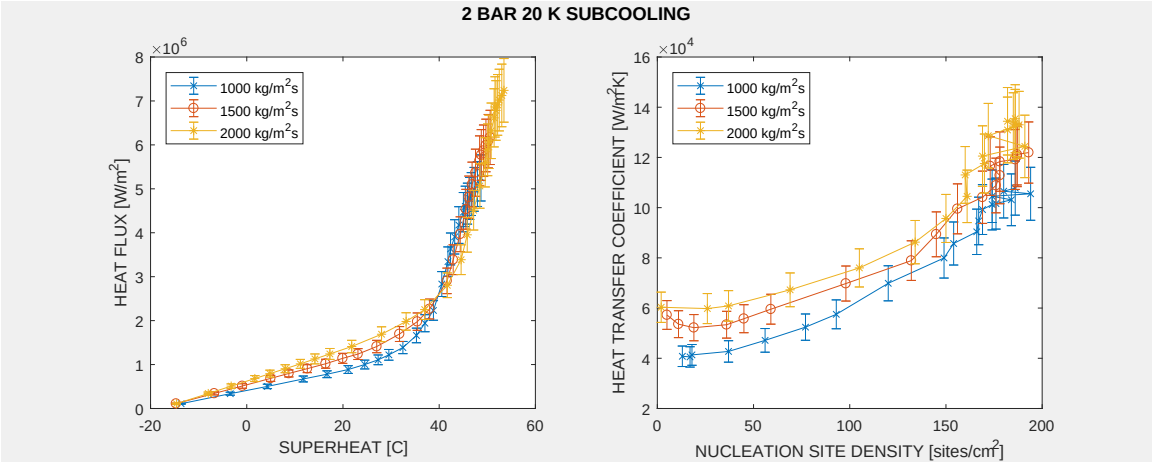

Figure B-15: Boiling Curves (left), Heat Transfer Coefficient versus Nucleation Site Density (right) for 2 bar, 20 K all mass fluxes.

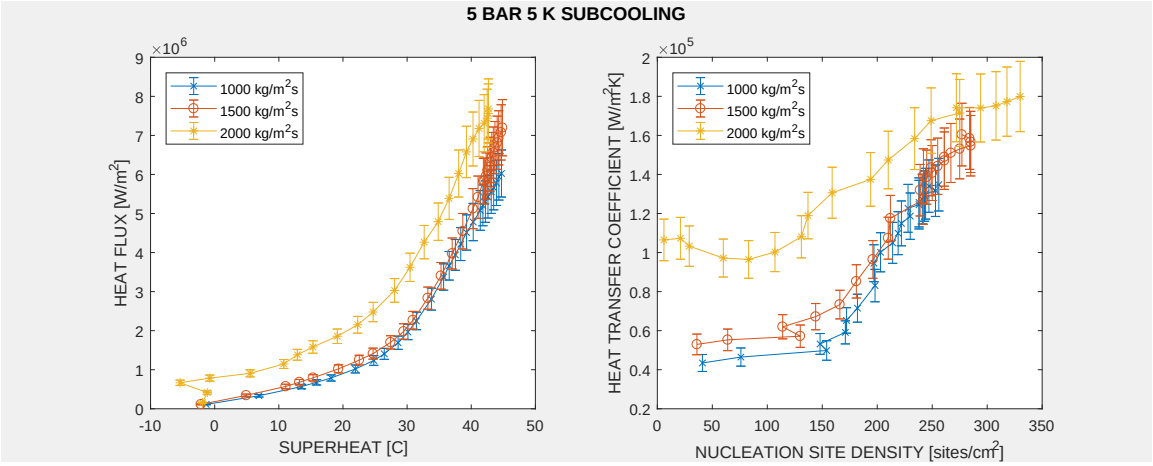

Figure B-16: Boiling Curves (left), Heat Transfer Coefficient versus Nucleation Site Density (right) for 5 bar, 5 K all mass fluxes.

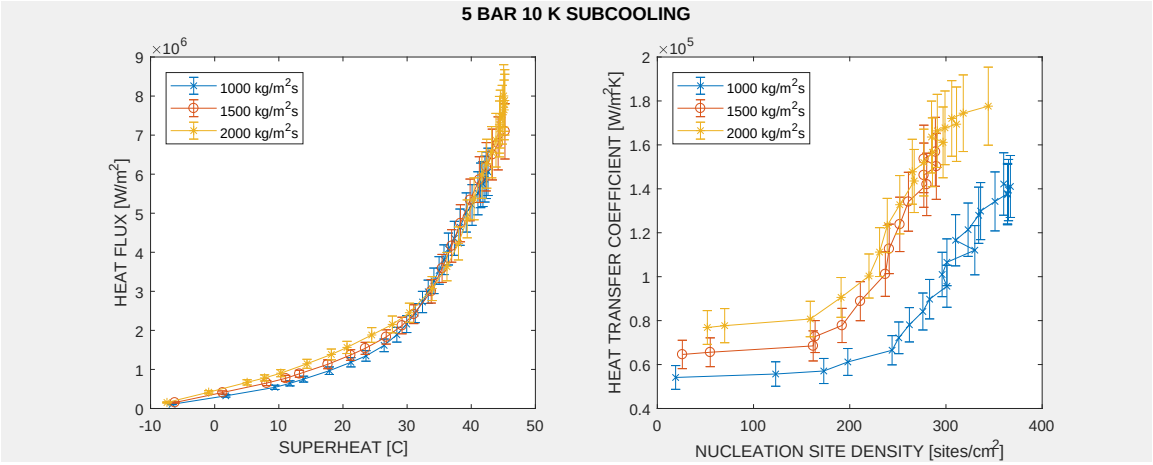

Figure B-17: Boiling Curves (left), Heat Transfer Coefficient versus Nucleation Site Density (right) for 5 bar, 10 K all mass fluxes.

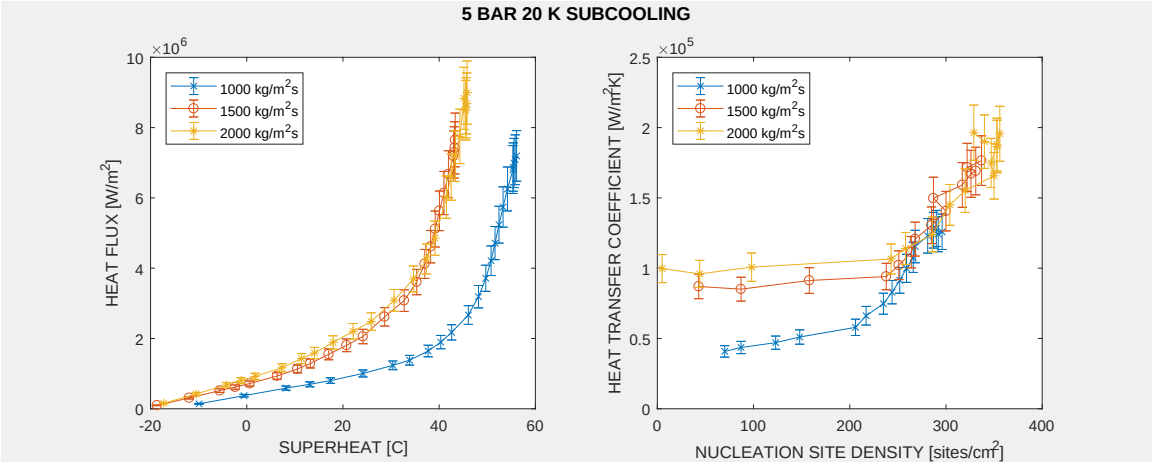

Figure B-18: Boiling Curves (left), Heat Transfer Coefficient versus Nucleation Site Density (right) for 5 bar, 20 K all mass fluxes.

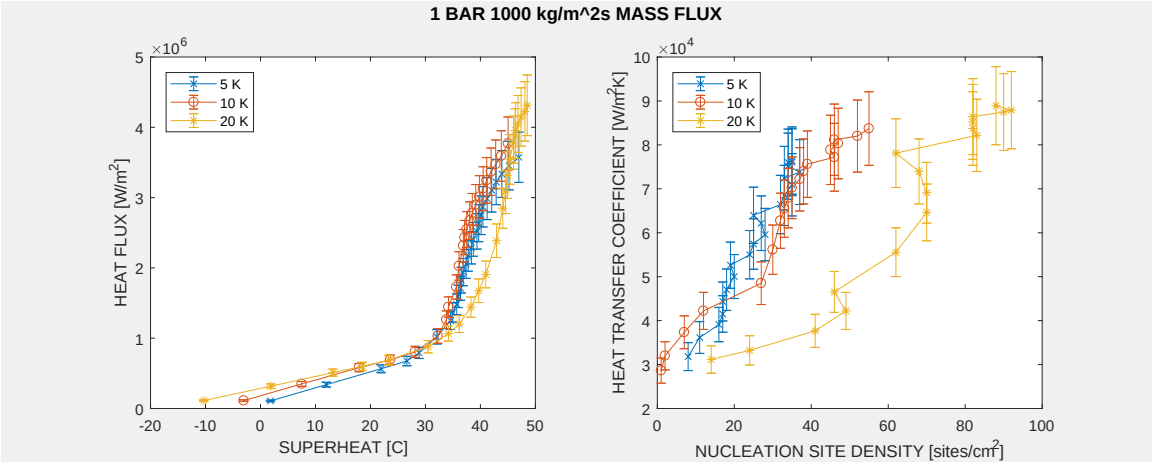

Figure B-19: Boiling Curves (left), Heat Transfer Coefficient versus Nucleation Site Density (right) for 1 bar, 1000 $\frac{kg}{m^2 s}$ all subcoolings.

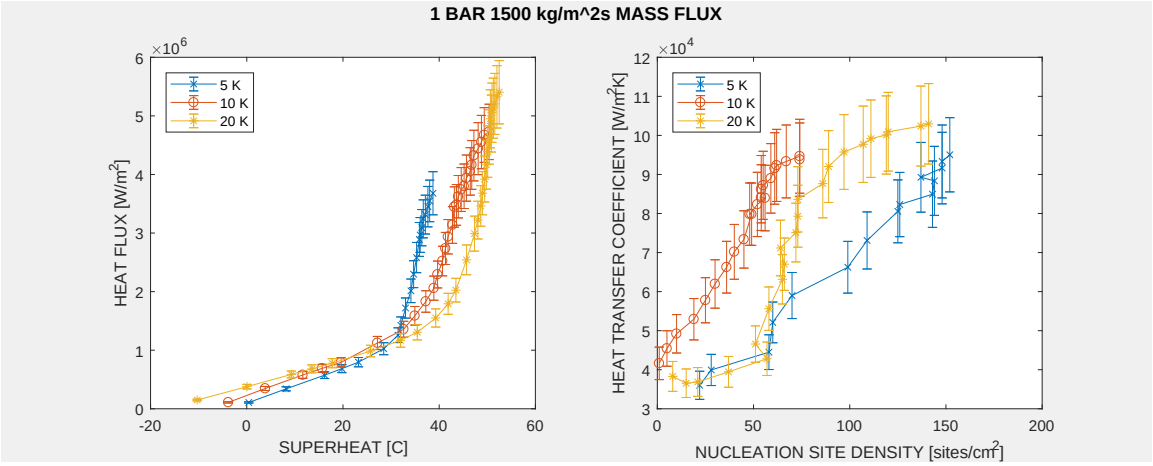

Figure B-20: Boiling Curves (left), Heat Transfer Coefficient versus Nucleation Site Density (right) for 1 bar, 1500 $\frac{kg}{m^2 s}$ all subcoolings.

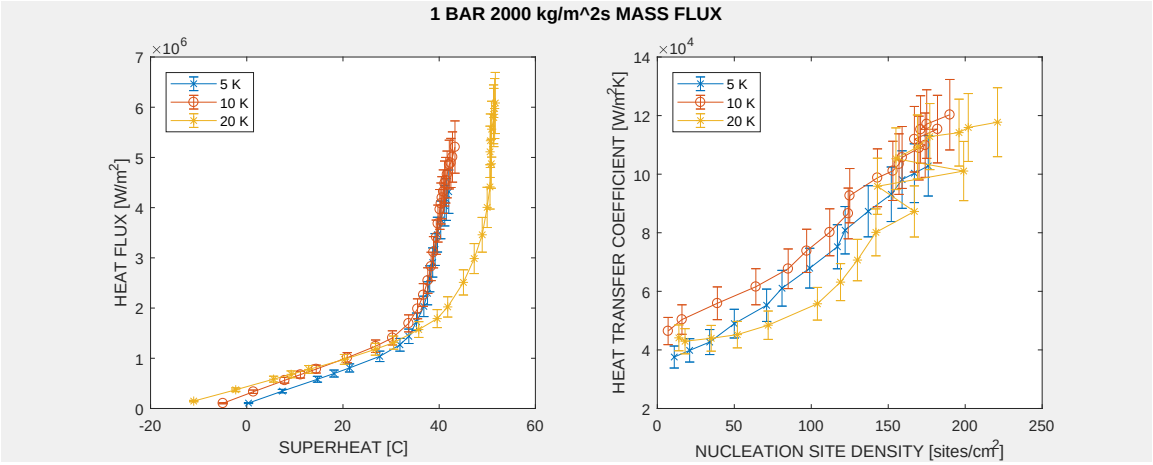

Figure B-21: Boiling Curves (left), Heat Transfer Coefficient versus Nucleation Site Density (right) for 1 bar, 2000 $\frac{kg}{m^2 s}$ all subcoolings.

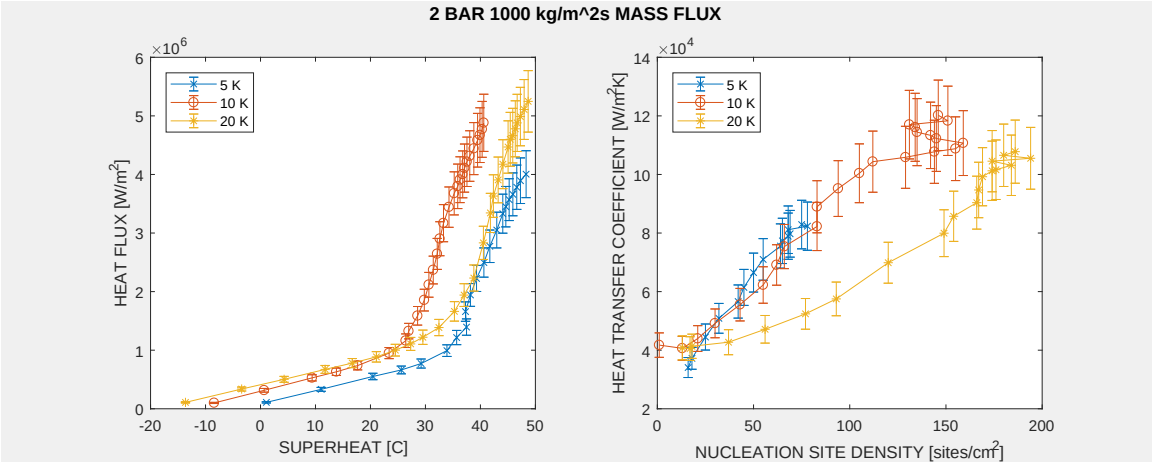

Figure B-22: Boiling Curves (left), Heat Transfer Coefficient versus Nucleation Site Density (right) for 2 bar, 1000 $\frac{kg}{m^2 s}$ all subcoolings.

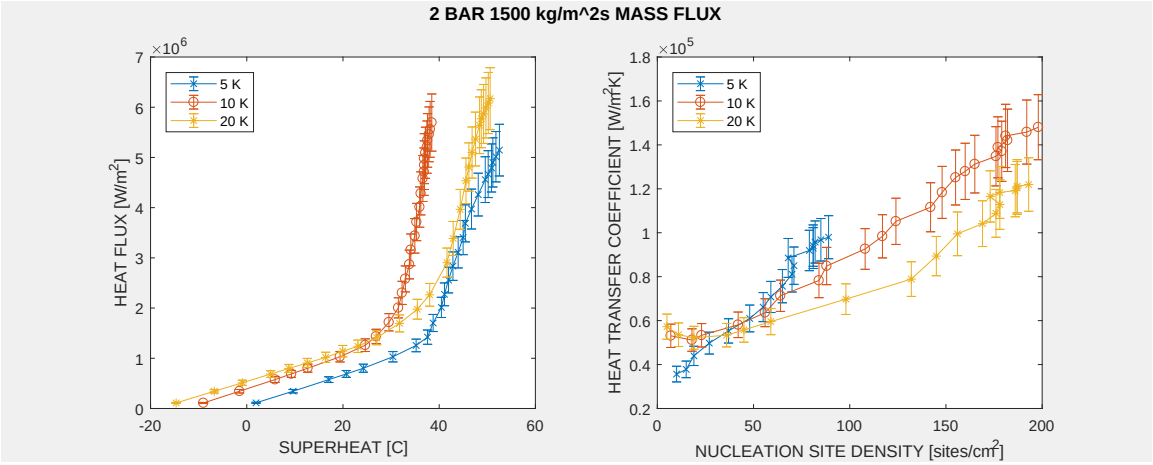

Figure B-23: Boiling Curves (left), Heat Transfer Coefficient versus Nucleation Site Density (right) for 2 bar, 1500 $\frac{kg}{m^2 s}$ all subcoolings.

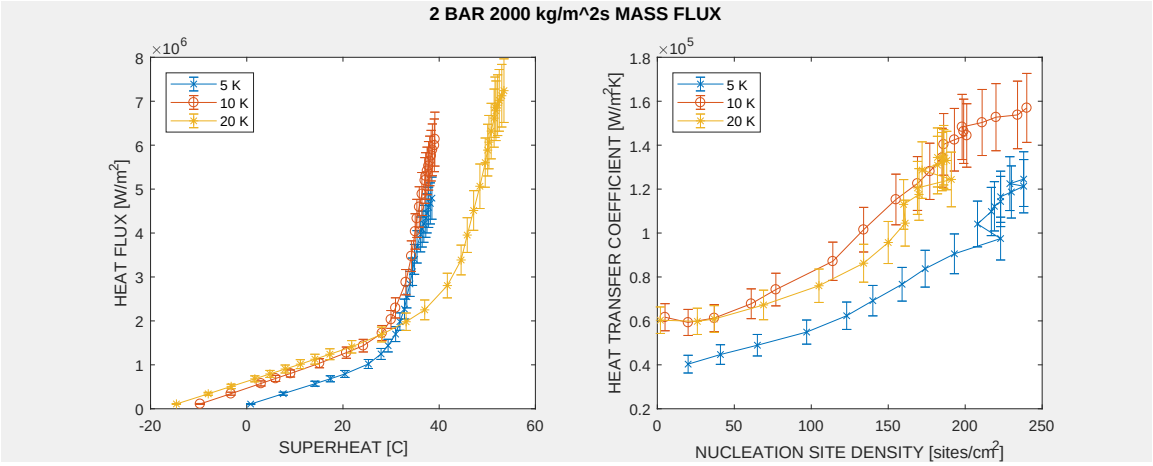

Figure B-24: Boiling Curves (left), Heat Transfer Coefficient versus Nucleation Site Density (right) for 2 bar, 2000 $\frac{kg}{m^2 s}$ all subcoolings.

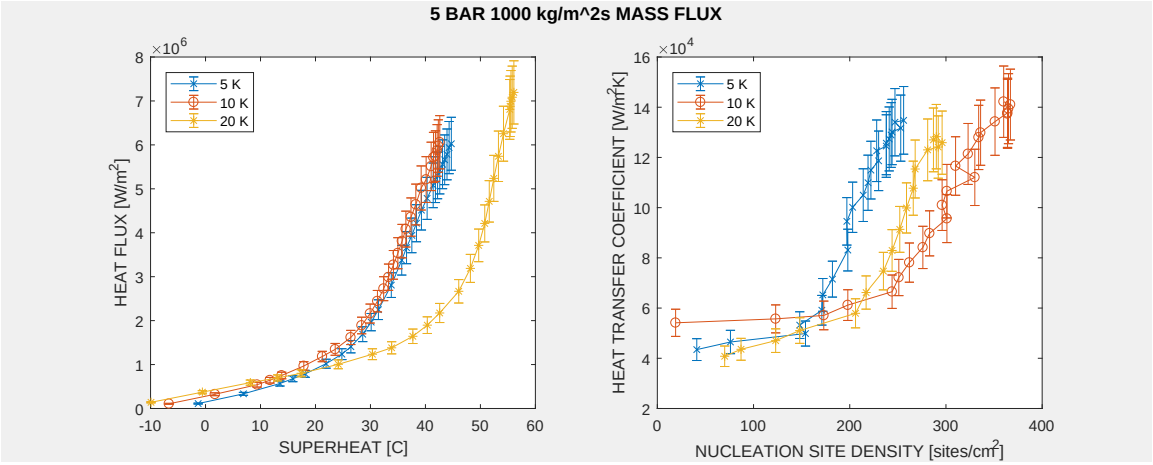

Figure B-25: Boiling Curves (left), Heat Transfer Coefficient versus Nucleation Site Density (right) for 5 bar, 1000 $\frac{kg}{m^2 s}$ all subcoolings.

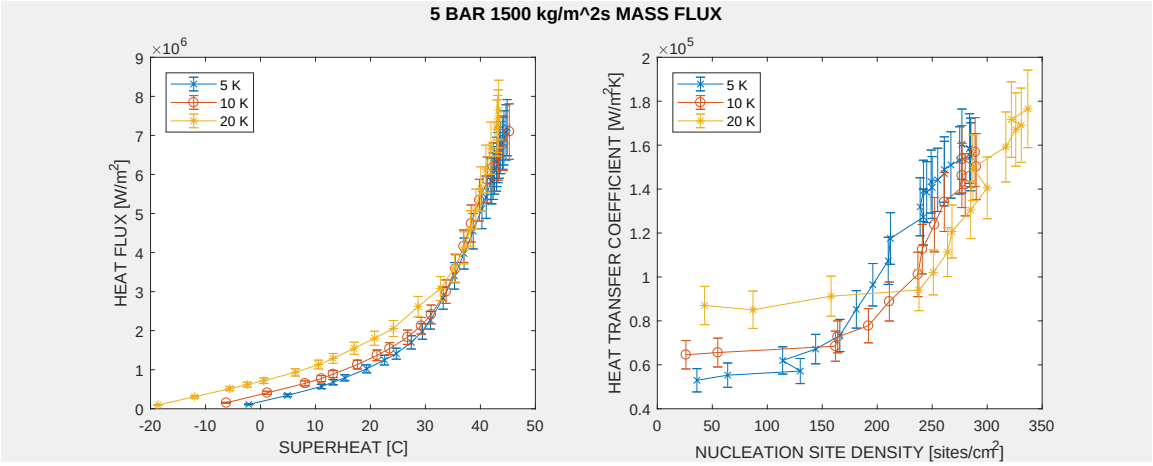

Figure B-26: Boiling Curves (left), Heat Transfer Coefficient versus Nucleation Site Density (right) for 5 bar, 1500 $\frac{kg}{m^2 s}$ all subcoolings.

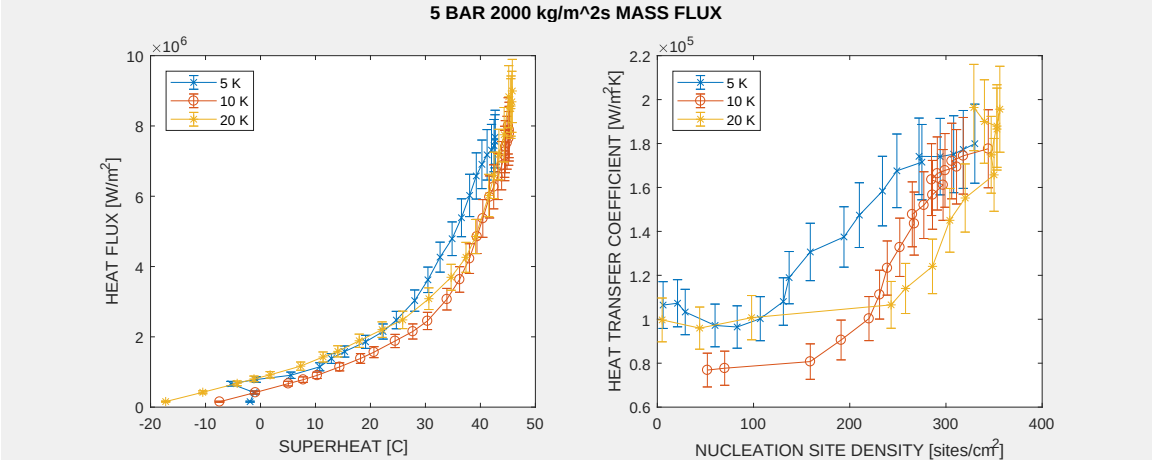

Figure B-27: Boiling Curves (left), Heat Transfer Coefficient versus Nucleation Site Density (right) for 5 bar, 2000 $\frac{kg}{m^2 s}$ all subcoolings.

Appendix C

Bubble Period, Growth Time and Wait Time Data

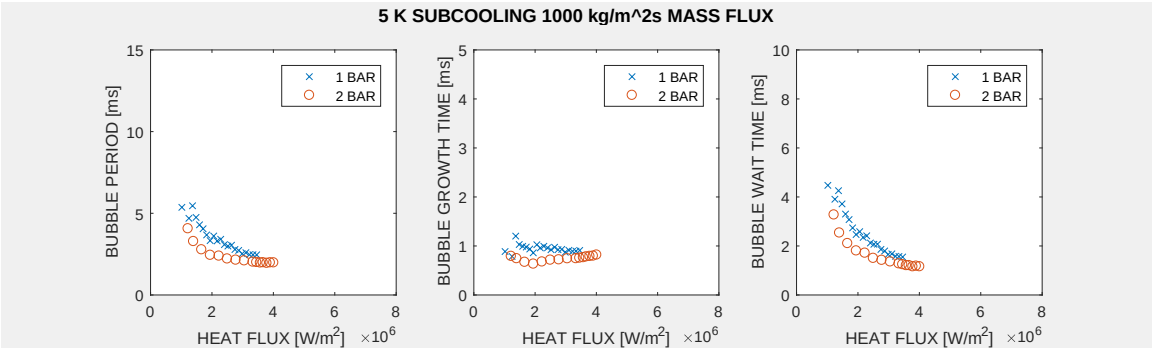

Figure C-1: Bubble period, growth time and wait time for 5 K, 1000 $\frac{kg}{m^2 s}$, 1 and 2 bar.

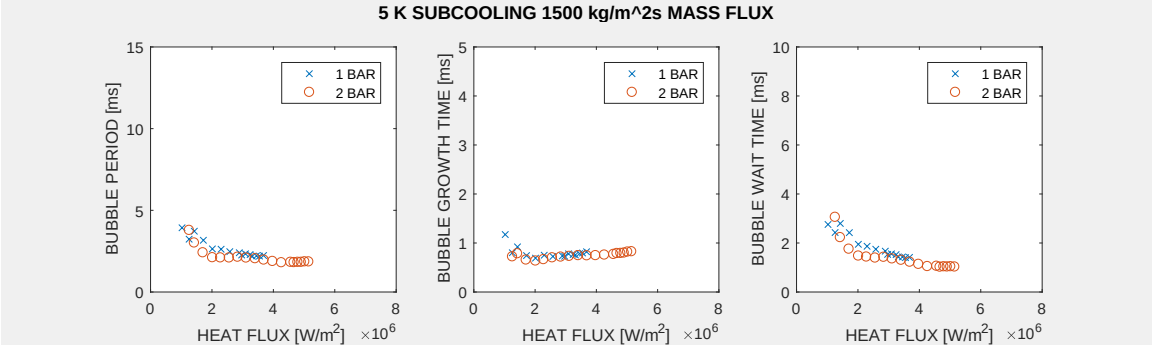

Figure C-2: Bubble period, growth time and wait time for 5 K, 1500 $\frac{kg}{m^2 s}$, 1 and 2 bar.

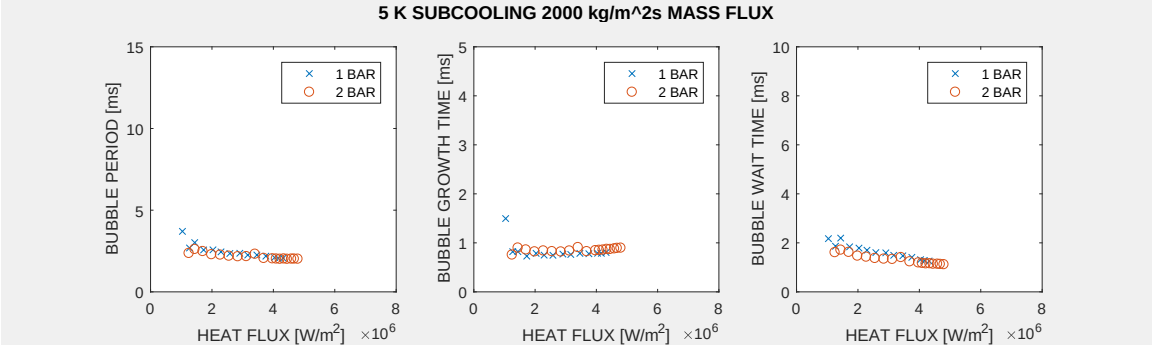

Figure C-3: Bubble period, growth time and wait time for 5 K, 2000 $\frac{kg}{m^2 s}$, 1 and 2 bar.

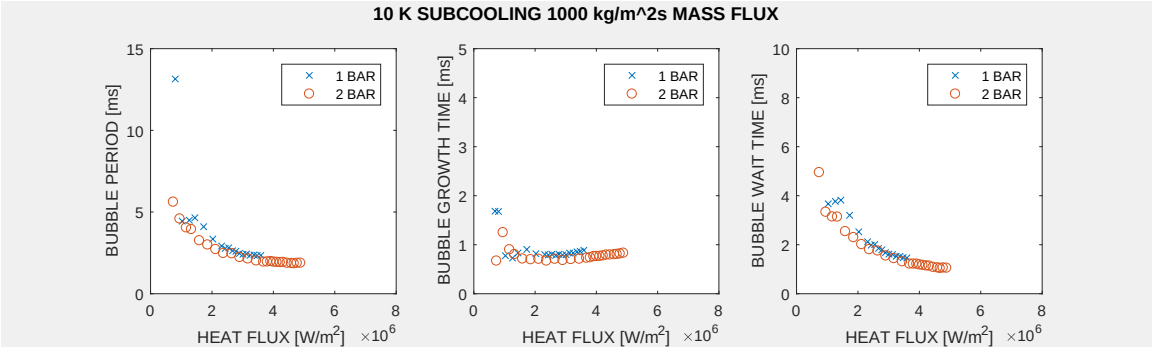

Figure C-4: Bubble period, growth time and wait time for 10 K, 1000 $\frac{kg}{m^2 s}$, 1 and 2 bar.

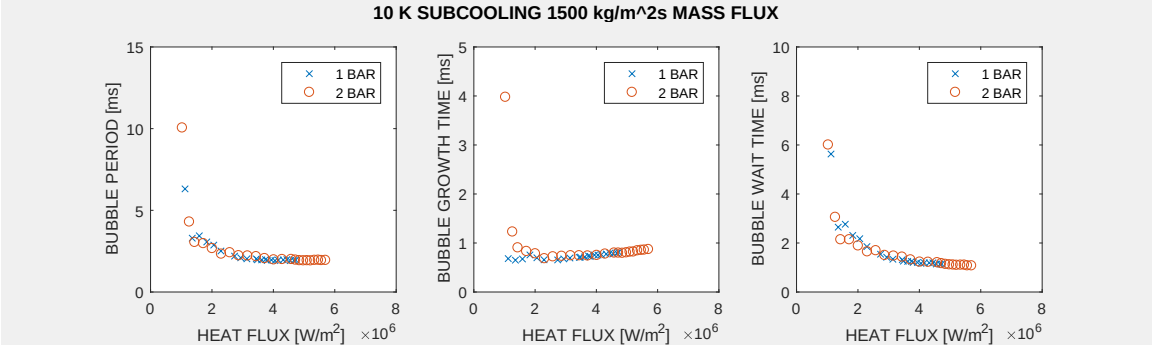

Figure C-5: Bubble period, growth time and wait time for 10 K, 1500 $\frac{kg}{m^2 s}$, 1 and 2 bar.

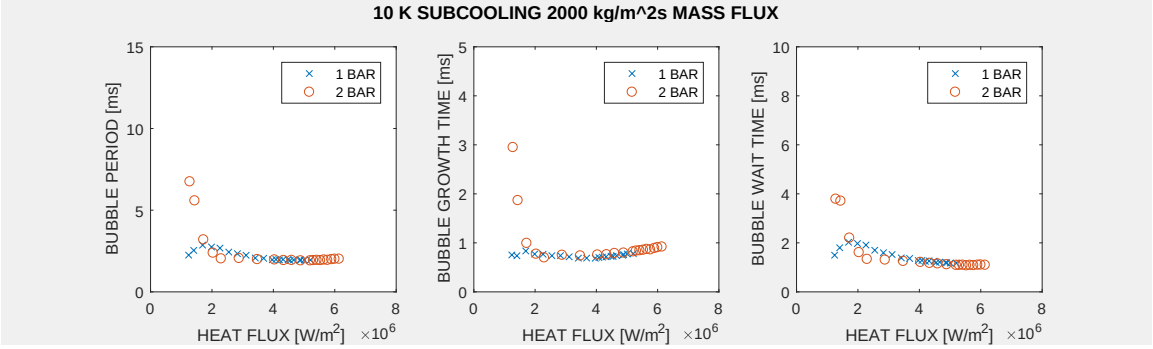

Figure C-6: Bubble period, growth time and wait time for 10 K, 2000 $\frac{kg}{m^2 s}$, 1 and 2 bar.

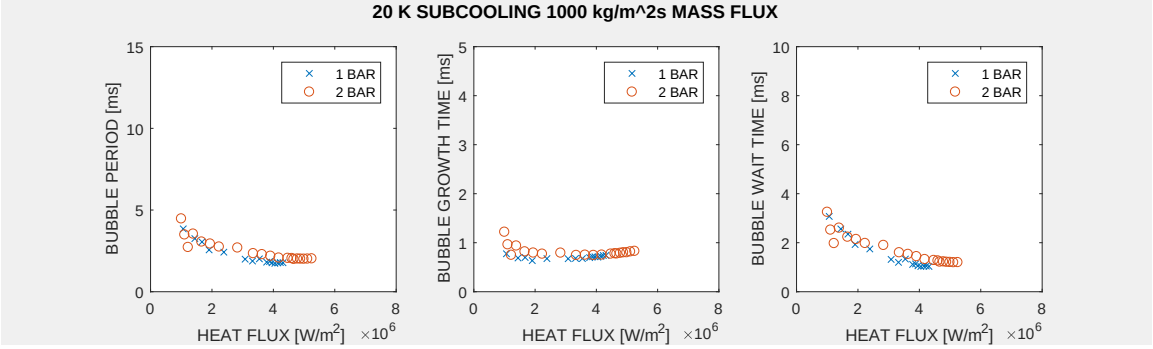

Figure C-7: Bubble period, growth time and wait time for 20 K, 1000 $\frac{kg}{m^2 s}$, 1 and 2 bar.

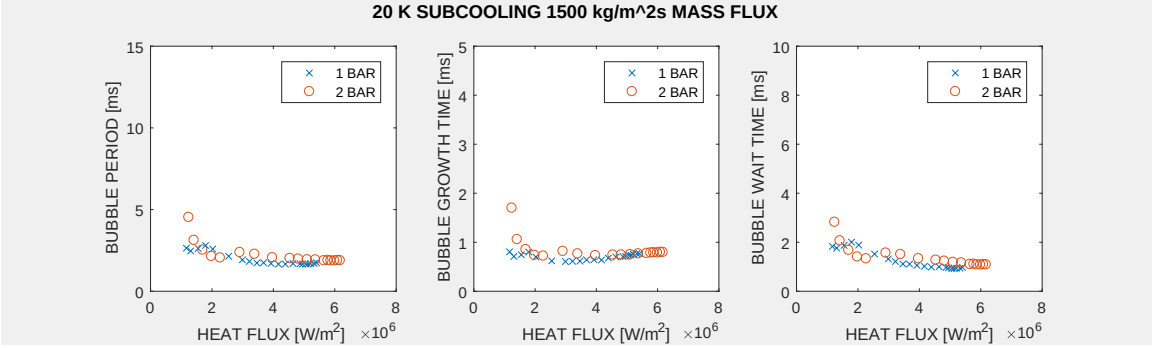

Figure C-8: Bubble period, growth time and wait time for 20 K, 1500 $\frac{kg}{m^2 s}$, 1 and 2 bar.

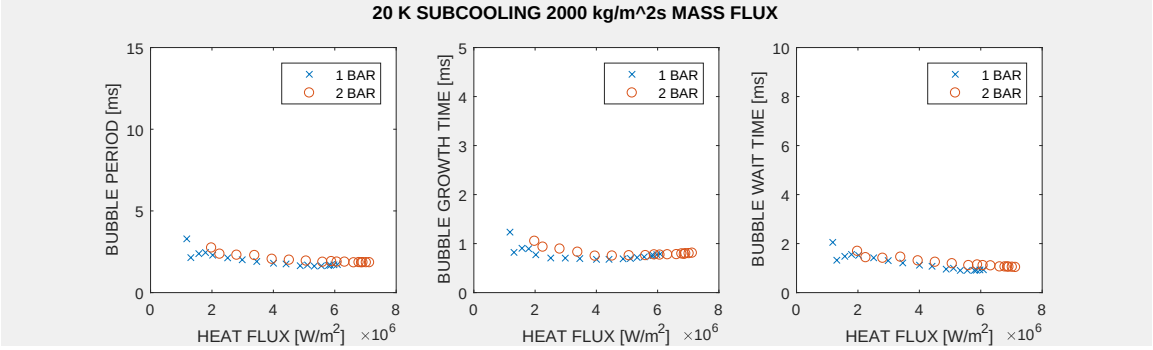

Figure C-9: Bubble period, growth time and wait time for 20 K, 2000 $\frac{kg}{m^2 s}$, 1 and 2 bar.

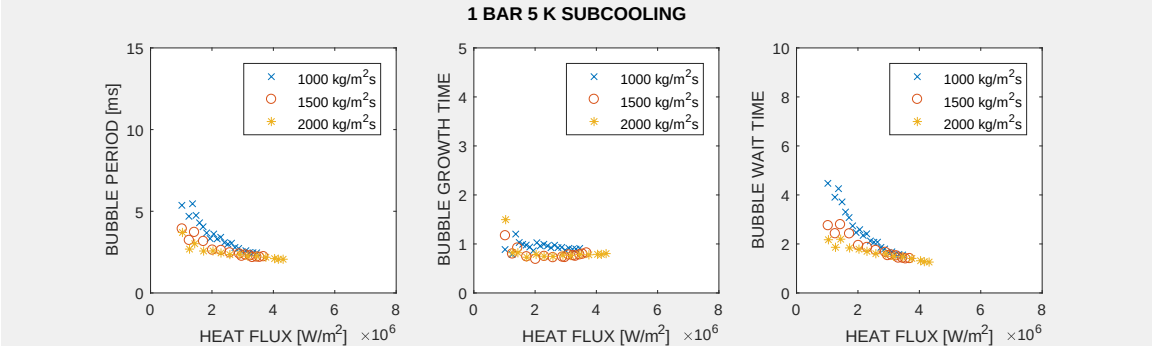

Figure C-10: Bubble period, growth time and wait time for 1 bar, 5 K all mass fluxes.

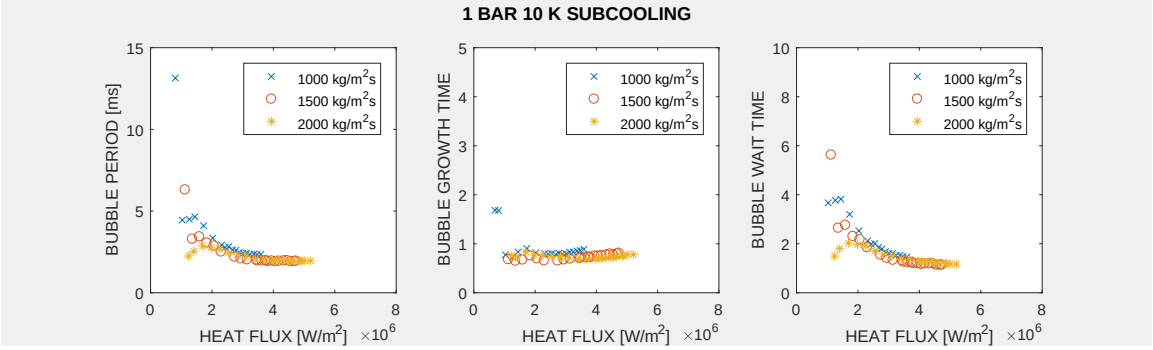

Figure C-11: Bubble period, growth time and wait time for 1 bar, 10 K all mass fluxes.

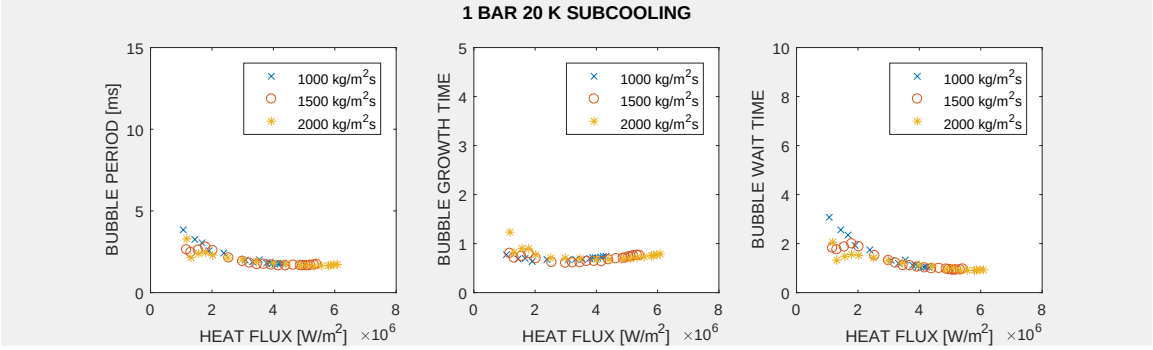

Figure C-12: Bubble period, growth time and wait time for 1 bar, 20 K all mass fluxes.

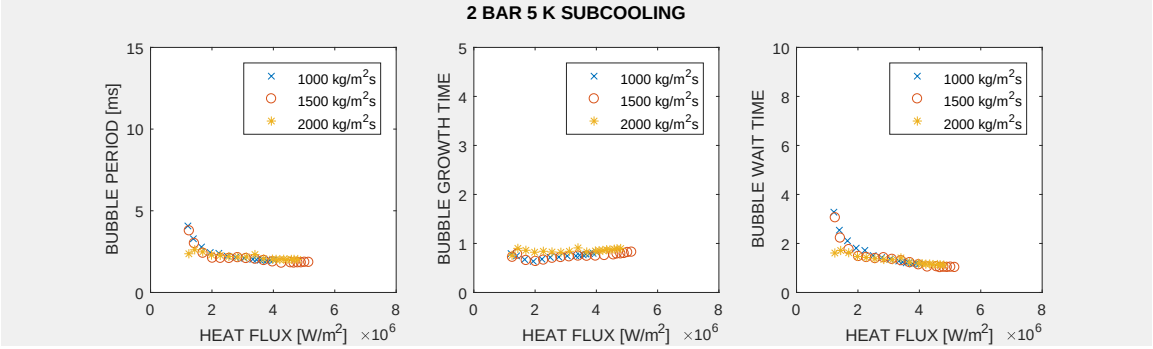

Figure C-13: Bubble period, growth time and wait time for 2 bar, 5 K all mass fluxes.

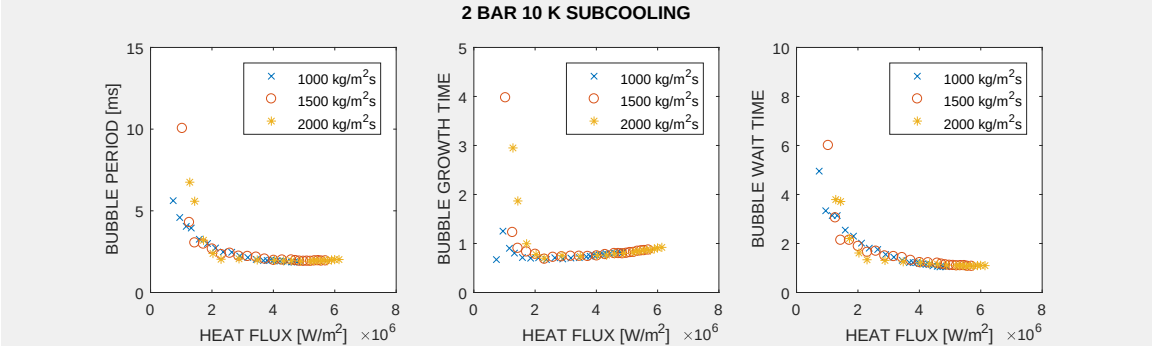

Figure C-14: Bubble period, growth time and wait time for 2 bar, 10 K all mass fluxes.

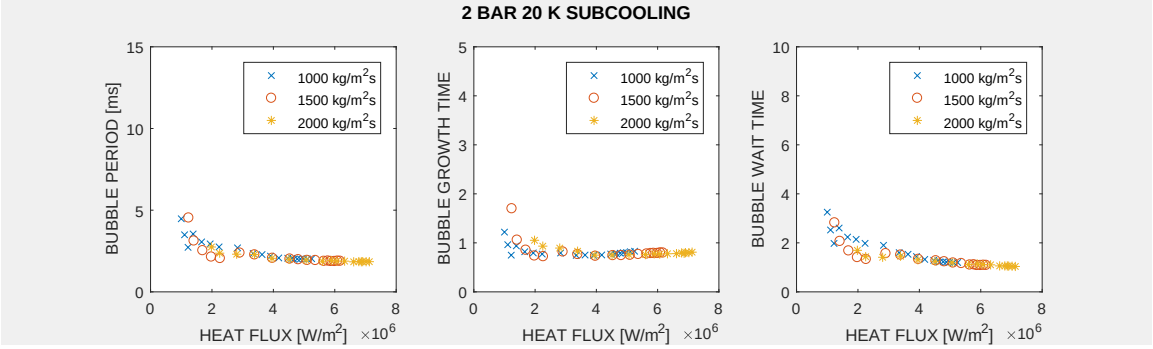

Figure C-15: Bubble period, growth time and wait time for 2 bar, 20 K all mass fluxes.

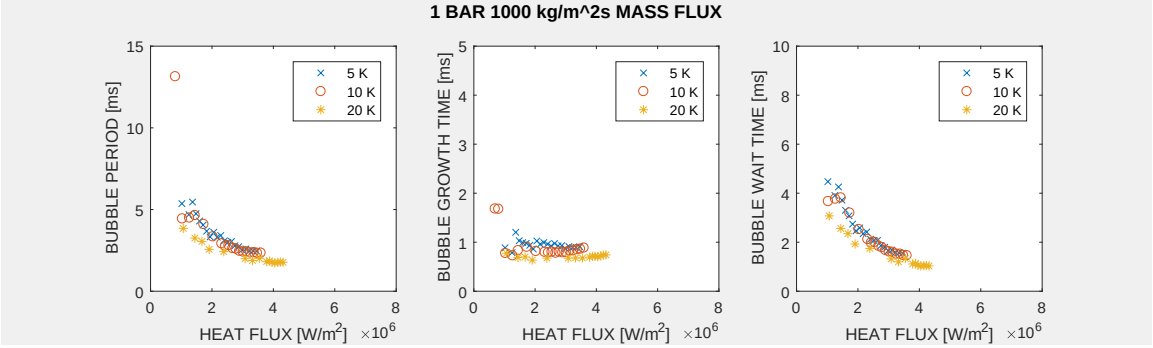

Figure C-16: Bubble period, growth time and wait time for 1 bar, 1000 $\frac{kg}{m^2 s}$ all subcoolings.

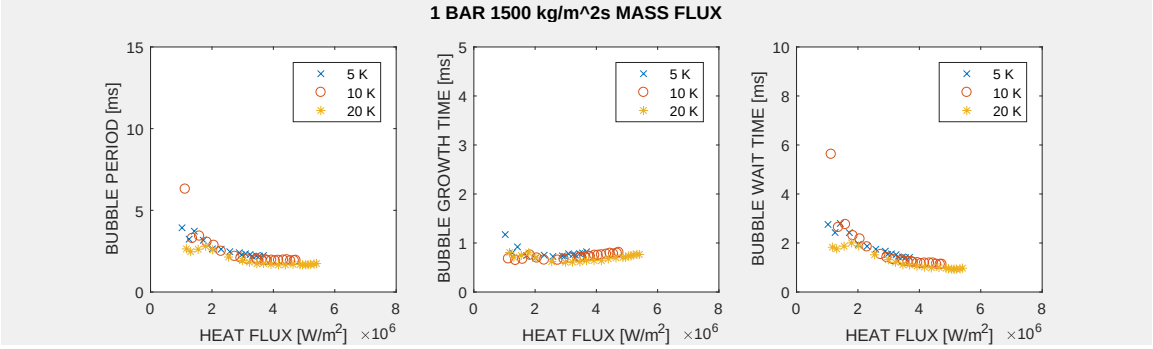

Figure C-17: Bubble period, growth time and wait time for 1 bar, 1500 $\frac{kg}{m^2 s}$ all subcoolings.

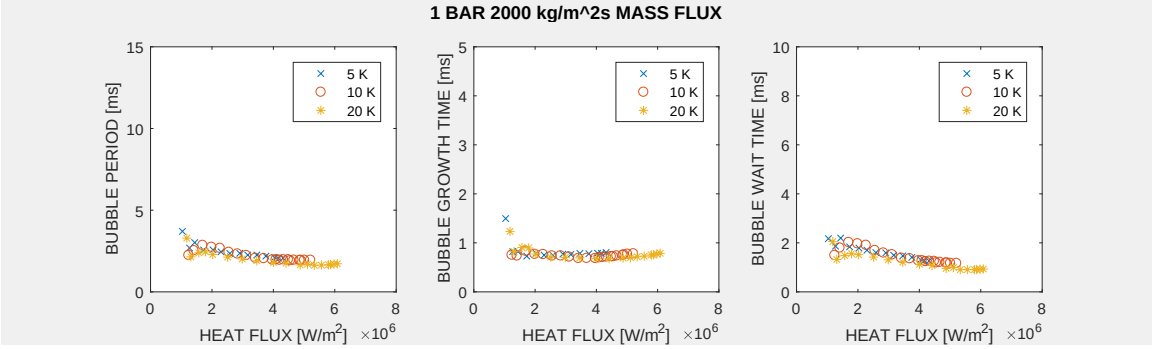

Figure C-18: Bubble period, growth time and wait time for 1 bar, 2000 $\frac{kg}{m^2 s}$ all subcoolings.

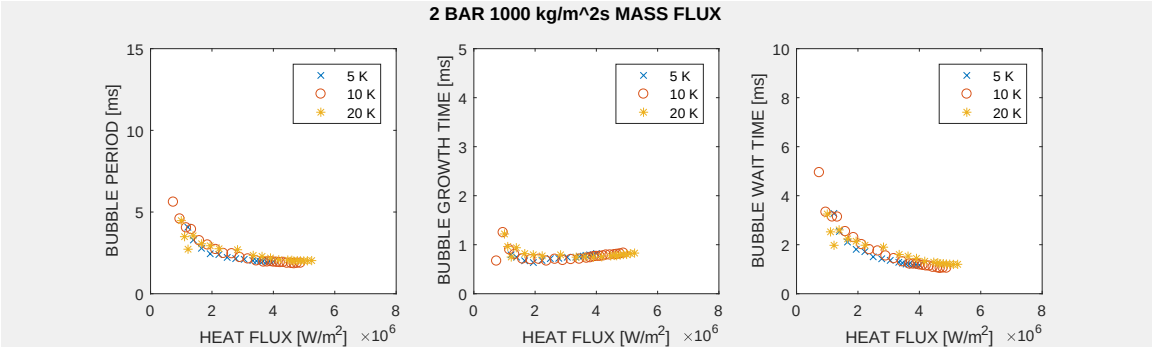

Figure C-19: Bubble period, growth time and wait time for 2 bar, 1000 $\frac{kg}{m^2 s}$ all subcoolings.

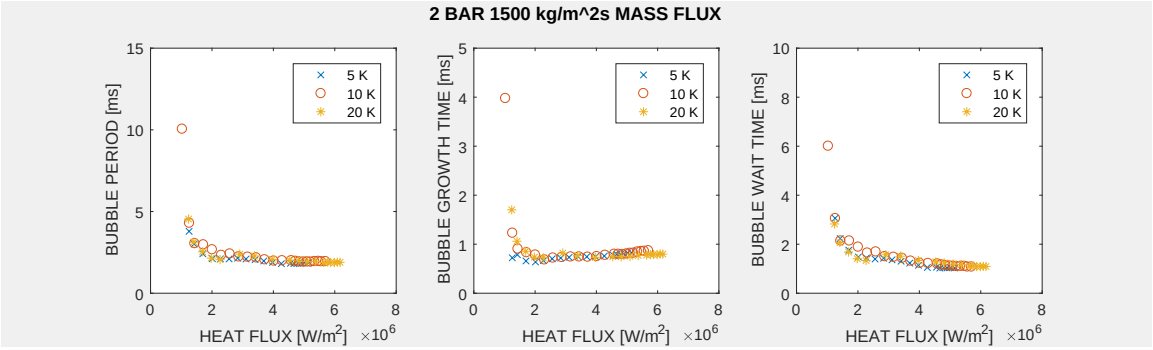

Figure C-20: Bubble period, growth time and wait time for 2 bar, 1500 $\frac{kg}{m^2 s}$ all subcoolings.

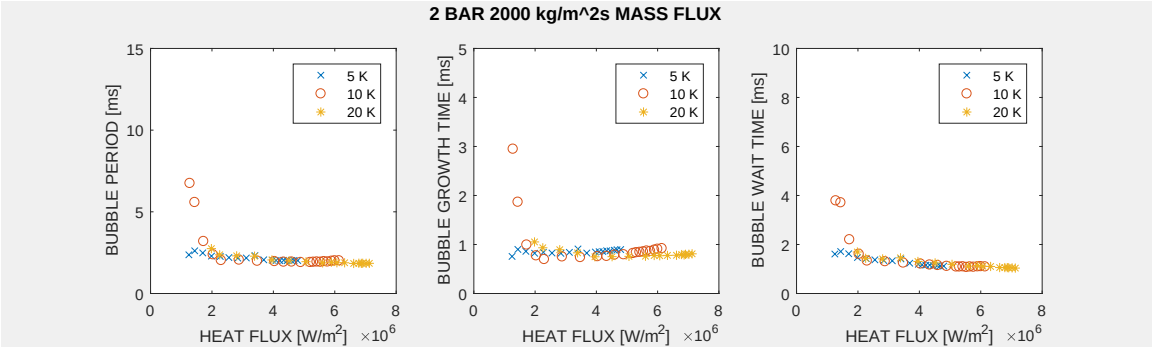

Figure C-21: Bubble period, growth time and wait time for 2 bar, 2000 $\frac{kg}{m^2 s}$ all subcoolings.

Appendix D

Heat Flux Partitioning Data

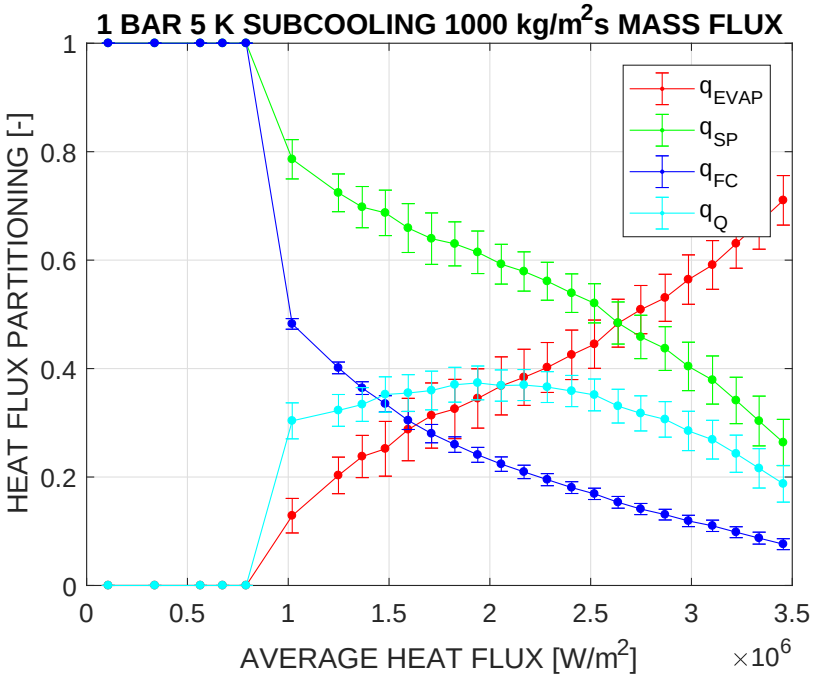

Figure D-1: Heat Flux Partitioning for 1bar, 5 K, 1000 $\frac{kg}{m^2 s}$

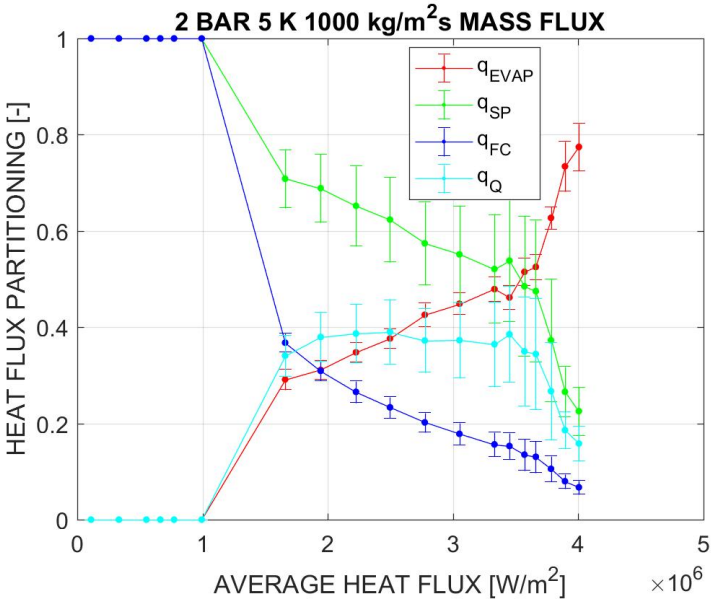

Figure D-2: Heat Flux Partitioning for 2bar, 5 K, 1000 $\frac{kg}{m^2 s}$

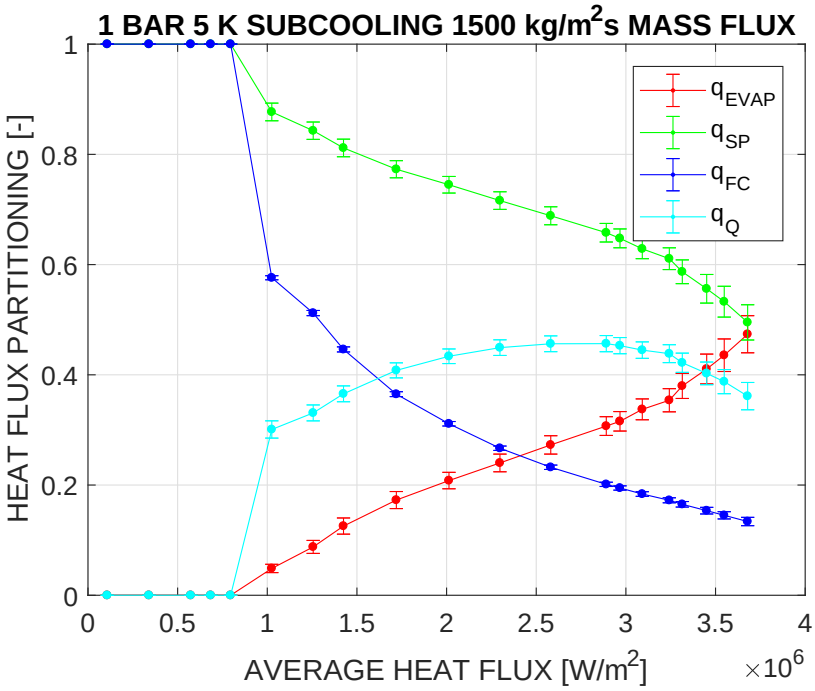

Figure D-3: Heat Flux Partitioning for 1bar, 5 K, 1500 $\frac{kg}{m^2 s}$

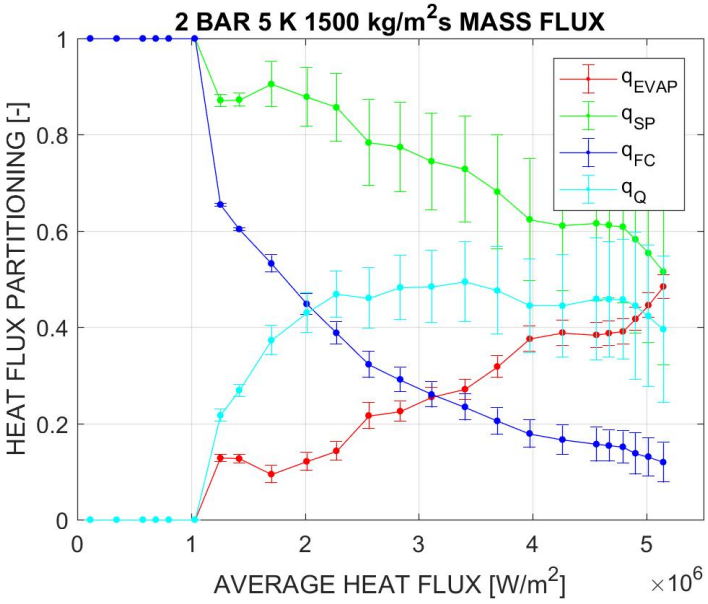

Figure D-4: Heat Flux Partitioning for 2bar, 5 K, 1500 $\frac{kg}{m^2 s}$

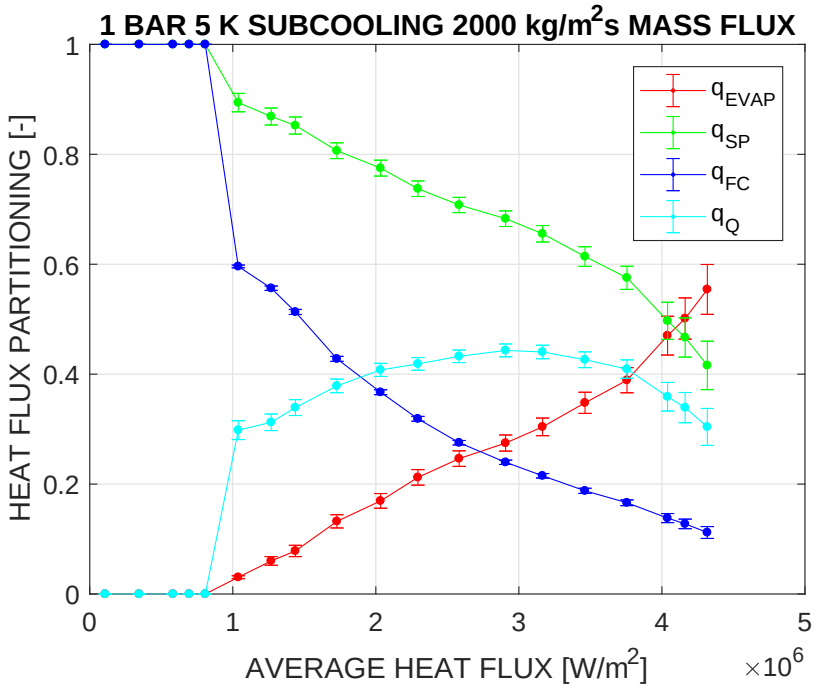

Figure D-5: Heat Flux Partitioning for 1bar, 5 K, 2000 $\frac{kg}{m^2 s}$

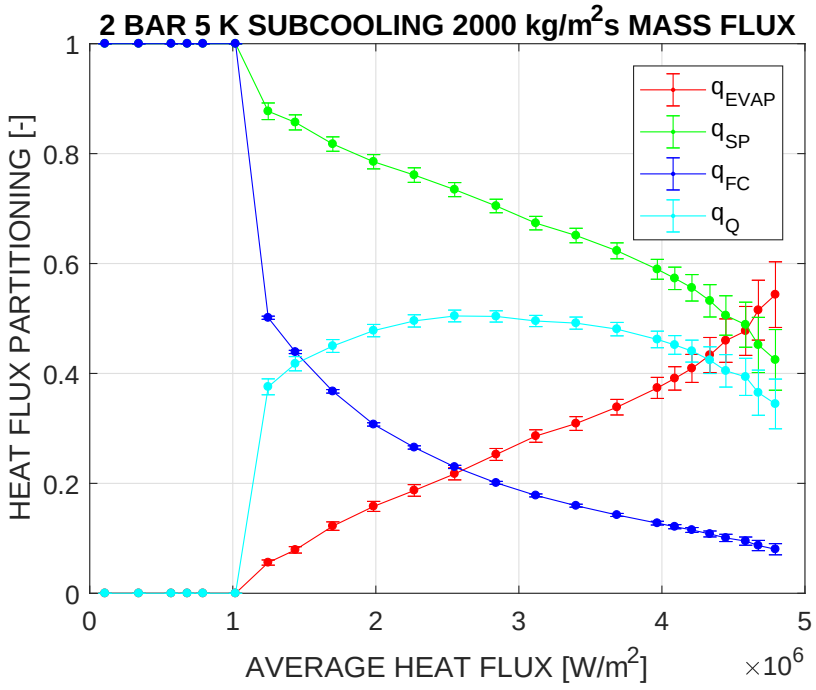

Figure D-6: Heat Flux Partitioning for 2bar, 5 K, 2000 $\frac{kg}{m^2 s}$

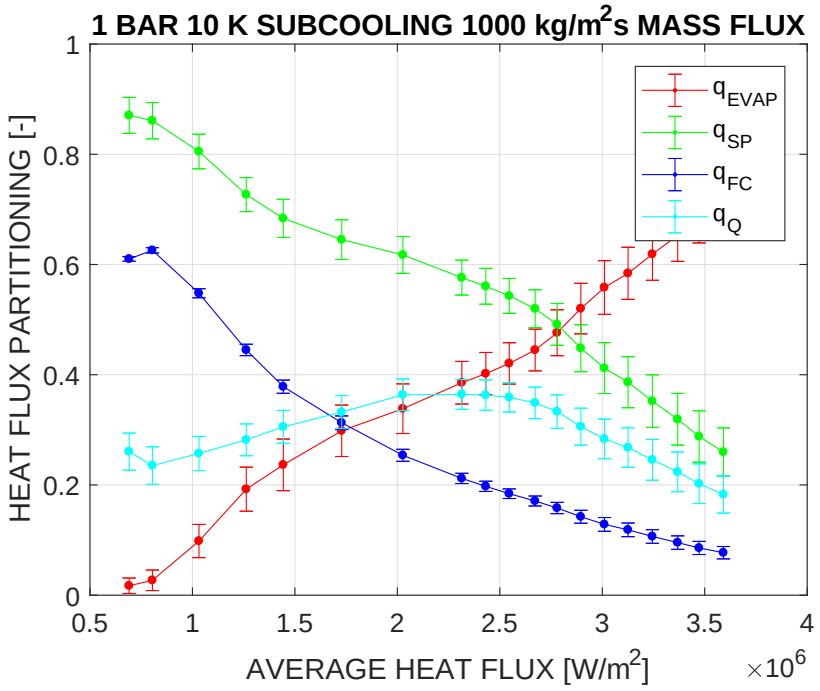

Figure D-7: Heat Flux Partitioning for 1bar, 10 K, 1000 $\frac{kg}{m^2 s}$

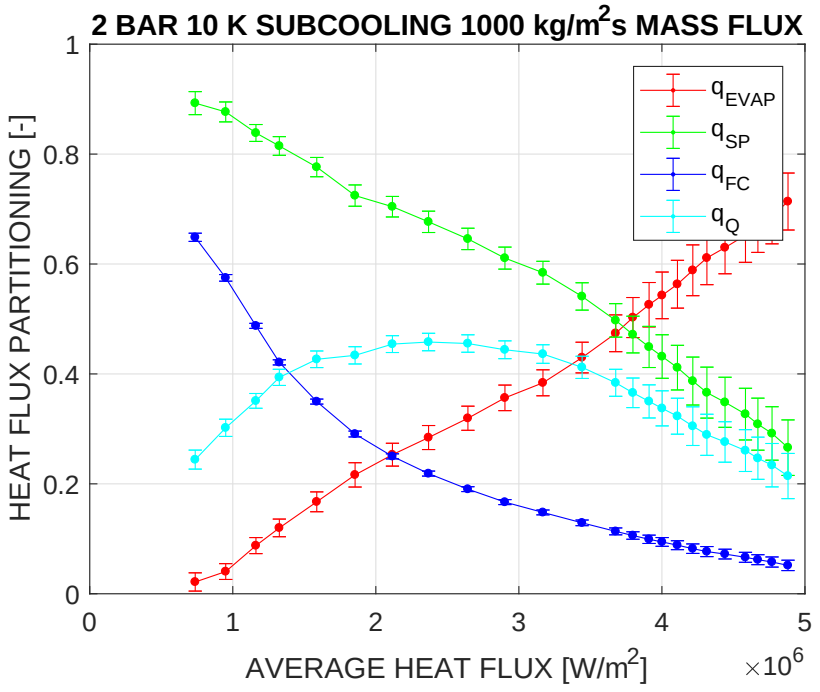

Figure D-8: Heat Flux Partitioning for 2bar, 10 K, 1000 $\frac{kg}{m^2 s}$

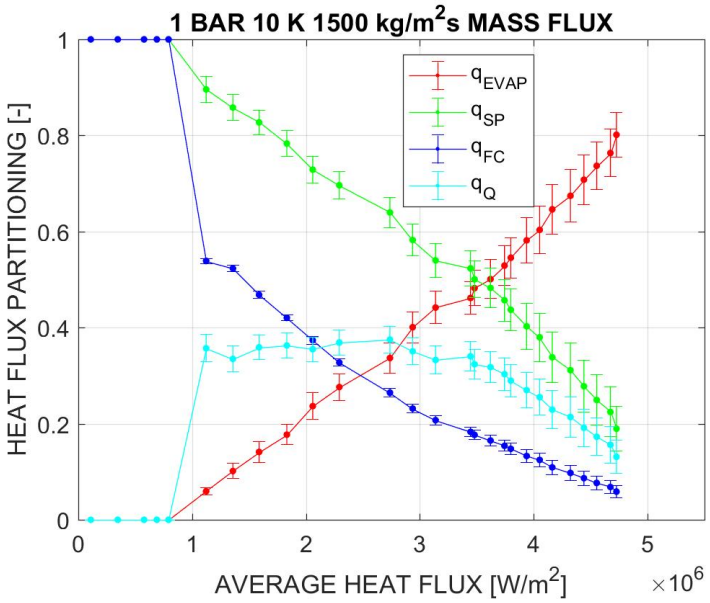

Figure D-9: Heat Flux Partitioning for 1bar, 10 K, 1500 $\frac{kg}{m^2 s}$

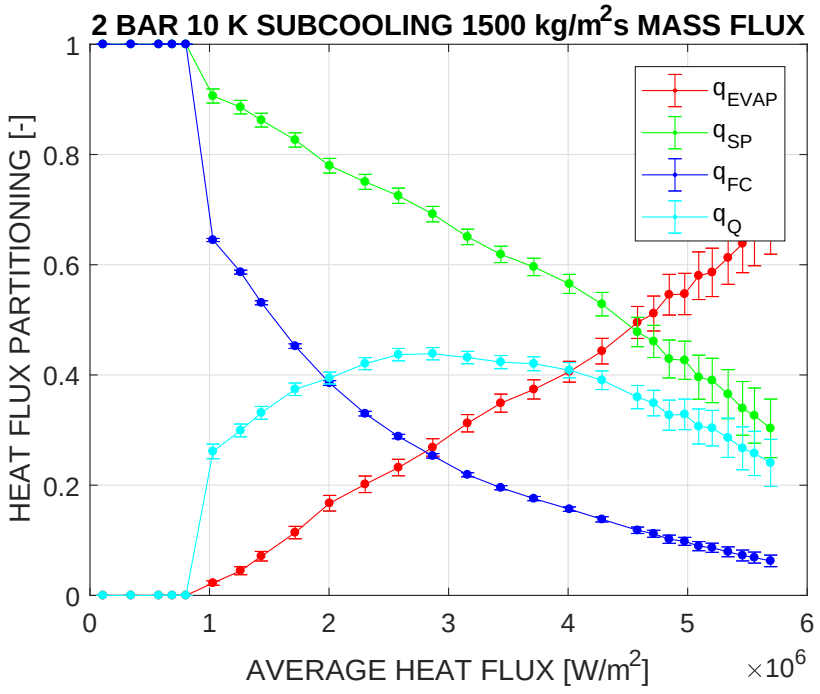

Figure D-10: Heat Flux Partitioning for 2bar, 10 K, 1500 $\frac{kg}{m^2 s}$

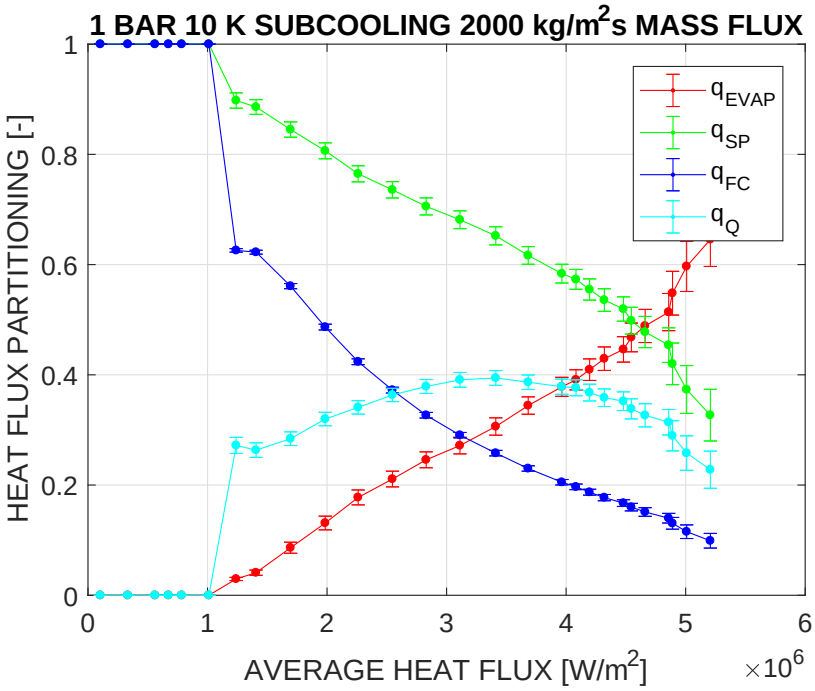

Figure D-11: Heat Flux Partitioning for 1bar, 10 K, 2000 $\frac{kg}{m^2 s}$

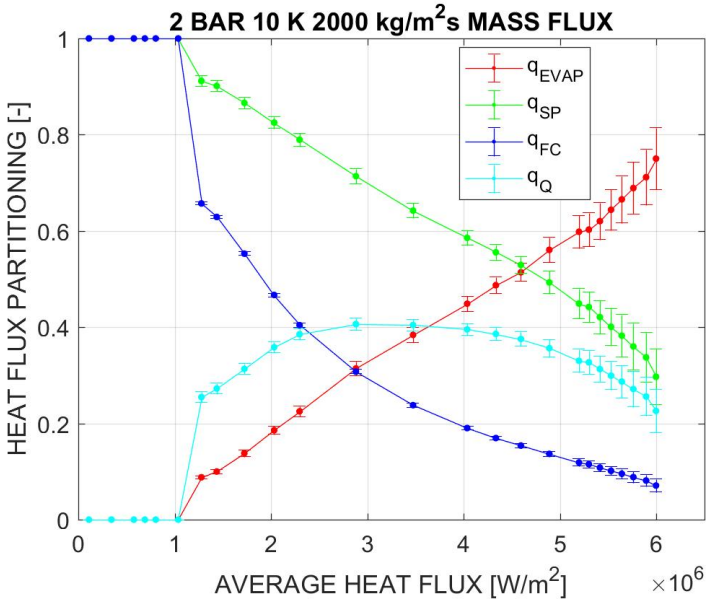

Figure D-12: Heat Flux Partitioning for 2bar, 10 K, 2000 $\frac{kg}{m^2 s}$

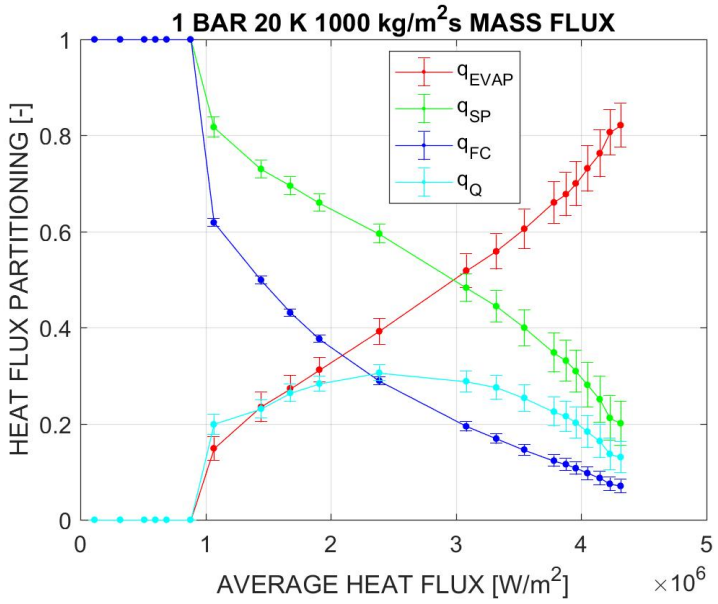

Figure D-13: Heat Flux Partitioning for 1bar, 20 K, 1000 $\frac{kg}{m^2 s}$

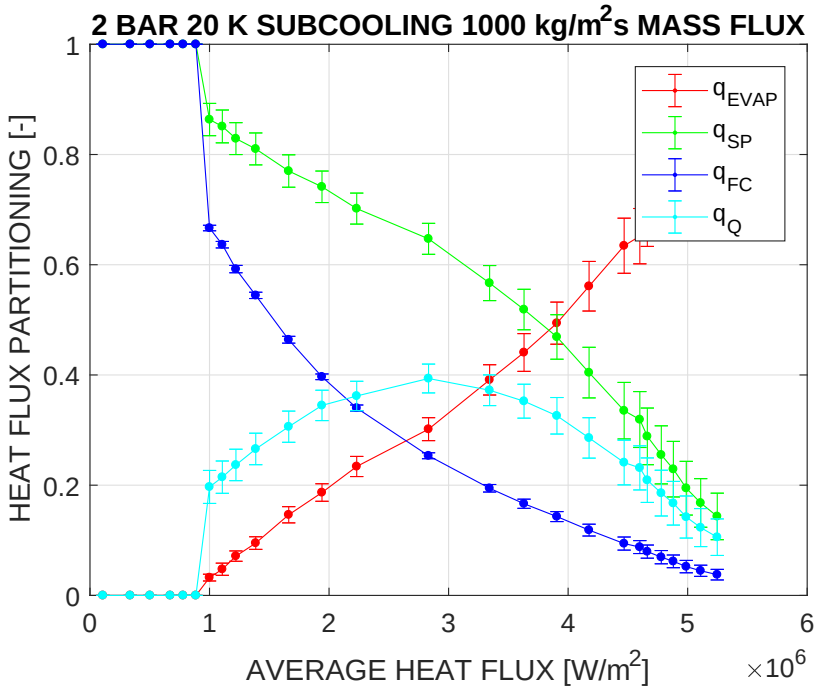

Figure D-14: Heat Flux Partitioning for 2bar, 20 K, 1000 $\frac{kg}{m^2 s}$

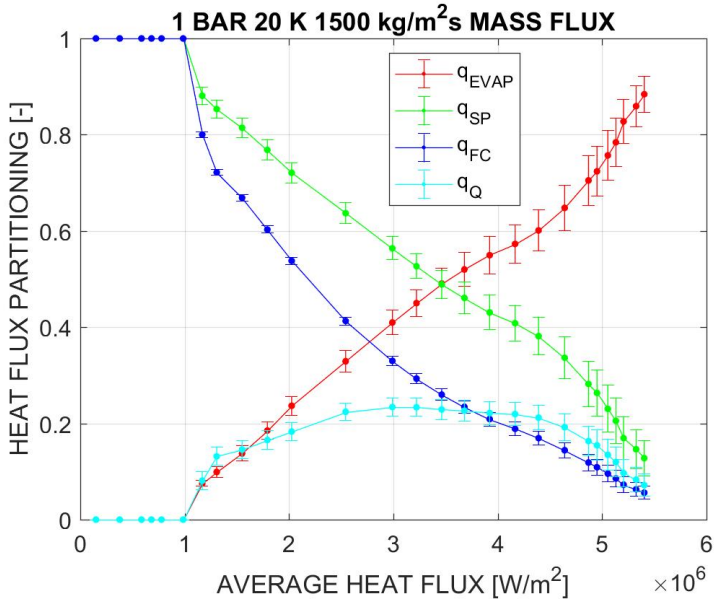

Figure D-15: Heat Flux Partitioning for 1bar, 20 K, 1500 $\frac{kg}{m^2 s}$

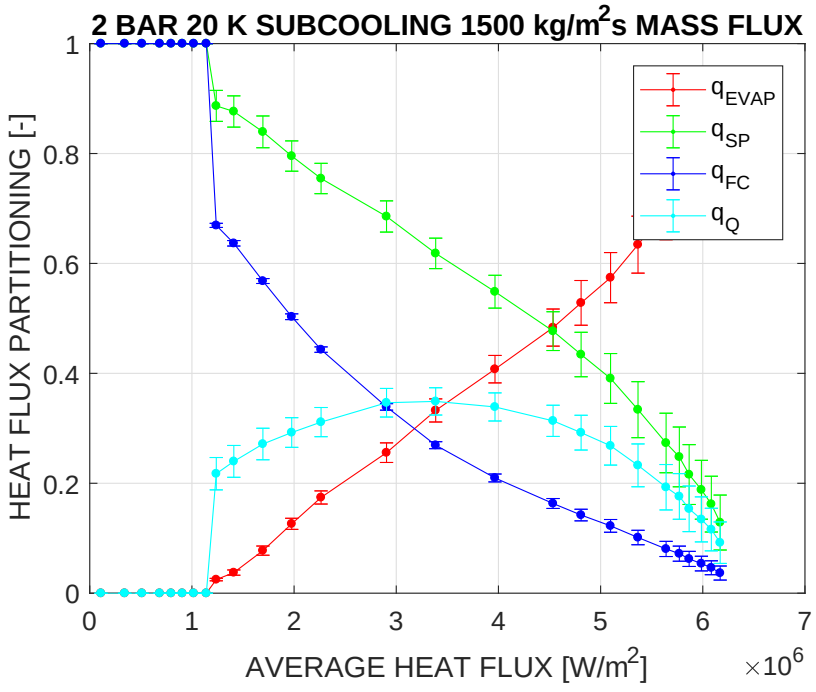

Figure D-16: Heat Flux Partitioning for 2bar, 20 K, 1500 $\frac{kg}{m^2 s}$

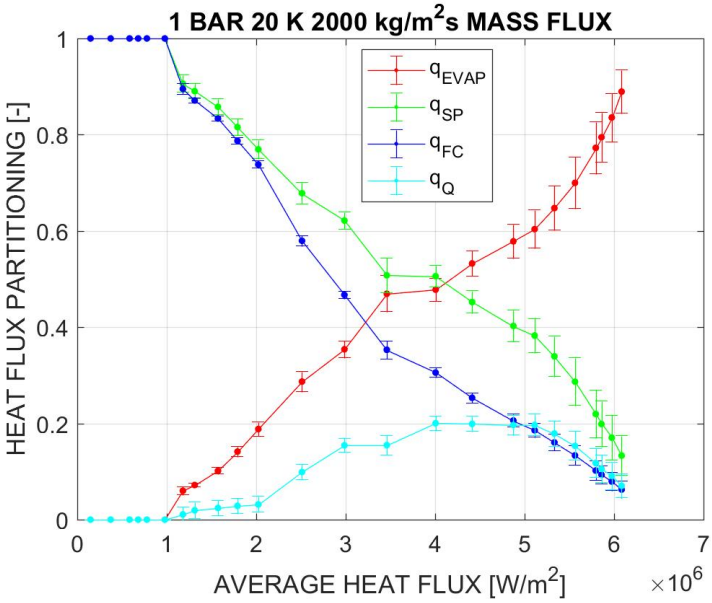

Figure D-17: Heat Flux Partitioning for 1bar, 20 K, 2000 $\frac{kg}{m^2 s}$

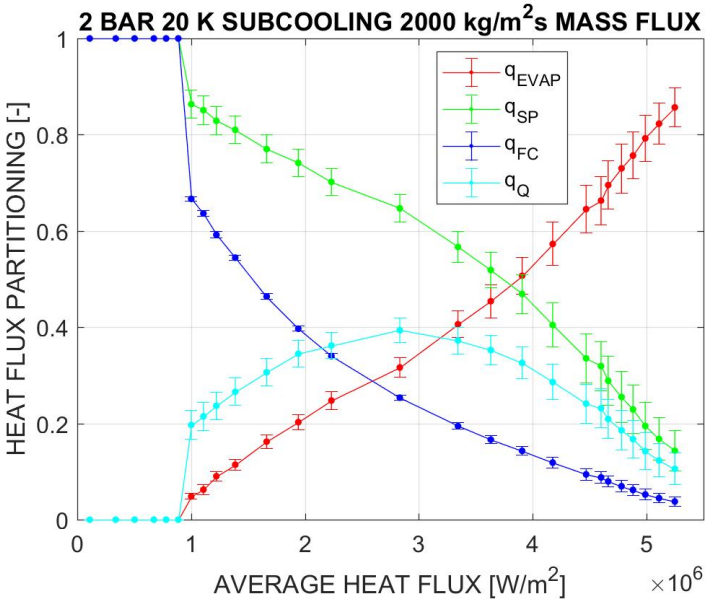

Figure D-18: Heat Flux Partitioning for 2bar, 20 K, 2000 $\frac{kg}{m^2 s}$